The Two-dimensional Electron Gas at the Lanthanum Aluminate - Strontium Titanate Heterointerface

By

Tomas Hernandez

A dissertation submitted in partial fulfillment of the

requirements for the degree of

Doctor of Philosophy

(Physics)

at the

UNIVERSITY OF WISCONSIN – MADISON

2013

Date of final oral examination: August 15, 2013

The dissertation is approved by the following members of the Final Oral Committee:

Mark S. Rzchowski, Professor, Physics

Chang-Beom Eom, Professor, Materials Science and Engineering

Franz Himpsel, Professor, Physics

Adele Ruosi, Senior Visiting Scientist, Physics

Michael Winokur, Professor, Physics

Dedicated to my late father Tomas

Abstract

Since the discovery of the conducting two dimensional electron gas (2DEG) at the interface of insulating oxide materials $LaAlO_3$ and $SrTiO_3$ in 2004, this system has shown a vast diversity of physical properties including superconductivity, ferromagnetism and field induced metal-insulator phase transitions. In this dissertation we discuss three advances by our collaboration that bolster applicability of this interfacial system. In an all thin-film $LaAlO_3/SrTiO_3$ system we identified two different conduction regimes, where the effect of oxygen partial pressure during growth directly affects the carrier density of the system. In the lower carrier density regime ($\sim 10^{13}$ cm^{-2}) we found a metallic to insulating temperature dependence and strong localization by disorder, whereas in the higher regime ($> 10^{14}$ cm^{-2}) we find metallic dependence with signs of weak localization. This is understood in the occupation of Ti $3d$ bands farther from the interface as carrier density is increased. Our work in the electronic properties of all-thin-film $LaAlO_3/SrTiO_3$ pioneers the understanding and implementations of this 2DEG to harness the richness of this oxide interface and its integration to industry standard substrates. Furthermore, we showed the first conducting $LaAlO_3/SrTiO_3$ two-dimensional system grown by the physical vapor deposition technique: 90° off-axis sputtering. Films grown with this scalable technique have excellent crystalline quality and transport characteristics similar to those grown by (mostly research employed) pulsed laser deposition. Writing of circuits on the nanoscale using conducting-tip atomic force microscopy is demonstrated in sputtered $LaAlO_3$ on $SrTiO_3$, opening the doors to nanoelectronic application of this novel interfacial system. Moreover, we are among the first groups in the world to demonstrate

conducting [111]-oriented $LaAlO_3/SrTiO_3$ heterostructures, a crystallographic orientation that proves to be challenging due to the large polar nature of perovskite oxides in this stacking direction. An interplay between structural and electronic reconstructions is at work to resolve the polarization divergence. This drives the $LaAlO_3/SrTiO_3$ (111) system from insulating to conducting with increasing $LaAlO_3$ thickness, displaying a broader transition than the conventional (001) system and a similar n-type 2DEG.

Acknowledgements

This dissertation is the culmination of six years of graduate work, along the way there were many people and institutions that directly or indirectly influenced me in a positive way to carry this academic phase to an end. First, I would like to thank my advisor Mark Rzchowski, whose insight was always keen and who taught me to look at all sides of the problem. I must also acknowledge the efforts of members of my group I collaborated with: David, Kellan and Meera; Adele Ruosi made working in the lab a much more enjoyable experience and was a mentor to me on the softer skills of life. A fruitful collaboration with Professor Chang Beom-Eom and his group in the Materials Science and Engineering department lead to many interesting research projects; it was always a pleasure to collaborate and discuss with Chung Wung Bark, Sangwoo Ryu, Jacob Podkaminer, Trevor Anderson and Ben Merten; and thanks to every member of that group who helped me transfer liquid helium at some point. I would also like to acknowledge all our collaborators in different groups and institutions: Michael Winokur here at UW-Madison, Hua Zhou and D.D. Fong at Argonne National Laboratory, X.Q. Pan's group at the University of Michigan, E.Y. Tsymbal's group at the University of Nebraska and J. Levy's group at the University of Pittsburgh.

My experience at the University of Wisconsin-Madison was more pleasant with the company of friends willing to get out of their labs and have a beer: Leon, John, Phil, Scott, Jon, Ian, Alex, Tien-Tien, Trevor. I learned all my basic physics at the University of Washington during my first year of graduate school. My comrades there were instrumental for keeping some resemblance of my mental sanity: Kamil, Liz, Eric, Scott,

Jae, Alex, Michael, Anders. I initiated my undergraduate studies at UTEP and would have graduated as an electrical engineer if it wasn't for Ramon E. Lopez, who, after our third midterm exam in a baby-physics course, thought it would be a good idea for me to study Physics instead. I joined Physics and his space physics research group the following summer, where I met many young people passionate about physics. Among them, Emilio, Jorge, Julian (not in order of preference) and I became lifelong friends and have kept each other motivated to continue forward. Throughout my education there were a handful of professors indispensable in my intellectual development: Piotr Wojciechowski, Ken Nollett, Mohamed Khamsi, Ramon Ravelo, Pavel Solin, Art Duval, Brent Fultz,

My love for Physics bloomed in high school, when I participated in the Physics Olympiad. Never in my life have I been as motivated to learn physics than then; the thrill for the competition was intoxicating and the problem solving skills I acquired then have proven invaluable throughout my life. My teachers Ildamar and Medrano started me up on academic competitions in Physics. Adriana Martel was the state delegate of the Olympiad, to me she became a teacher, a mentor and a friend. I would also like to thank all organizers and teachers, from the first exam in Juarez to the last one in Indonesia, and most all, to all my fellow students I competed with and against.

It is hard to put in words the immense support I have received from my family. My mother, with a strict but kind discipline, always ensured the best conditions for our education and development. My brother has been a kind soul and friend since the very beginning. My late father is responsible for the type of man I am today; honesty, decisiveness, fairness and diligence are qualities for which I couldn't have had a better role model for. My entire extended family has always been cheering for me, I appreciate

their support and encouraging words. I must also recognize my girlfriend Emilie, who has supported and tolerated me in every aspect during the dissertation writing ordeal, she has been compassionate and loving when I have most needed her.

List of Figures

List of Tables

Contents

Chapter 1

Introduction

In his 2000 Nobel Prize Lecture, Herbert Kroemer said:

Often it may be said *the interface is the device.*

Kroemer was receiving the prize "for developing semiconductor heterostructures used in high-speed- and opto-electronics." He pioneered the use of heterojunctions of conventional semiconductors from the II–V groups to develop widely used solid state devices such as the drift-field effect transistor and the double-heterostructure laser, the basis of all modern solid state diode lasers. Recently, *Nature Materials* published an editorial article titled *The interface is still the device*, highlighting the importance of recent advances in the fabrication of heterostructures using transition metal oxides [1]. Oxide interfaces provide a platform of diverse phenomena arising from the more complex electronic structure, e.g. magnetism, ferroelectricity and superconductivity. Indeed, complex oxide interfacial systems have shown electrostatically driven electronic reconstruction ($LaAlO_3/SrTiO_3$), ferromagnetic order ($LaMnO_3/SrMnO_3$), spin and orbital reconstructions ($CaMnO_3/CaRuO_3$), interface superconductivity ($LaAlO_3/SrTiO_3$ again) and fractional quantum Hall effect (ZnO/(MgZn)O) [2].

Almost 10 years after Ohtomo and Hwang's discovery of the two-dimensional electron gas (2DEG) at the $LaAlO_3/SrTiO_3$ heterointerface [3], the quest for new interfacial phenomena has been relentless, with field-effect tuning, superconductivity, ferromagnetism, Rashba spin-orbit coupling, strain-induced internal polarization, among others

populate the list. In this dissertation we expand the understanding of this 2DEG at $LaAlO_3/SrTiO_3$ by exploring aspects related to confinement, scalability, new growth techniques and realization in challenging crystal orientations that will further the applicability of this electron system to modern devices. This dissertation contains an overview chapter (Chapter 2) that briefly outlines the developments towards understanding the $LaAlO_3/SrTiO_3$ interfacial system. Following are three main chapters detailing several different projects I have worked on, discussing different aspects of the $LaAlO_3/SrTiO_3$ system. Each chapter is written in a 'stand-alone' manner and only assumes basic familiarity with oxide heterostructures and knowledge of condensed matter physics.

Chapter 3 treats the realization of the $LaAlO_3/SrTiO_3$ interface in an all thin-film realization, where 50 unit cells of $SrTiO_3$ are deposited onto $(LaAlO_3)_{0.3}$-$(Sr_2AlTaO_3)_{0.7}$ (LSAT) substrates. $LaAlO_3$ thin films are deposited on the $SrTiO_3$ layers to form the 2DEG. We were able to modulate the sheet carrier density of the 2DEG by using the $LaAlO_3$ growth parameters and we observed two different conduction regimes dependent on carrier density. Samples grown at high oxygen partial pressure (10^{-3} mbar) showed less carrier density and displayed strongly localized transport at low temperatures, whereas samples grown in lower oxygen partial pressure (10^{-4}–10^{-6} mbar) displayed greater sheet carrier densities and weakly localized behavior at low temperatures. We have argued that the additional carriers in the low-pressure samples begin to occupy subbands in Ti layers further from the $LaAlO_3/SrTiO_3$ interface that are less susceptible to interfacial disorder. In this project C. W. Bark in C. B. Eom's group fabricated the samples and the author (T. H.) in M. S. Rzchowski's group performed the magneto-transport experiments.

In Chapter 4 we show the creation of the first conducting two-dimensional electron system using sputtering as the deposition technique of $LaAlO_3$ on $SrTiO_3$. We found excellent crystalline quality of the deposited $LaAlO_3$ films and that the 2DEG formed displays similar transport properties compared to the commonly pulsed laser deposition grown films. Furthermore, conductive tip atomic force microscopy writing and erasing was demonstrated on these samples. For this project J. P. Podkaminer in C.B. Eom's group grew and characterized the structures by x-ray diffraction; the author (T. H.) performed magnetotransport characterization and M. Huang in J. Levy's group at the University of Pittsburg demonstrated the nano-writing capabilities.

In Chapter 5 we explore the structural and electronic properties of heterostructures of $LaAlO_3$ grown on $SrTiO_3$ in the [111]-direction. Viewed along the [111] direction, both materials are polar, with a layer polar charge per cell of $\pm 4e$ for Ti-SrO_3 bilayers and $\pm 3e$ for Al-LaO_3. Furthermore, the (111) surface of a pseudo cubic lattice provides a hexagonally coordinated template that opens the possibility to generate topologically protected electronic states. By analyzing the bare $SrTiO_3$ substrate in the (111) orientation with surface x-ray diffraction and coherent Bragg rod analysis (COBRA) we identified an initial reconstruction and off-stoichiometry that alleviates the internal field of this layer-by-layer polar single crystal. Similar analysis and transmission electron microscopy (TEM) imaging on $LaAlO_3/SrTiO_3$ (111) indicate slight intermixing and perfect stacking of AO_3-B bilayer across the interface. This interface shows polar electronic reconstruction as in the (001) case, supported by direct observation of n-type carriers in magnetotransport measurements and density functional theory (DFT) calculations. In this project, the sample fabrication was led by S. Ryu in C. B. Eom's lab, surface x-ray diffraction and COBRA was done by H. Zhou and D. D. Fong at Argonne

National Laboratory. The author (T. H.) and M. S. Rzchowski performed magneto-transport characterization, TEM was performed in X.Q. Pan's group at the University of Michigan and DFT calculations were performed by E.Y. Tsymbal's group at the University of Nebraska.

Chapter 2

Background

2.1 The $LaAlO_3/SrTiO_3$ (001) Interface

In 2004, Ohtomo and Hwang began a new era in thin-film oxide physics when they published "A high-mobility electron gas at the $LaAlO_3/SrTiO_3$ heterointerface" [3]. They showed that the epitaxial growth of $LaAlO_3$ on $SrTiO_3$ (001) by pulsed laser deposition (PLD) created a conducting interface when the substrate had a TiO_2 termination (structure shown in Fig. 2.1b). The SrO termination, achieved by the deposition of a single monolayer of Sr on the TiO_2 terminated substrate, yielded an insulating interface (Fig. 2.1d). Their layer-by-layer growth was monitored using reflection high-energy electron diffraction (RHEED). Their reported mobilities saturated at values over 10,000 cm^2/Vs and their legendary sheet carrier densities ranged from 10^{14} to 10^{17} cm^{-2}, with high dependence on the growth oxygen partial pressure and post-annealing treatments [3]. They attributed the conduction mechanism to the abrupt polarity discontinuity across the interface. In the [001] oriented perovskites, these oxides are composed of SrO/TiO_2 and LaO/AlO_2 for $SrTiO_3$ and $LaAlO_3$ respectively. Simple counting of the oxidation states of each element shows that $SrTiO_3$ is composed of neutral monolayers whereas $LaAlO_3$ is formed of polar monolayers with $\pm e$ charge per unit cell, where e is the fundamental charge. In this way, they argue, the interface will have an excess $\pm e/2$ electrons per two-dimensional unit cell [3].

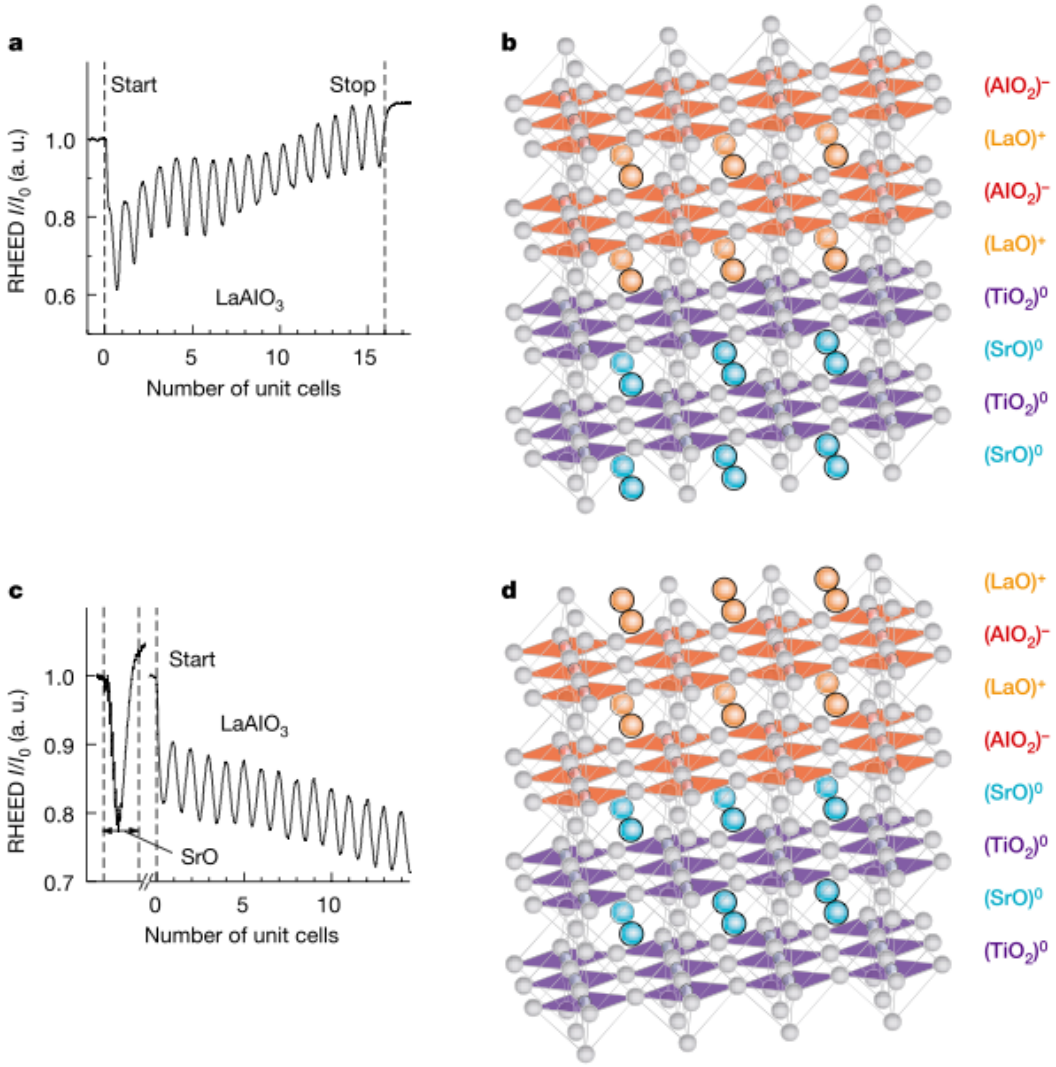

Figure 2.1: Growth of the first $LaAlO_3/SrTiO_3$ Heterointerface. (a) RHEED intensity of the deposition of $LaAlO_3$ on TiO_2 terminated $SrTiO_3$. (b) Schematic of the LaO/TiO_2 interface. (c) RHEED intensity of the deposition of a single SrO layer and $LaAlO_3$ on TiO_2 terminated $SrTiO_3$. (b) Schematic of the AlO_2/SrO interface. Reproduced from Ref. [3] with permission from Nature Publishing Group.

2.2 The Components: $SrTiO_3$ and $LaAlO_3$

Both $SrTiO_3$ and $LaAlO_3$ are band insulators with gaps ~ 3.2 eV and ~ 5.6 eV respectively. They both have the general perovskite ABO_3 structure, with a primitive cubic unit cell with the A cations at the edges, a B cation at the center and and O anion at each of the faces (see Fig. 2.2). It is relevant to note that the substrate, $SrTiO_3$, has the perfect cubic symmetry at room temperature with lattice constant $a = 3.905$ Å and undergoes a structural phase transition from cubic to tetragonal at $T = 105$ K. Its dielectric function appears to diverge with decreasing temperature, but saturates at a high value near $T = 4$ K and does not become ferroelectric. Quantum fluctuations at low temperatures are responsible for stabilizing the structure and preventing the transition [4]. Because of this, $SrTiO_3$ is often called an *incipient ferroelectric* or a *quantum paraelectric* [5]; however, a ferroelectric phase has been found in $SrTiO_3$ thin films [6–10]. On the other hand, $SrTiO_3$ is typically paramagnetic but ferromagnetic phases have been reported in La and Fe doped, oxygen reduced $SrTiO_{3-\delta}$ thin films [11].

2.3 Creation of the Conducting Channel

The mechanism for the creation of this two-dimensional electron system due to polarization discontinuity was soon extended by Nakagawa et al. in which the electrostatic potential builds up from the interface due to each set of charged $LaAlO_3$ polar layers; the divergence of this potential forces a reconstruction, either electronic or structural [12]. In their paper, Nakagawa et al. considered the oxidation states of each of the components of the materials: seen in the [001] orientation, $SrTiO_3$ is composed of sets of $Sr^{2+}O^{2-}$ and $Ti^{4+}O_2^{4-}$ neutral monolayers, whereas $LaAlO_3$ is formed by polar set of $La^{3+}O^{2-}$ and $Al^{3+}O_2^{4-}$ monolayers [12]. On TiO_2 terminated $SrTiO_3$ substrates, the

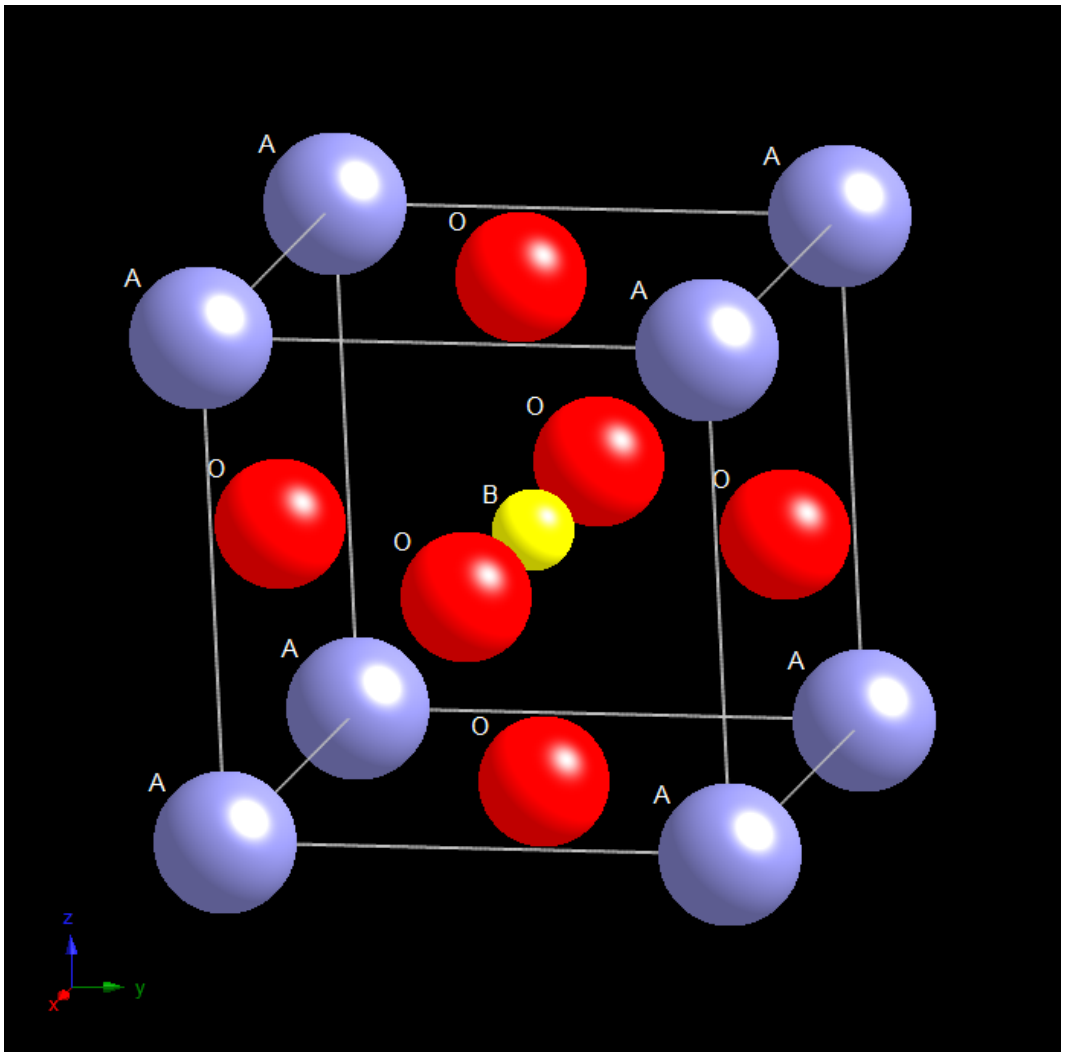

Figure 2.2: Perovskite unit cell. The blue, yellow and red spheres correspond to the A, B and O atoms.

interface structure is $SrO/TiO_2/LaO$ and the electric fields create a positive, diverging potential as with increasing number $LaAlO_3$ layers above the interface (see Fig. 2.3a). This potential divergence can be prevented by having a charge of $-e/2$ per unit cell at the interface, which can be accommodated due to the mix valance of Ti (+3 or +4) (see Fig. 2.3b); this type of termination is often denominated an *n-type interface*. Conversely, in the SrO terminated case the interface will be $TiO_2/SrO/AlO_2$ and the diverging potential will have the opposite sign (see Fig. 2.4a); the divergence is prevented by transferring a charge of $+e/2$ to the interface which can be hosted by oxygen vacancies at the SrO monolayer (see Fig. 2.4b), this is often called a *p-type interface*. In this way, an n-type interface leads to an electronic reconstruction and a p-type one to a structural reconstruction. They supported these claims with evidence from electron energy loss spectroscopy, which also showed the reconstruction mechanisms in both cases to have a spatial extent of a few nanometers [12]. They also observed interface roughness and cation intermixing in the n-type interface via scanning transmission electron microscopy and electron energy loss spectroscopy, and argued that intermixing was a mechanism to reduce the interfacial dipole moment, not necessary in the p-type interface due to the lack of delocalized screening electrons [12].

This electrostatic potential divergence mechanism is termed *polarization catastrophe*. An indication of a polarization divergence was the existence of a critical thickness (4 unit cells of $LaAlO_3$) above which the $LaAlO_3/SrTiO_3$ interface becomes conducting [13]. This observation has been reproduced in many laboratories and it is considered to be a direct indicator of electronic reconstruction induced by the polarization catastrophe scenario. Due to the interfacial nature of this electron gas and its narrow confinement it was denominated a 'two-dimensional electron gas' (2DEG) [13, 14]. Since 2006, many studies have attempted to explain the creation mechanism of the 2DEG at

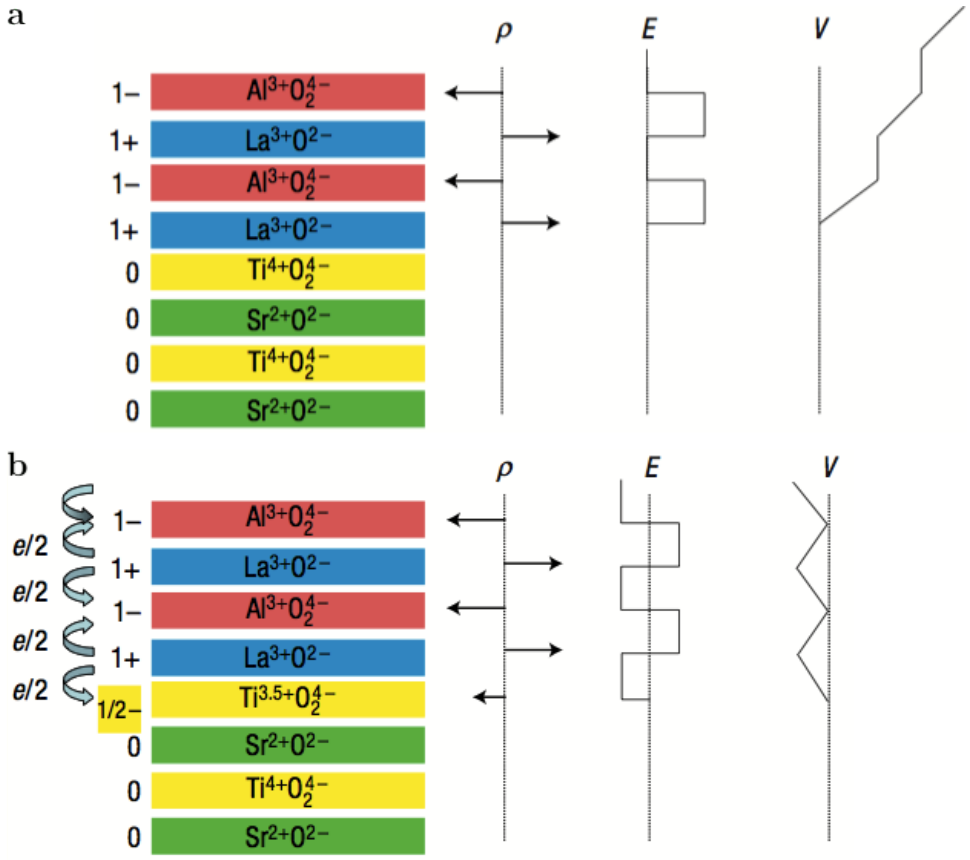

Figure 2.3: Polarization catastrophe of a $LaAlO_3$ film on a TiO_2 terminated $SrTiO_3$ substrate. (a) Unreconstructed interface. (b) Avoidance of the potential divergence by a transfer of -$e/2$ charge to the interface. Reproduced from Ref. [12] with permission from Nature Publishing Group.

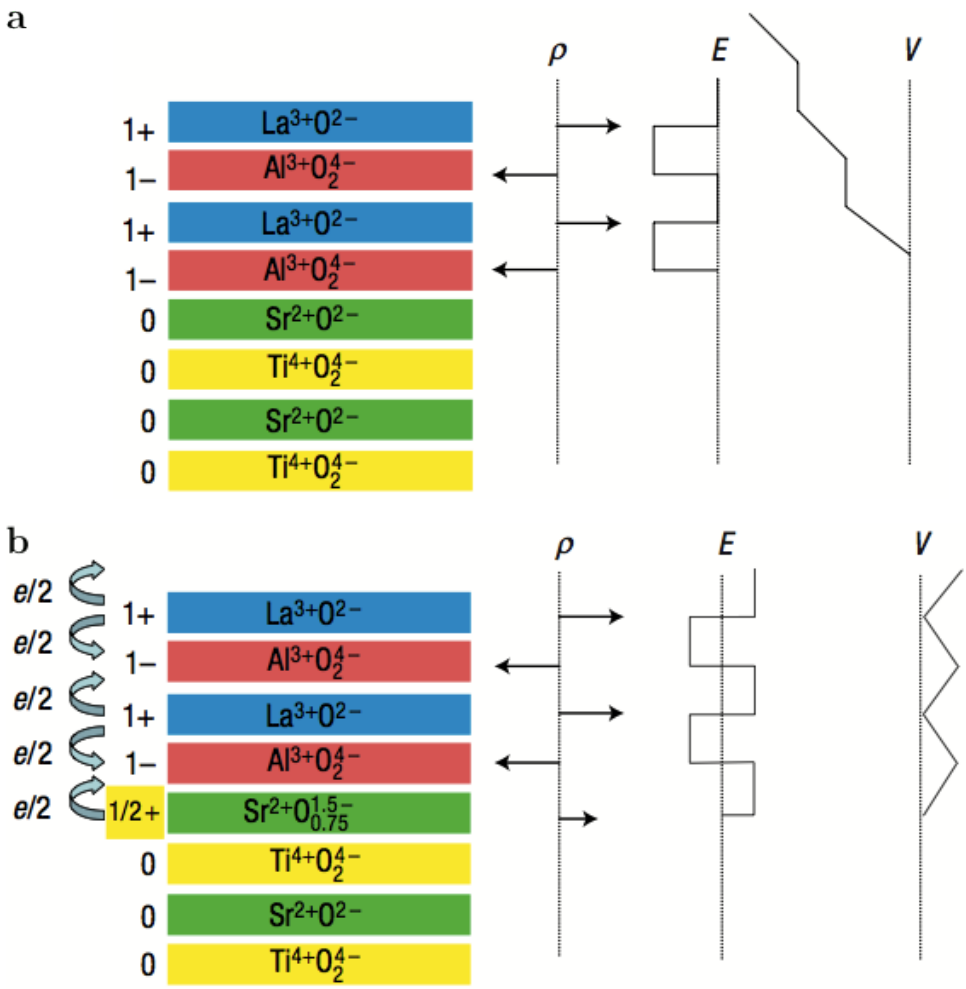

Figure 2.4: Polarization catastrophe of a $LaAlO_3$ film on a SrO terminated $SrTiO_3$ substrate. (a) Unreconstructed interface. (b) Avoidance of the potential divergence by a transfer of $+e/2$ charge to the interface.. Reproduced from Ref. [12] with permission from Nature Publishing Group.

the $LaAlO_3/SrTiO_3$ heterointerface, and besides the polarization catastrophe scenario another two main mechanisms are amply discussed: oxygen vacancy doping and cation intermixing.

It is well known that $SrTiO_3$ can be n-doped by reduction, i.e. the creation of oxygen vacancies to form $SrTiO_{3-\delta}$ [15–23]. Oxygen vacancies produced during the highly-energetic process of PLD deposition, the main fabrication technique of $LaAlO_3/SrTiO_3$ structures, cause unintentional δ-doping of the top surface of the $SrTiO_3$ substrate [24–27]. Herranz et al. conducted a study on PLD grown samples in a variety of oxygen atmospheres and compared them to previously reduced and doped $SrTiO_3$, concluding by comparison, that the conduction channel is formed solely by oxygen vacancy doping [26]. The variability of the transport properties on growth conditions is well documented, for example in Ref. [28] and in Ohtomo and Hwang's original paper [3]; further, we have taken advantage of this fact to modulate the carrier density in order to probe different conduction and localization regimes in all-thin-film $LaAlO_3/SrTiO_3$ heterostructures [29] (more on this in Chapter 3). It is also widely accepted that transport properties vary even between different laboratories using the same nominal conditions; an excellent summary of this variability is presented in the review article by Chen et al. [30]. Another indication that oxygen vacancies create the conducting channel are a variety of high-mobility 2DEGs formed on bulk or thin film $SrTiO_3$ for example: Ar^+ irradiated single crystal $SrTiO_3$ [31–33], HF treated and O_2-atmosphere annealed $SrTiO_3$ single crystals [34], and oxygen reduced $SrTiO_3$ thin films grown homoepitaxially by PLD [35].

The other commonly discussed explanation for the existence of conduction at the $LaAlO_3/SrTiO_3$ heterointerface is cation intermixing. First observed by Nakagawa et al. [12], they explained intermixing as mechanism necessary to compensate the interfacial electric dipole. Using surface x-ray diffraction and coherent Bragg rod analysis,

Willmott et al. observed cation intermixing across three unit cells at the interface of five unit cells of $LaAlO_3$ on $SrTiO_3$ structures deposited by PLD [36]. Their analysis shows a non-abrupt interface that contains one to two $La_{1-x}Sr_xTiO_3$ layers with $x = 0.86 - 0.70$. Lanthanum doped strontium titanate ($La_{1-x}Sr_xTiO_2$) is known to be conducting in the doping range $x = 0.05 - 0.95$ [37–39]. Thus, the conductivity across the $LaAlO_3/SrTiO_3$ interface could be caused by a layer of La-doped $SrTiO_3$. Kalabukhov et al. showed with medium-energy ion spectroscopy, which is sensitive to La and Sr one unit cell into the surface, of $LaAlO_3$ films with thicknesses 1–8 unit cells that there is significant intermixing in the first three layers of $LaAlO_3$ [40]. Furthermore, Chambers et al. provide large amounts of evidence using medium-energy ion spectroscopy, electron energy loss spectroscopy, and angle-resolved x-ray photoelectron spectroscopy that $LaAlO_3/SrTiO_3$ heterostructures grown in typical conditions show some degree of La-Sr intermixing [41]. Density functional theory calculations show that this intermixing is energetically favorable and they argue that La-doped $SrTiO_3$ is the main mechanism for the creation of the conducting interface [41]. Chambers also wrote an article in which he reviews the main effects observed in the $LaAlO_3/SrTiO_3$ system and explains them in terms of a cation intermixed interface [42].

2.4 Two-dimensional Character

Regardless of the on-going debate on the source of carriers, the $LaAlO_3/SrTiO_3$ heterointerface displays a conductive n-type system with large two-dimensional character. Hard x-ray photoelectron spectroscopy experiments showed that this 2DEG is confined to one or a few unit cells below the interface [43]. Infrared ellipsometry determined the depth profile to have an initial decay over 2 nm and long tail extending 11 nm below the interface and carrier densities consistent with transport measurements [44]. Optical second harmonic generation measurements found mobile carriers occupying the Ti $3d$ bands and determined two different electronic arrangements for thicknesses above and below the $LaAlO_3$ critical thickness [45]. The occupation of Ti $3d$ bands was furthermore predicted through density functional theory (DFT) calculations [46, 47].

In the case of $SrTiO_3$, the Sr cation has a larger atomic radius with a closed s shell, the Ti cation has a smaller atomic radius and partly filled d band. Therefore, the electronically available states of the Ti states interact with the O $2p$ bands. The perovskite structure is usually visualized as formed by a cubic lattice made by the Sr ions and a TiO_6 octahedron formed by the Ti at the center and the O atoms at the faces of the cube (see Fig. 2.5). The crystal field of this octahedral coordination creates a splitting in the Ti $3d$ bands (d_{xy}, d_{xz}, d_{yz}, d_{z^2} and $d_{x^2-y^2}$), into degenerate, lower level, t_{2_g} bands (d_{xy}, d_{xz}, d_{yz}) and higher level, degenerate e_g bands (d_{z^2} and $d_{x^2-y^2}$) [48, 49].

Using x-ray adsorption spectroscopy, Salluzzo et al. found that mobile electrons first occupy the Ti $3d_{xy}$ bands, suggesting that there is further splitting of the t_{2_g} bands due to the symmetry breaking caused by the interface [50]. Delugas et al. provided a theoretical framework in which the layer-by-layer band occupation depends on the density of mobile carriers. According to their DFT calculations, occupation starts in the d_{xy} band of the first TiO_2 layer (from the interface down) and as carrier density is

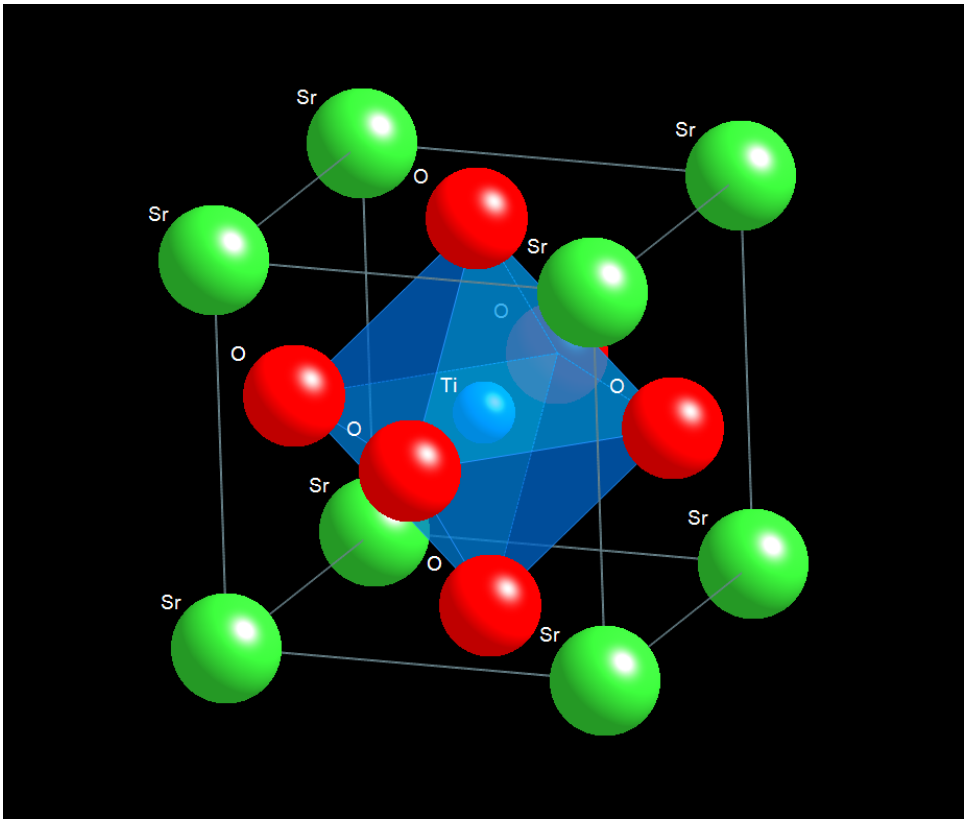

Figure 2.5: Octahedral coordination of the Ti ion with the six O atoms within the perovskite cell.

increased d_{xy} bands further from the interface begin to be occupied. Above a carrier density of $n_s \sim 10^{14}$ cm^{-2} the rest of the t_{2_g} bands become occupied [51].

The observation of superconductivity on this two dimensional electron gas provides an upper bound on the spatial confinement. Reyren et al. discovered a superconducting state on $LaAlO_3/SrTiO_3$ below $T = 200$ mK, the dependence of the sheet resistance with temperature across the transition was consistent with the Berezinskii-Kosterlitz-Thouless model for two-dimensional superconducting systems. By comparison to the theory they estimated that the upper bound of the confinement to be ~ 10 nm [52]. In a different magnetotransport study, Caviglia et al. showed Shubnikov-de Haas oscillations with a period that depends only on the perpendicular component of the magnetic field, an indication of a quantum coherent electron gas with planar confinement [53].

2.5 Potential for Applications

The $LaAlO_3/SrTiO_3$ Interface provides an incredibly rich system for potential applications. Most notable are the electric field effects on many of the properties of this electron gas, very likely caused by the dielectric dependence of the $SrTiO_3$ substrate. Reported field-effect phenomena include: transistor like modulation from insulating to conducting states with applied gate voltage [13], electric field control of the superconducting state [54], modulation of mobility of the 2DEG with gate voltage [55], tunable Rashba spin-orbit interaction [56, 57], carrier depletion driven metal-insulator transition [58], among others.

Microlithography of patterns on these heterostructures was first demonstrated by Schneider et al. in 2006 [59], and the role of polar adsorbates, commonly used in lithographic processes, was studied by Xie et al. [60]. Furthermore, lateral confinement to widths of 500 nm of $LaAlO_3/SrTiO_3$ preserved the two-dimensional character and superconductivity of the electron gas [61]. Another technique explored is the writing of conducting patterns as thin as a few nanometers on insulating $LaAlO_3/SrTiO_3$ structures (just below the critical thickness) using conductive-tip atomic force microscopy (c-AFM) (see Fig. 2.6) [62].

Another important issue to consider when discussing applicability of the $LaAlO_3/SrTiO_3$ system is scalability, where two main limitations arise: commercial availability of large substrates and the growth technique. Even though $SrTiO_3$ provides a good platform for field-effect sensitive devices, commercially available single crystal $SrTiO_3$ substrates are limited to areas of 10×10 mm. Park et al. demonstrated conductivity at the interface of $LaAlO_3/SrTiO_3$ thin films (in contrast with the widely studied $LaAlO_3$ thin film on an $SrTiO_3$ single crystal substrate) grown on Si, and that c-AFM nanowriting is possible in these all-thin-film structures [63]. Bark et al. further

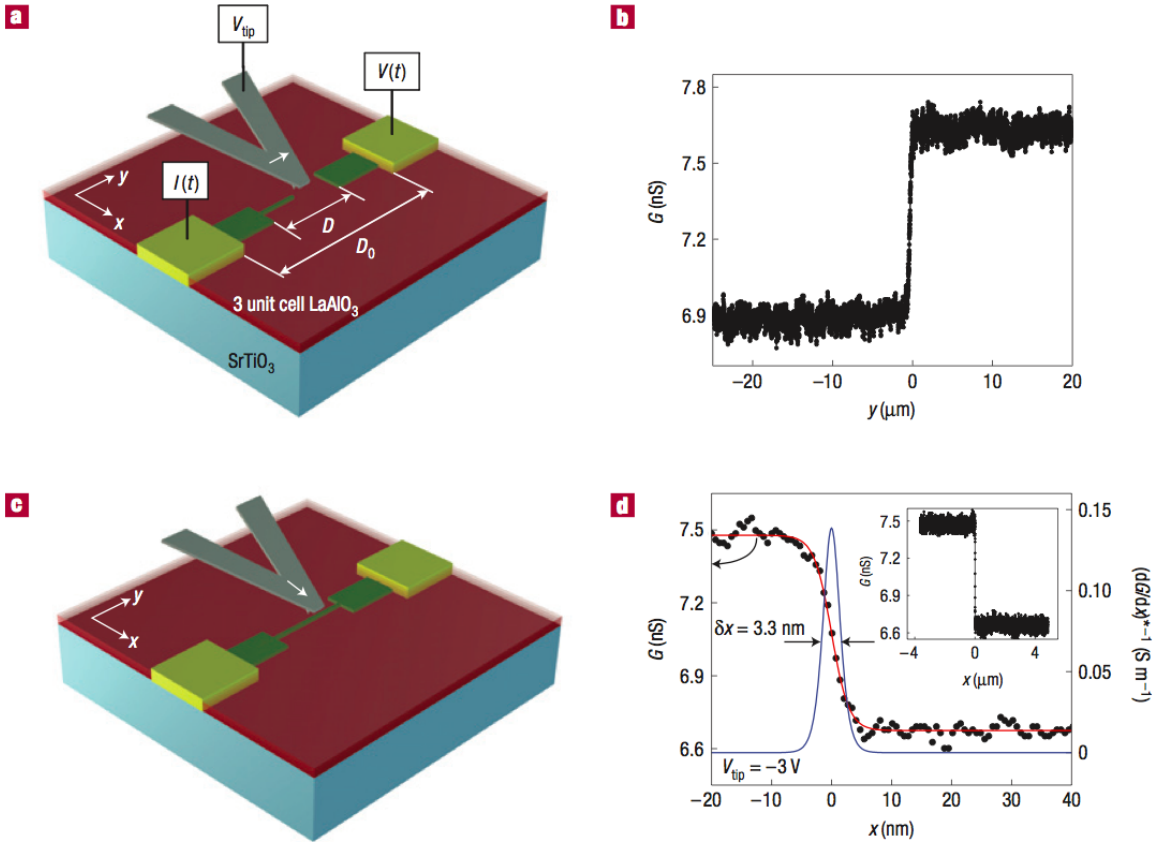

Figure 2.6: Nanowriting and erasing of conductive channels on 3 unit cell thick $LaAlO_3$ on $SrTiO_3$. (a) Writing of the conductive nanowire and (b) conductivity monitoring showing a jump upon completion of the wire. (c) Erasing of the conductive nanowire and (d) conductivity decrease upon finishing the erase process. Reproduced from Ref. [62] with permission from Nature Publishing Group.

studied the effect of substrate strain on all-thin-film $LaAlO_3/SrTiO_3$ 2DEGs and found that only compressively strained systems (on Si, $(LaAlO_3)_{0.3}$-$(Sr_2AlTaO_3)_{0.7}$ (LSAT) and $NdGaO_3$ substrates) show conductive interfaces [64]. We further investigated the transport mechanisms on $LaAlO_3/SrTiO_3$ thin films grown on LSAT substrates, finding different conducting regimes not observed in the single crystal $SrTiO_3$ systems (see Ref. [29] or Chapter 3). Furthermore, the most common deposition technique for these oxide structures, PLD, provides only a small area of uniform coverage. Attempts to replicate the epitaxial $LaAlO_3/SrTiO_3$ interface been made using more scalable techniques like sputtering failed to yield a conducting 2DEG [65, 66]. Our collaboration has demonstrated the first conducting 2DEG fabricated by sputtering film deposition, with similar transport properties and nanowriting capabilities to PLD grown $LaAlO_3$ on $SrTiO_3$ (see Ref. [67] or Chapter 4).

In this brief background review we attempted to show the richness of the 2DEG at the $LaAlO_3/SrTiO_3$ heterointerface in both physical properties and progress towards its future applicability. We began by discussing the discovery of the system and the initial observations, then we reviewed few structural, electric and magnetic properties of the main components. We proceeded to summarize the proposed mechanisms for the creation of the 2DEG, highlighting the still ongoing debate. Lastly, we reviewed the experimental and theoretical studies, of the two-dimensional nature and band occupation of the electron gas and overview the diverse efforts to develop the applicability of this promising system.

Chapter 3

Two-dimensional Electron Gas Between $LaAlO_3$ and $SrTiO_3$ Thin Films

Measurements of the 2DEG spatial extent indicate a dense sheet of carriers, 2–4 nm thick, decaying into the $SrTiO_3$ layer [43–45]. Carriers occupy the $SrTiO_3$ Ti $3d$ bands near the interface [43, 50], which are split by crystal field and structural distortions [50]. The octahedral coordination of the Ti cation with the O atoms is responsible for splitting the $3d$ band into a low energy triplet t_{2_g} (d_{xy}, d_{yz} and d_{xz} subbands) and a higher-energy doublet e_g (d_{z^2} and $d_{x^2-y^2}$). The interface between $LaAlO_3$ and $SrTiO_3$ introduces a symmetry break along the z-direction, further splitting the t_{2_g} triplet into a lower d_{xy} subband and a higher d_{xz} and d_{yz} doublet [47, 50, 51].

The lowest conduction band of Ti $3d$ states is the d_{xy} subband of the first TiO_2 layer [51], which has strong two-dimensional character, and hence is susceptible to disorder driven localization. As more carriers are introduced to the system, they occupy d_{xy} subbands spread over several TiO_2 layers away from the interface [51], making them less susceptible to localization by interfacial disorder [47]. Carriers in the higher-energy d_{xz} and d_{yz} bands are more prone to localization on the other hand, because of their large effective mass in the xy plane. These three-dimensional subbands are occupied when

the surface carrier density exceeds 10^{14} cm^{-2}, as well as d_{xy} bands in deeper TiO_2 layers [51].

A better understanding of these oxide 2DEGs can be achieved by controlling both the $LaAlO_3$ and $SrTiO_3$ layer properties, through growth of all-thin-film $LaAlO_3/SrTiO_3$ heterostructures on bulk substrates. Substrate choice provides the opportunity to manipulate the interfacial 2DEG. Electron transport at the $LaAlO_3/SrTiO_3$ interface has been reported for heterostructures grown on Si [63], $(LaAlO_3)_{0.3}$-$(Sr_2AlTaO_3)_{0.7}$ (LSAT) [64, 68] and $NdGaO_3$ [64]. This approach can lead to several effects, including increased interfacial disorder when growing on an additional interface, strain effects introduced by substrate misfit, a different interfacial structure, and different Ti 3d band occupations.

Effects of disorder on transport in the $LaAlO_3/SrTiO_3$ interfacial system have been reported previously. Charged dislocation cores were suggested to be responsible for increased resistance and lower mobilities [69], and weak localization effects were identified through magnetotransport measurements [56, 70]. A reduction of mobility in field effect experiments was attributed to confinement of carriers closer to the disordered interface, increasing scattering [55]. Moreover, a metal-insulator transition tuned by field effect was suggested to arise from disorder-induced localization or strong Coulomb interactions [58].

Misfit strain of $SrTiO_3$ layers grown on different substrates can change its crystallographic phase and band structure. Strain in thin film $SrTiO_3$ has been preported to increase mobility by 300% [71], attributed mainly to band structure changes. Variations of carrier concentration in $LaAlO_3$ on thin-film $SrTiO_3$ structures have been attributed to a strain-induced electric polarization in the $SrTiO_3$ layer [64]. In addition, theory predicts complex structural phases in strained thin film $SrTiO_3$ [6], and indications of these phases have been observed [72].

We present a magnetotransport study of epitaxial thin-film $LaAlO_3/SrTiO_3$ on LSAT substrates, demonstrating strongly localized transport at low temperatures on structures with $LaAlO_3$ layers grown at high (10^{-3} mbar) oxygen partial pressures (p_{O_2}). Increased carrier concentration and metallic behavior is observed in samples where the $LaAlO_3$ layer was grown at lower p_{O_2} (10^{-4}–10^{-6} mbar). This leads to the occupation of subbands in Ti layers further from the $LaAlO_3/SrTiO_3$ interface that are less susceptible to the strong interfacial disorder. We support this interpretation with low temperature magnetoresistance measurements. This chapter follows closely our published results in Ref. [29].

3.1 Growth and Characterization

Epitaxial $LaAlO_3$ and $SrTiO_3$ thin films were grown on (001) LSAT substrates by Pulsed Laser Deposition (PLD) by C. W. Bark in C. B. Eom's group. The low miscut ($< 0.05°$) LSAT substrates were treated by a modified buffered hydrofluoric acid etch and annealed in oxygen to create atomically smooth surfaces with unit cell step. The substrates were then attached to a resistive heater and positioned $5.0 \sim 6.0$ cm from the target. A KrF excimer laser (248 nm) beam was focused on stoichiometric $LaAlO_3$ and $SrTiO_3$ single-crystal targets with an energy density of $2.0 \sim 2.5$ J/cm^2 and pulsed at $3 \sim 5$ Hz. The PLD system is equipped with a high-pressure Reflection High-Energy Electron Diffraction (RHEED) system, which enabled in situ monitoring of atomic layer controlled growth. The $SrTiO_3$ layers of 50 unit cell (uc) thickness were grown at a substrate temperature of 750°C and an oxygen partial pressure of 1 atm, and then etched using buffered hydrofluoric acid for $30 \sim 90$ s to maintain Ti-termination after growth $SrTiO_3$ layer. The three-dimensional strain state of the films was determined

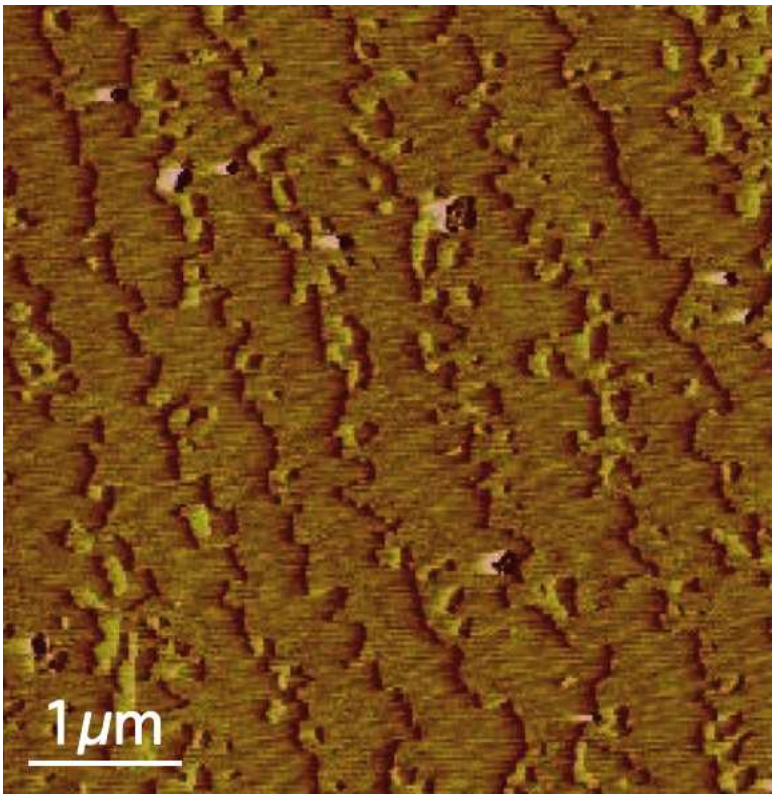

Figure 3.1: Atomic Force Microscopy image of the $SrTiO_3$ film after buffered hydrofluoric etching and annealing.

using high-resolution four-circle X-ray diffraction in a Bruker D8 Advance system. The $SrTiO_3$ layer was fully coherent and compressively strained by -0.96% [64]. Furthermore, the 0.003° width of the thin-film $SrTiO_3$ out-of-plane rocking curve was much narrower than the 0.035° measured for the $SrTiO_3$ substrate, suggesting superior crystal quality. Film surfaces were imaged with an Atomic Force Microscopy (AFM) system by Veeco and show atomically sharp terraces after the etching and annealing steps (Fig. 3.1).

The $LaAlO_3$ films were grown on top of the $SrTiO_3$ layers at 550°C at oxygen pressures of 10^{-3}, 10^{-4}, and 10^{-6} mbar. The heterostructures studied (schematically shown in Fig. 3.2) have an overlayer of 15 to 20 unit cells (uc) of $LaAlO_3$ on a 50 uc $SrTiO_3$ thin film on LSAT (001). After deposition, the samples cooled down to room temperature

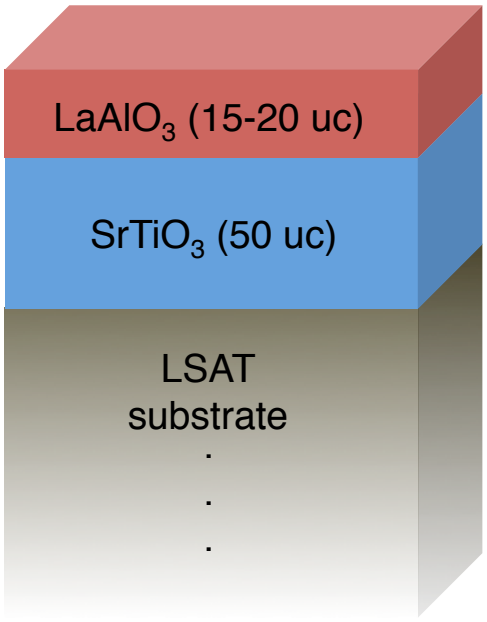

Figure 3.2: Schematic of the $LaAlO_3/SrTiO_3$/LSAT heterostructures.

in the same oxygen atmosphere. The RHEED patterns during growth of the two films (Fig. 3.3) remained similar to that observed on the bare LSAT substrate indicating grown films maintained the substrates crystallographic phase. The RHEED intensity during growth of the $LaAlO_3$ layer displays clear oscillations, as seen in Fig. 3.4, indicating layer-by-layer controlled growth.

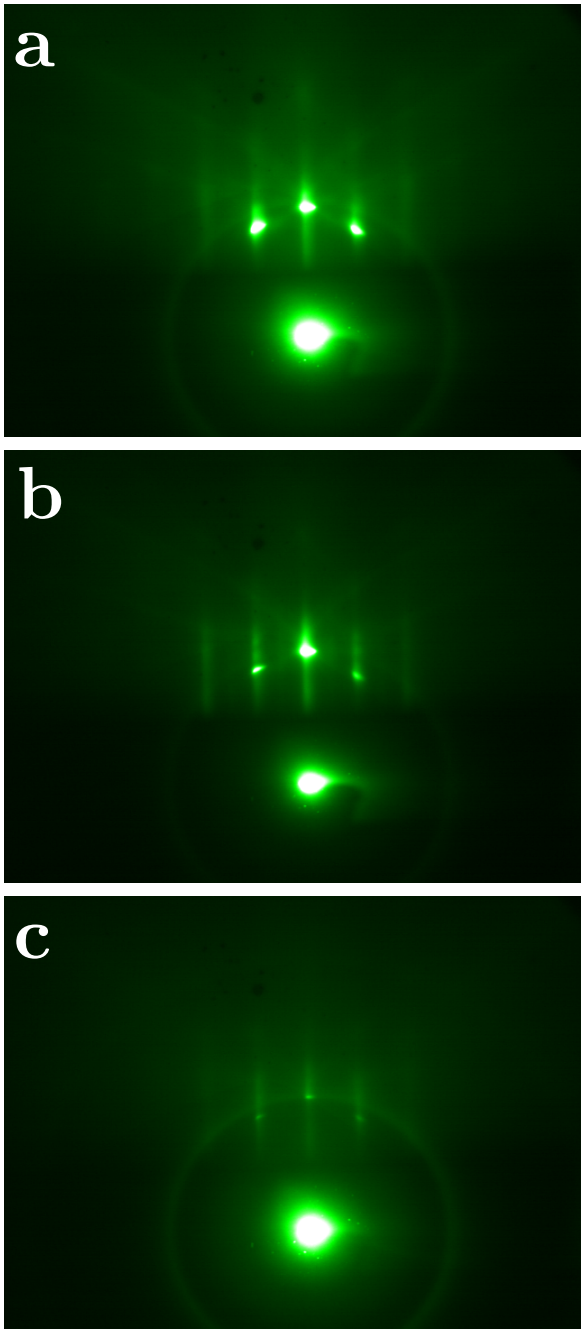

Figure 3.3: Reflection High-Energy Electron Diffraction patterns during the deposition process. (a) Bare LSAT substrate. (b) After growth of $SrTiO_3$ layer. (c) After growth of $LaAlO_3$ layer.

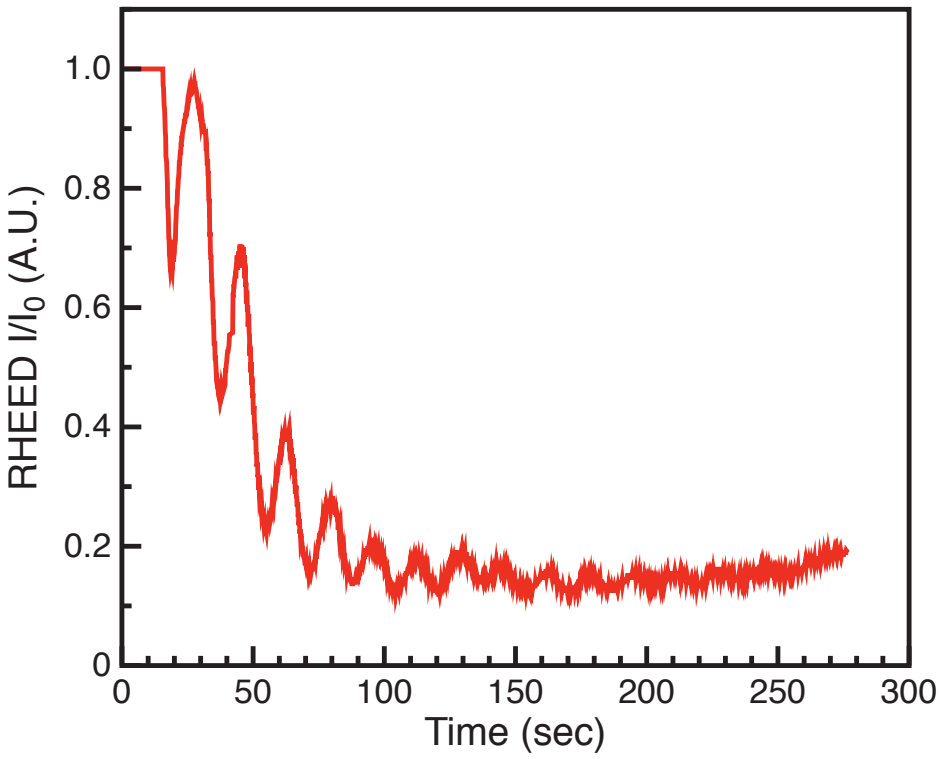

Figure 3.4: Reflection High-Energy Electron Diffraction oscillations during deposition of the $LaAlO_3$ layer on the $SrTiO_3$ thin film.

We bonded aluminum wires directly at the sample corners and we determined sheet resistance (R_s), Hall coefficient (R_H), and magnetoresistance (MR) given by:

$$\frac{\Delta R_s(H)}{R_s(0)} = \frac{R_s(H) - R_s(0)}{R_s(0)} \tag{3.1}$$

using the van der Pauw technique [73]. Electrical transport was measured using a Keithley 2400 Sourcemeter to source bias currents and measure potential drops, and a Keithley 2700 Data Acquisition unit to automatically switch and connect between the different configurations. We cooled the samples in an Oxford Instruments MagLab 2000 liquid helium, sample in flowing gas, cryostat with an integrated superconducting magnet. The temperature range measured was between 300 and 3 K, with maximum magnetic fields of $\mu_0 H = 8.3$ T. The Hall voltages were linear as a function of magnetic field indicating single band transport; thus the two-dimensional carrier concentrations (n_s) and Hall mobilities (μ_H) were calculated according to:

$$n_s = -\frac{1}{eR_H} \tag{3.2}$$

$$\mu_H = \frac{1}{en_s R_s} \tag{3.3}$$

where e is the fundamental charge.

3.2 Strong Localization in High-pressure Samples

The samples grown at 10^{-3} mbar (high-pressure samples) with $LaAlO_3$ thicknesses of 20 and 15 uc showed metallic behavior at high temperatures and an upturn in R_s near $T = 100$ K. At $T = 3$ K the samples reached values as high as 5×10^5 $\Omega/\square$ in the 20 uc sample and 2×10^6 $\Omega/\square$ in the 15 uc sample, as seen in Fig. 3.5. These low temperature sheet resistances were much higher than the quantum of resistance $h/e^2 = 25.8$ kΩ, suggesting strong localization and a hopping conduction mechanism as opposed to semiclassical transport.

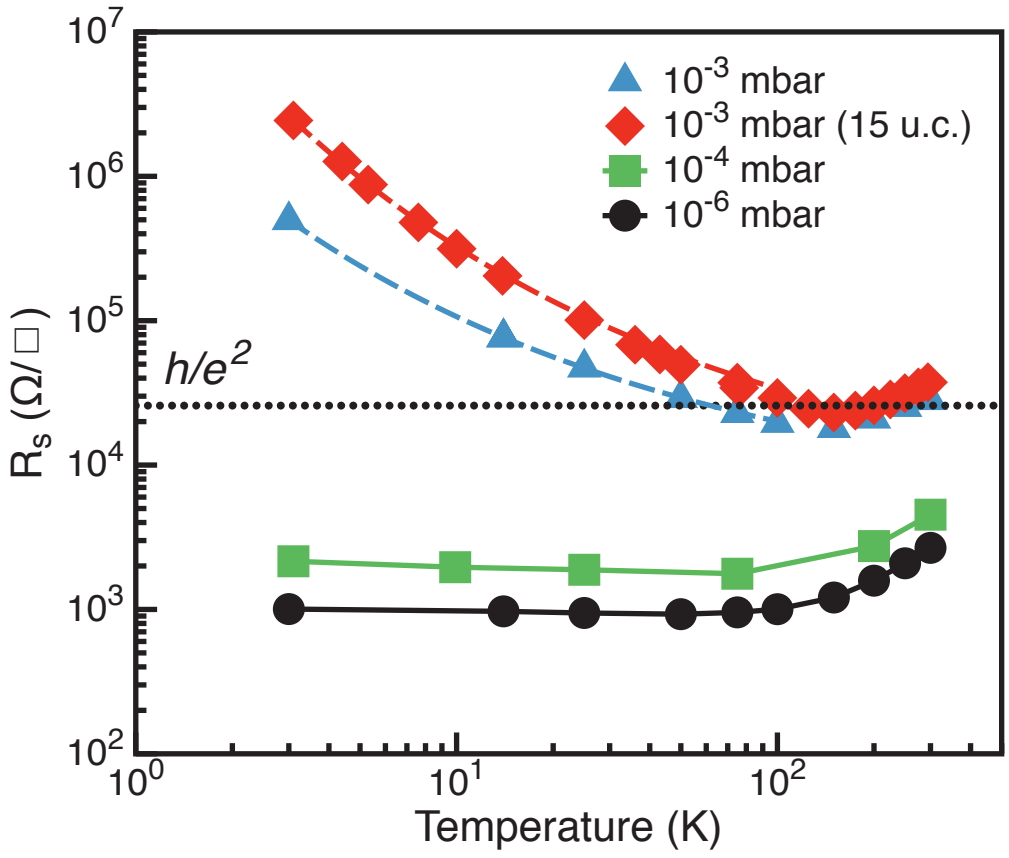

Figure 3.5: Temperature dependence of R_s in $LaAlO_3/SrTiO_3$ films on LSAT substrates. Dashed lines show fits for the Mott type VRH model.

In order to identify the localization mechanism at work we plotted the logarithm of the sheet conductivity of these samples as a function of three powers (α) of temperature, as seen in Figures 3.6 and 3.7. The exponent $\alpha = -1/2$ corresponds to the Efros-Shklovski type variable range hopping (VRH) mechanism, with a characteristic temperature dependence:

$$\rho = \rho_0 \exp\left[(T_0/T)^{1/2}\right] \tag{3.4}$$

whereas the exponents $\alpha = -1/3$ and $\alpha = -1/4$ correspond to Mott type VRH [74]:

$$\rho = \rho_0 \exp\left[(T_0/T)^{1/(d+1)}\right] \tag{3.5}$$

where d is the dimensionality of the system, thus corresponding to $d = 2$ and $d = 3$ respectively.

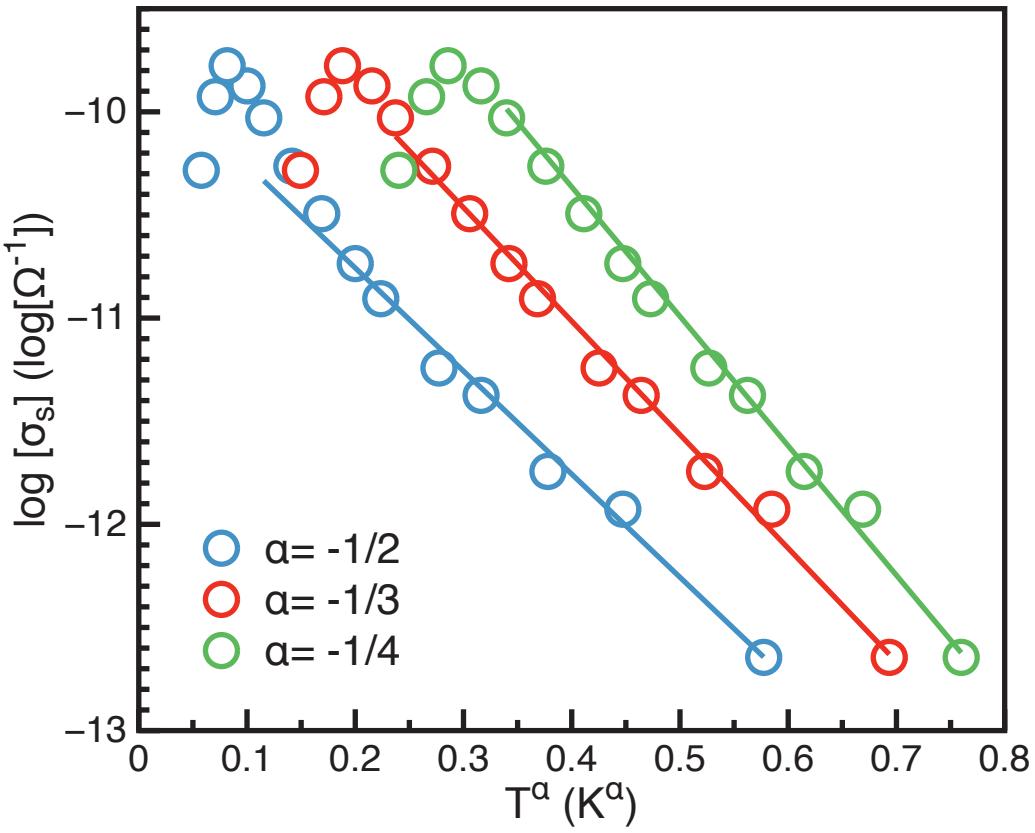

Figure 3.6: Logarithm of conductivity of the 20 uc $LaAlO_3$ thick high-pressure sample as a function of three powers of temperature.

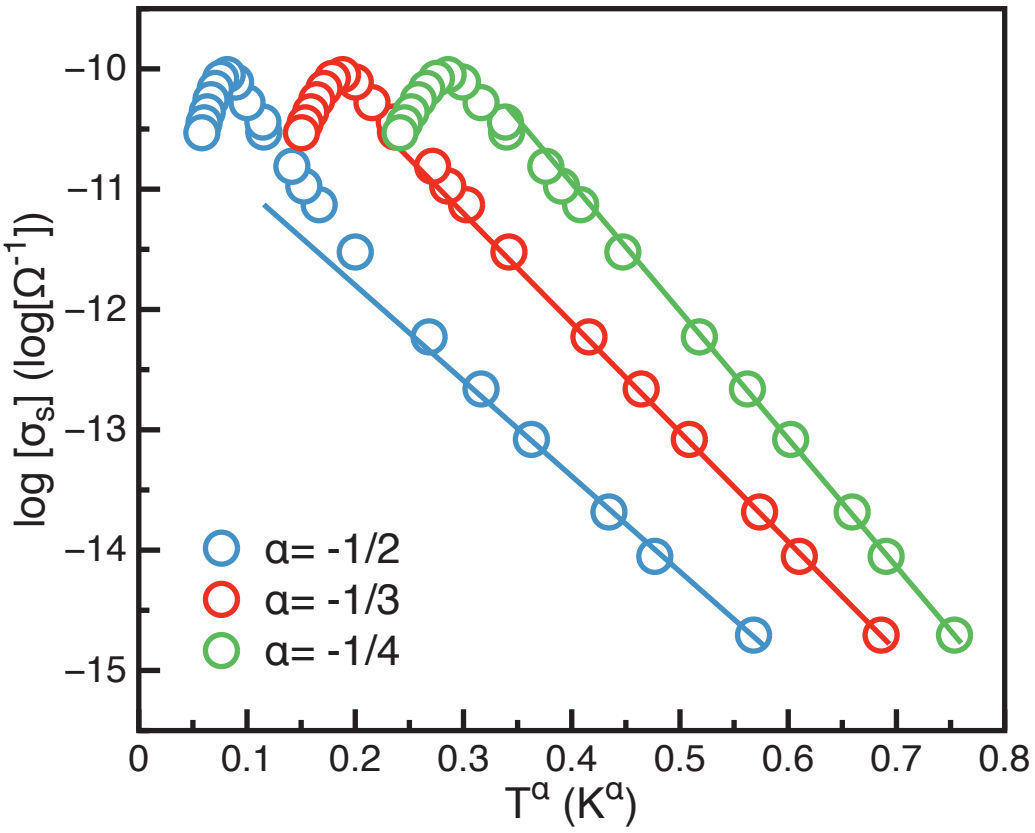

Figure 3.7: Logarithm of conductivity of the 15 uc $LaAlO_3$ thick high-pressure sample as a function of three powers of temperature.

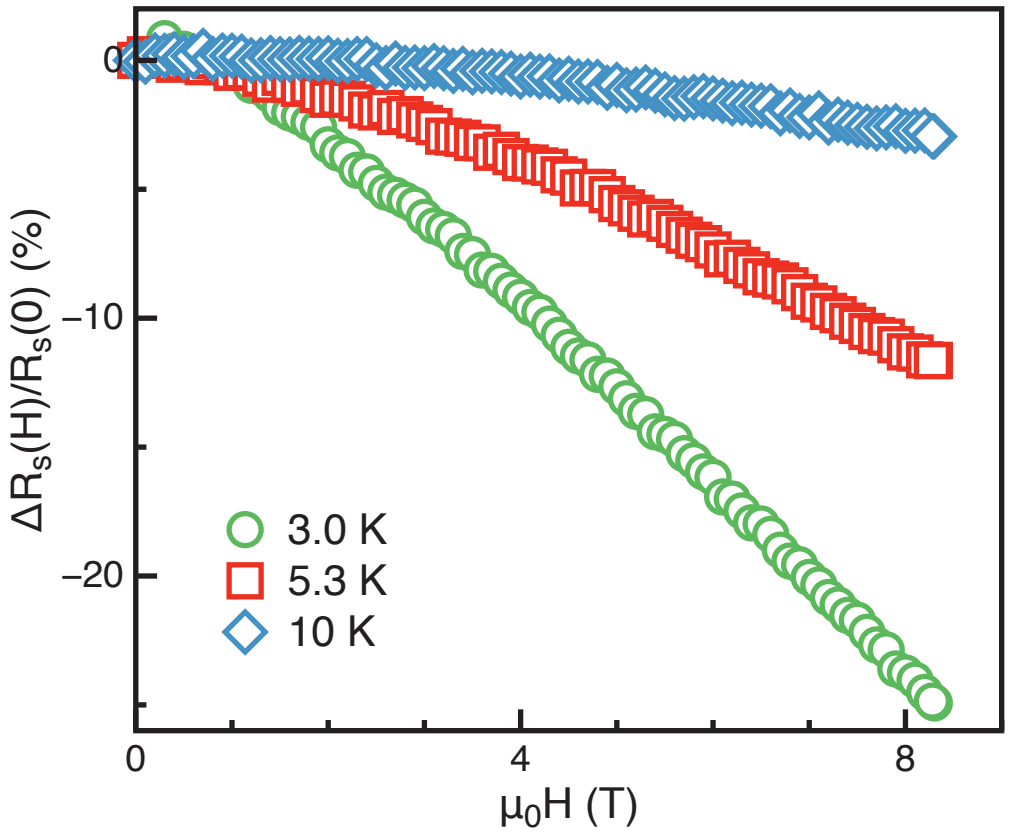

Figure 3.8: Perpendicular field magnetoresistance for the high-pressure sample with $LaAlO_3$ thickness of 15 uc at $T = 3.0$, 5.3 and 10.0 K.

Both Mott-type VRH models (only the $d = 2$ fit is shown in Fig. 3.5)) were good fits to the data, but Efros-Shklovskii VRH was not. Both thicknesses of $LaAlO_3$ grown at this p_{O_2} show similar behavior. This suggests that the increasing sheet resistance arises from a decreased available energy for hopping at lower temperature, which requires hopping to spatially farther sites. However, we are not able to determine the dimensionality of the system in this way.

The high-pressure samples displayed a large negative MR below 15 K that did not saturate with increasing magnetic field. It magnitude of the MR became larger with decreasing temperature and becoming more than -25% at $T = 3$ K and $\mu_0 H$ =8.3 T

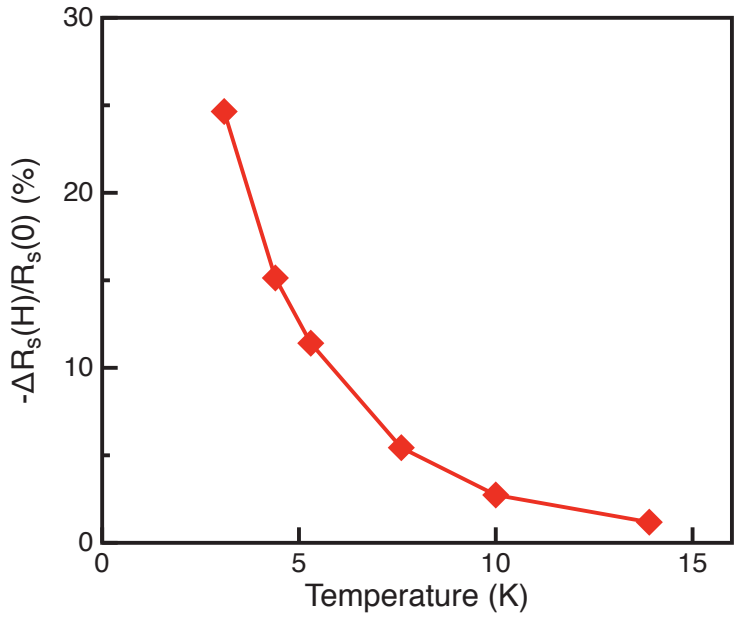

Figure 3.9: Temperature dependence of the perpendicular field magnetoresistance for the high-pressure sample with $LaAlO_3$ thickness of 15 uc at a field $\mu_0 H = 8.3$ T.

without observed saturation either. (Fig. 3.8). The MR did not follow Kohler scaling [75] which indicates that the classical orbital MR observed for out-of-plane field in high mobility 2DEGs at $LaAlO_3$-single crystal $SrTiO_3$ interfaces [76, 77] is not dominant in our system. The negative MR is consistent with the interference between different hopping paths connecting two variable-range hopping sites [78]. This is further supported by the divergent temperature dependence of MR (Fig. 3.9). In summary, the large negative out-of-plane MR, lack of Kohler scaling, high zero-field R_s at low temperature and its VRH dependence all indicate strong localization [78] of interfacial carriers in the high-pressure grown sample.

3.3 Weak Localization in the Low-pressure Samples

The samples grown at $p_{O_2} = 10^{-4}$ and 10^{-6} mbar (low-pressure), both with 20 uc $LaAlO_3$ thicknesses, showed transport properties qualitatively different from the high-pressure samples. We observed metallic behavior down to $T = 75$ and 50 K respectively (Fig. 3.5), and a small up turn in R_2 down to $T = 3$ K. Furthermore, the low-pressure samples displayed small positive MR with a maxima near $\mu_0 H = 7$ T (Fig. 3.10). This MR does not follow Kohler scaling (shown in Fig. 3.11 for the 10^{-6} mbar sample, the behavior of the 10^{-4} mbar sample is similar). The downturn in MR near $\mu_0 H = 7$ T is consistent with weak localization [78] and it agrees with the Maekawa-Fukuyama formalism [79] as characterized previously in $LaAlO_3/SrTiO_3$ [56]. The MR at $\mu_0 H = 8.3$ T diverged with decreasing temperature (Fig. 3.12), as suggested by Maekawa and Fukuyama [79].

Maekawa and Fukuyama extended the model of the MR behavior in the weakly localized regime in order to include the effects of spin-orbit scattering and Zeeman splitting [79]. Following this model we are able to qualitatively reproduce this behavior; the change in conductivity in a magnetic field perpendicular to the 2DEG form is:

$$\frac{\Delta\sigma}{\sigma_0} = \Psi\left(\frac{H}{H_i + H_{so}}\right) + \frac{1}{2\sqrt{1-\gamma^2}}\Psi\left(\frac{H}{H_i + H_{so}(1+\sqrt{1-\gamma^2})}\right) - \frac{1}{2\sqrt{1-\gamma^2}}\Psi\left(\frac{H}{H_i + H_{so}(1-\sqrt{1-\gamma^2})}\right)$$

where $\sigma_0 = e^2/\pi h$ is the conductance quantum, $\Psi(x) = \ln(x) + \psi\left(\frac{1}{2} + \frac{1}{x}\right)$, ψ is the digamma function, $H_{so} = \hbar/4eD\tau_{so}$, $H_i = \hbar/4eD\tau_i$, $\gamma = g\mu_B H/4eDH_{so}$, D is the diffusion constant, τ_{so} and τ_i are the spin-orbit and inelastic relaxation times respectively, and g is the electron's g-factor.

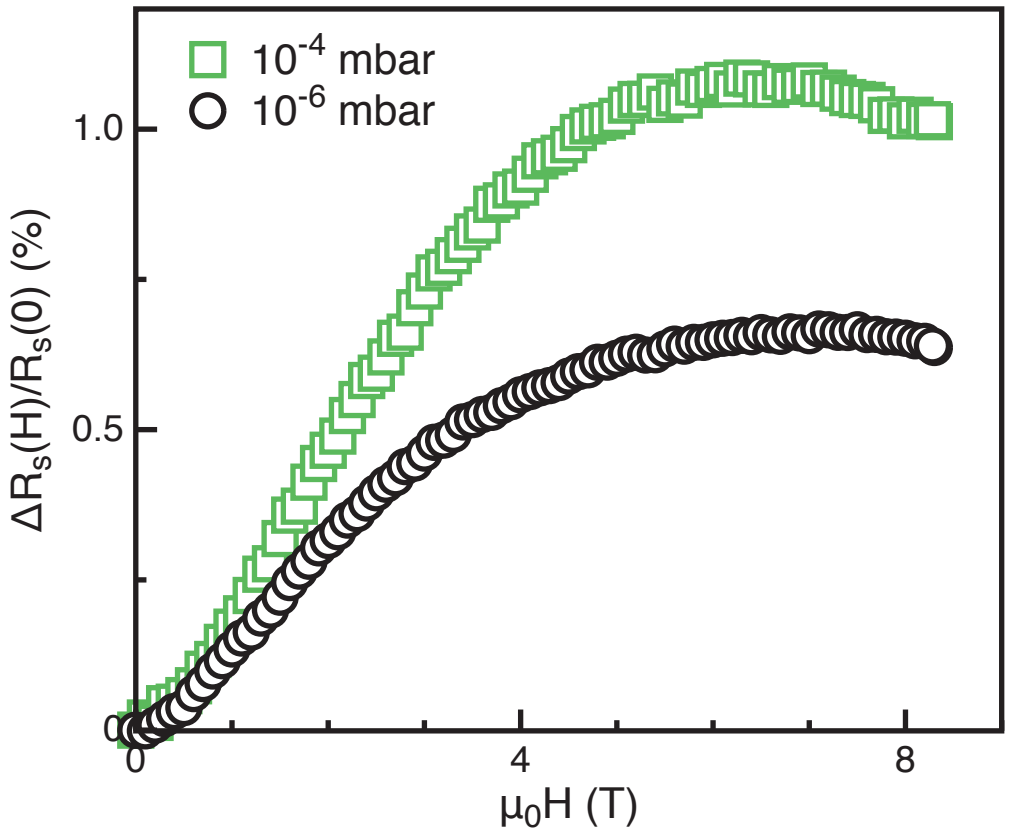

Figure 3.10: Perpendicular field MR for the low-pressure samples at $T = 3$ K.

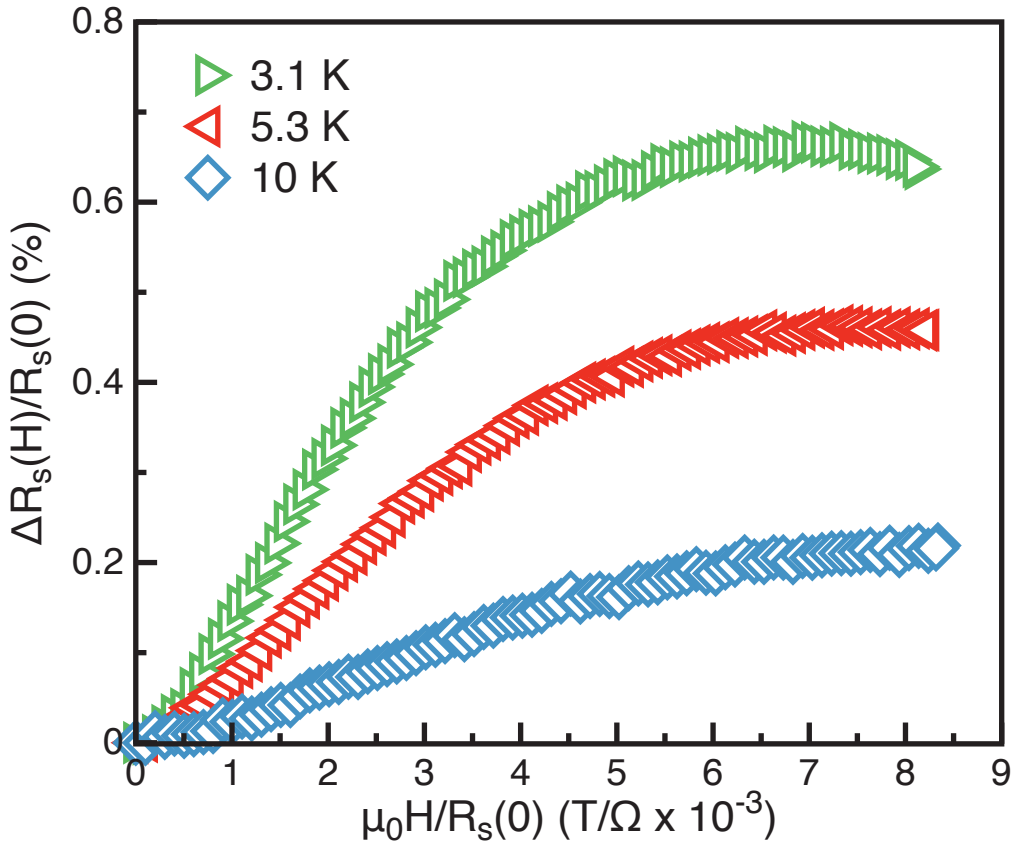

Figure 3.11: Kohler plot of the 10^{-6} mbar grown sample.

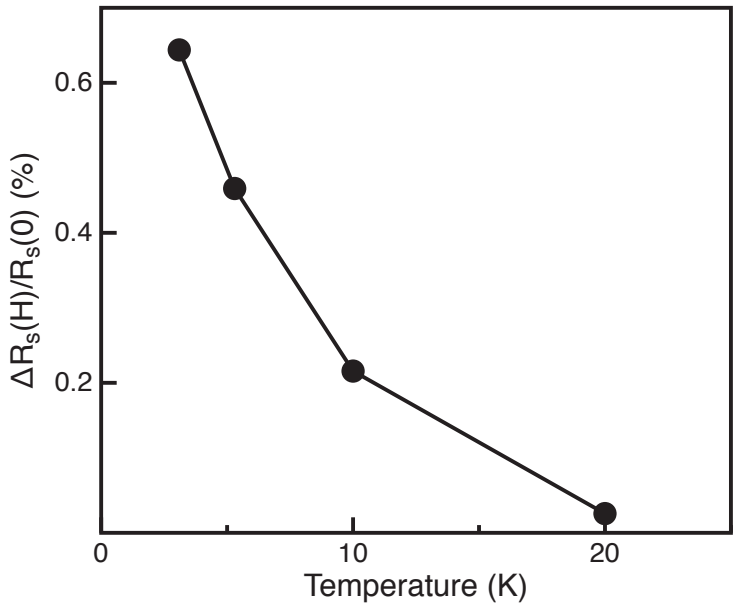

Figure 3.12: Temperature dependence of the perpendicular field magnetoresistance for the 10^{-6} mbar grown sample at a field $\mu_0 H = 8.3$ T.

The fits are shown in Figures 3.13 and 3.14 for the 10^{-6} and 10^{-4} mbar grown samples respectively. The fitted field parameters for the 10^{-6} mbar grown sample were $\mu_0 H_i = 0.27$ T and $\mu_0 H_{so} = 2.95$ T and for the 10^{-4} mbar grown sample $\mu_0 H_i = 0.36$ T and $\mu_0 H_{so} = 2.90$ T, suggesting a stronger influence of the spin-orbit contribution to weak localization. This results are in agreement with weak localization observed in $LaAlO_3$ on single crystal $SrTiO_3$ in Ref. [56].

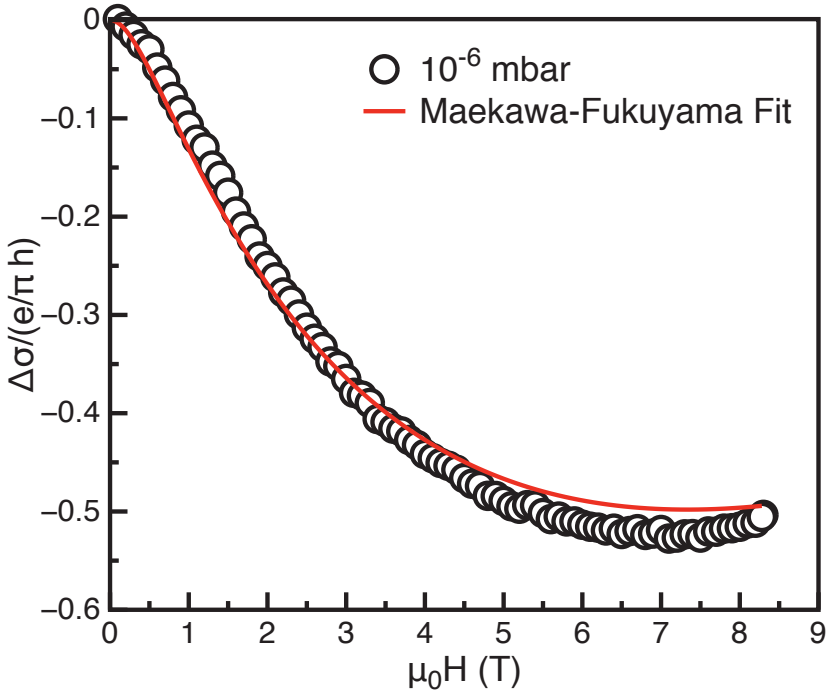

Figure 3.13: Magnetoconductance of the 10^{-6} mbar grown sample at $T = 3$ K.

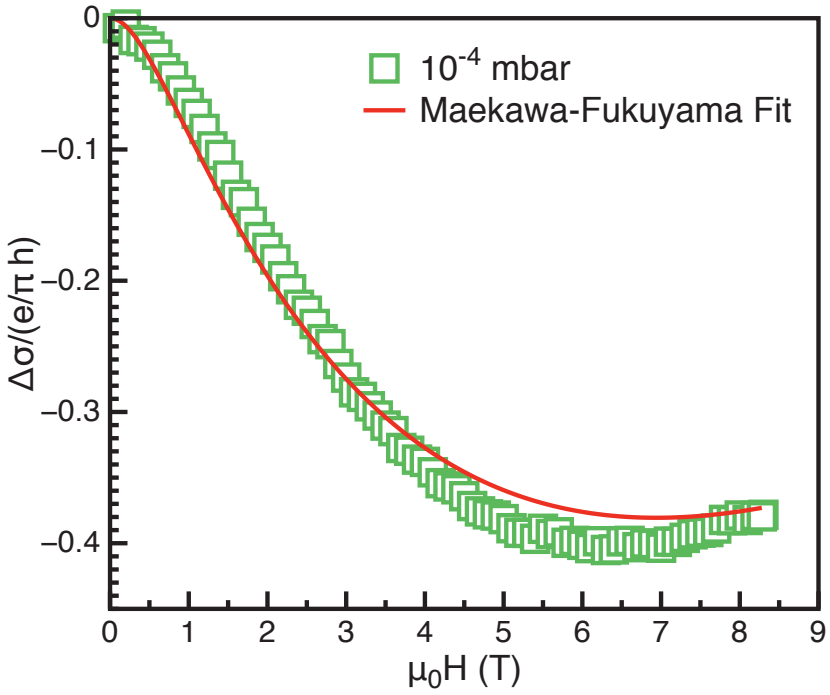

Figure 3.14: Magnetoconductance of the 10^{-4} mbar grown sample at $T = 3$ K.

3.4 Analysis of Transport Properties

We attribute the different carrier concentrations and transport behavior of samples grown at oxygen growth pressures to a different contribution of oxygen vacancies. The low-pressure samples showed room temperature $n_s = 2$–5×10^{14} cm^{-2} (Fig. 3.15), higher than the polarization catastrophe prediction of half electron per unit cell or 3.3×10^{14} cm^{-2}; this is a clear indication of contribution of carrier from oxygen vacancies. The high-pressure samples showed a room-temperature $n_s = 6.2 \times 10^{13}$ cm^{-2}, lower than both the polarization catastrophe prediction and the calculated critical density at which carriers begin to occupy d_{xz} and d_{yz} subbands [51]. As a check, we found that 100nm thick, oxygen deficient $SrTiO_3$ thin films (grown in similar conditions as in the low-pressure samples) on LSAT substrates without an $LaAlO_3$ overlayer were insulating, as also reported in the literature [80], indicating that the $LaAlO_3/SrTiO_3$ interface is necessary in order to show conductivity in oxygen deficient $SrTiO_3$ on LSAT.

The low-pressure samples displayed mobilities of order 1 cm^2/ Vs at room temperature and order 10 cm^2/Vs at $T = 3$ K (Fig. 3.16). The Hall voltages were found to be linear with magnetic field in the entire temperature range, suggesting single band transport. Thus, the mobility is determined in terms of the carrier relaxation time by

$$\mu_H = \frac{e\tau}{m^*} \tag{3.6}$$

where τ is the relaxation time and m^* is the carrier's effective mass. We can fit the scattering time in a single band model to

$$\frac{1}{\tau} = \frac{1}{\tau_1} + \frac{1}{\tau_2} \tag{3.7}$$

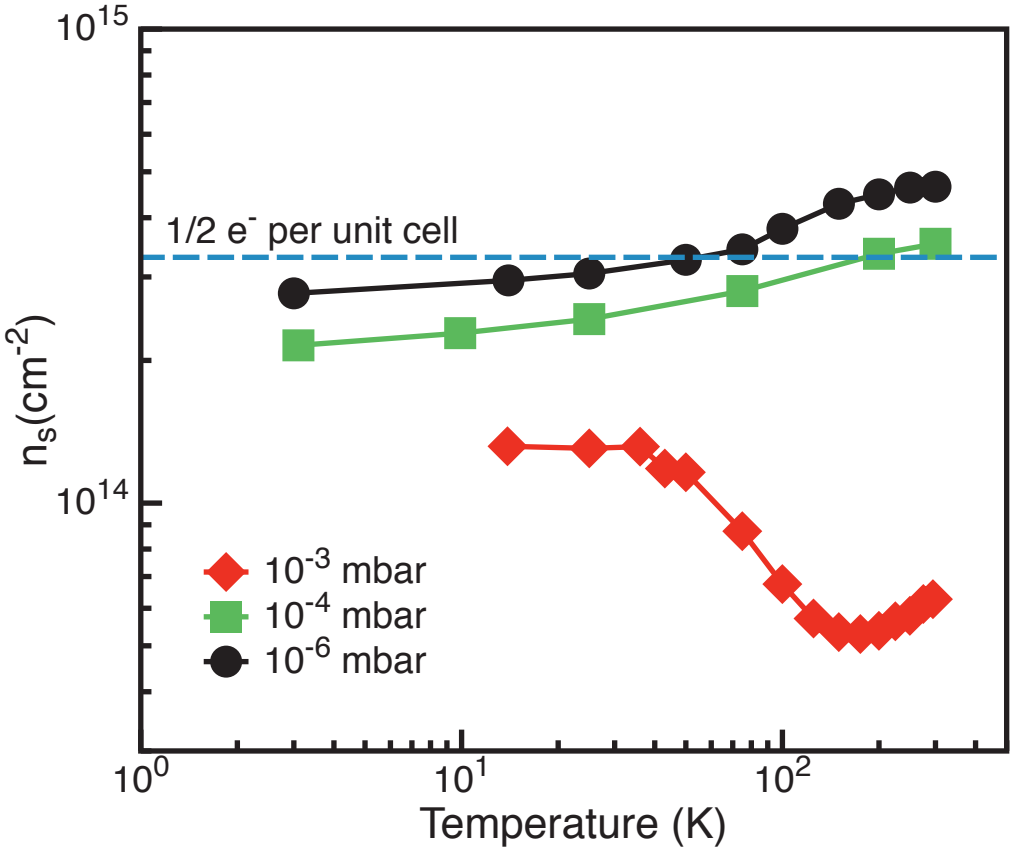

Figure 3.15: Temperature dependence of n_s in $LaAlO_3/SrTiO_3$ films on LSAT substrates.

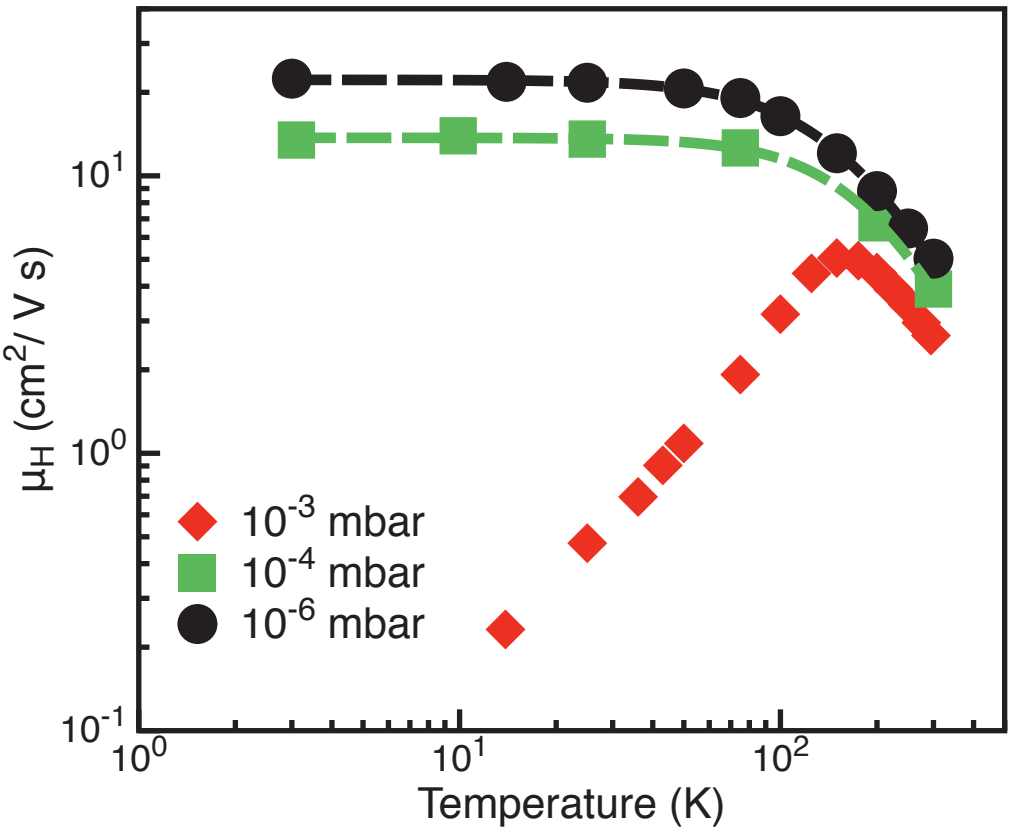

Figure 3.16: Temperature dependence of μ_H in $LaAlO_3/SrTiO_3$ films on LSAT substrates.

where τ_1 is a temperature-independent impurity scattering time, and τ_2 is temperature-dependent $\tau_2(T) \sim \left(T/\bar{T}\right)^{\alpha}$, modeling contributions from lattice interactions.

We find $\alpha \sim 2.1$ and 2.4 for the 10^{-6} and 10^{-4} mbar samples, respectively, and in general agreement with typical exponents $\alpha \sim 2.0$–2.7 reported for $LaAlO_3$ on single crystal $SrTiO_3$ heterostructures [14, 24, 76]. Weak-localization effects are destroyed by inelastic scattering in this temperature regime [81]. At low temperatures, the mobilities saturate at values two orders of magnitude smaller than the highest observed at the $LaAlO_3$/single crystal $SrTiO_3$ interface [3, 25, 26, 53]; but are consistent with recently reported results obtained in a $LaAlO_3/SrTiO_3$ on LSAT heterostructure [68].

3.5 Discussion

We argue that two factors dominantly contribute to the low-temperature mobility of carriers at the $LaAlO_3/SrTiO_3$ interface: a change in spatial extent of carriers at the interface and disorder at the interface. Varying mobilities in field effect experiments have been discussed in terms of a changing spatial confinement of the electrons with applied electric field, with carriers closer to the interface becoming more susceptible to scattering and localization by interfacial disorder [55, 58]. $LaAlO_3$ grown at lower pressures leads to the occupation of bands further into the $SrTiO_3$ layer, which are less susceptible to interfacial localization.

In the high-pressure samples, the threshold for occupation of d_{xz} and d_{yz} bands has not yet been reached. The carriers in the lower energy d_{xy} bands in at most the first three TiO_2 layers close to the interface [51] become highly localized due to their xy two-dimensional character. In the low-pressure samples the 10^{14} cm^{-2} is exceeded and d_{xz} and d_{yz} become occupied, as well as d_{xy} bands deeper into the $SrTiO_3$ layer [51]. As the d_{xy} carrier close to the interface become strongly localized at low temperatures, as indicated by the behavior of the high-pressure samples, the heavier effective mass d_{xz} and d_{yz} carriers will likely be localized too. Thus, the deep d_{xy} carriers will dominate electrical transport measurements at low temperatures, and since they are farther from the interface, only display weak localization. The possibility of two types of carriers is further discarded in the low-pressure samples since the Hall voltages were found to be linear with magnetic fields up to $\mu_0 H = 8.3$ T.

Disorder at the interface appears to be greater in $LaAlO_3/SrTiO_3$ on LSAT substrates than in the higher-mobility $LaAlO_3$ on single crystal $SrTiO_3$ heterostructures. A possible cause for the increased disorder is the propagation of initial disorder after deposition of the $SrTiO_3$ layer on the LSAT substrate. Disorder from point defects, surface roughness

or incomplete coverage at the $SrTiO_3$/LSAT interface could be further propagated to the next interface after the deposition of the $LaAlO_3$ layer. It is the increased disorder in these heterostructures that shows the dramatic difference in transport properties at different carrier concentrations.

Strain in the $SrTiO_3$ layer may also affect the interfacial mobility. Compressively strained $SrTiO_3$ has been reported to undergo transitions to more complex structural phases than the tetragonal phase observed below $T \sim 110$ K in unstrained $SrTiO_3$ [71, 72]. In addition, a symmetry lowering transition has been reported at 150 K in LSAT, with neutron diffraction strongly suggesting a tetragonal distortion [82]. These may lead to a more complex $LaAlO_3/SrTiO_3$ interface structure than that of unstrained $SrTiO_3$ heterostructures, and possibly to higher levels of disorder, in addition to the disorder discussed previously. It has also been reported that compressive strain in fully coherent $LaAlO_3/SrTiO_3$ heterostructures on LSAT produces an internal polarization that points away from the $LaAlO_3/SrTiO_3$ interface, reducing the carrier concentration by the field-effect [64].

3.6 Concluding Remarks

We have shown that the 2DEG at the $LaAlO_3$/thin-film-$SrTiO_3$ interface on LSAT substrates grown at high p_{O_2} shows strongly localized transport at low temperatures, supported by both the temperature dependence of R_s and the MR. The low-pressure grown samples displayed greater sheet carrier densities and weakly localized behavior at low temperatures. We have argued that the additional carriers in the low-pressure samples begin to occupy subbands in Ti layers further from the $LaAlO_3/SrTiO_3$ interface that are less susceptible to interfacial disorder.

Additional work is necessary to fully understand the source of higher disorder and lower mobility at the $LaAlO_3/SrTiO_3$ heterointerface on LSAT, but our measurements suggest contributions from both intrinsic factors due to strain, and extrinsic factors due to defect-induced disorder. The relative importance of these has not been determined, but advances in interface control during growth may lead to substantially improve the mobility. We also expect that the induced polarization in the complex phases of strained $SrTiO_3$ affects transport and carrier confinement at the interface.

Chapter 4

Two-dimensional Electron Gas on Sputtered $LaAlO_3$ on $SrTiO_3$

Oxide heterostructures have vast potential to revolutionize electronic devices due to their high degree of tunability and functionality [83]. The discovery of a two-dimensional electron gas (2DEG) at the $LaAlO_3/SrTiO_3$ interface [3] brought innovative applications in the area of nanoscale oxide devices [13, 84], providing a system with rich exploitable phenomena such as a few-nanometer spatial depth 2DEG [43–45], superconductivity [85], field-effect controlled conductivity [13, 54], among others.

Currently pulsed laser deposition (PLD) [3, 86] is the dominant fabrication technique used for creating oxide interfacial heterostructures of $LaAlO_3$ on $SrTiO_3$ substrates, and only more recently has molecular beam epitaxy [87, 88] been used to create a 2DEG at this interface. In this chapter we explore a different deposition technique of oxide thin films that are uniform over large wafers. 90° off-axis sputtering is a scalable process that has been shown to create smooth, epitaxial films uniformly over large areas [89, 90], essential for potential integration with the current silicon-based semiconductor industry [63]. While several groups have grown $LaAlO_3/SrTiO_3$ heterostructures using sputter deposition [65, 66], none have reported a conducting interfacial 2DEG. This task requires finely tuned growth parameters that avoid reducing the bulk $SrTiO_3$ substrate, which could create unintentional conduction due to oxygen vacancies, while maintaining a

2DEG at the interface with the $LaAlO_3$ layer.

We present the creation of a conductive 2DEG by deposition of a high quality $LaAlO_3$ thin film on a $SrTiO_3$ substrate using 90° off-axis sputtering. The transport properties and nanowriting capabilities are shown to be similar to those found in $LaAlO_3/SrTiO_3$ grown by PLD. The growth and structural characterization efforts were led by J. P. Podkaminer in C.B. Eom's group; the author (T.H.) performed magnetotransport characterization and M. Huang in J. Levy's group at the University of Pittsburgh demonstrated the nano-writing capabilities. This chapter follows closely our published results in Ref. [67].

4.1 Growth Procedure: 90° off-axis Sputtering

In order to create an oxide interfacial 2DEG, we use a different regime of growth conditions that deviates from the previously reported 3:4 O_2:Ar ratio [65, 91] and high pressure ($\sim$1 mbar) O_2 sputter environments [66]. We aim at reproducing the growth conditions widely used in PLD to create conducting $LaAlO_3/SrTiO_3$ interfaces. However, duplicating the 10^{-4}–10^{-6} Torr [28, 30, 86] O_2 partial pressures used in PLD can be challenging in sputtering due to typically higher Ar gas pressure (i.e. 200 mTorr) used for 90° off-axis sputtering. This three to five order of magnitude difference in partial pressures can not be controlled accurately in this regime. We overcome this difficulty by sputtering in a pure Ar atmosphere and relying on the sputtered single crystal $LaAlO_3$ target to sustain a large enough background pressure of O_2 and atomic oxygen to create an environment similar to PLD. During sputtering of an oxide target material a relatively large amount of O_2 and, more importantly, atomic oxygen is produced. The high activity of atomic oxygen compared with molecular oxygen [92] significantly increases

the effective p_{O_2} during sputter growth, creating an environment capable of producing high quality 2DEGs [3, 86] during sputtering while mantaining a pure Ar atmosphere.

The growth system consists of a 2 inch RF magnetron sputter source in a 90° off-axis geometry with reference to the sample heater. All films discussed here were grown on TiO_2-terminated (001) $SrTiO_3$ substrates [93]. A $LaAlO_3/SrTiO_3$ control sample was grown by PLD using conditions outlined in Park et al. [63]. The sputtered samples were grown from a 2-inch single crystal $LaAlO_3$ target mounted on a US Gun II sputter source at an RF power of 50W. The sample temperature was 780°C during growth, consistent with previously reported works [86]. A partial pressure 200 mTorr of Ar was used, with a minimum pre-sputter time of 15 minutes in order to stabilize a background partial pressure of O_2 (and atomic oxygen) produced from the target. Films grown without this extended pre-sputtering were found to be insulating. We also grew samples in the previously reported 3:4 of O_2:Ar atmosphere [65], producing insulating films as well. We subsequently annealed the sample for 1 hour in 300 Torr O_2 at 600°C to ensure that the bulk substrate was fully oxidized [94].

Accurate control of the thickness of the $LaAlO_3$ layer is necessary since the electronic reconstruction in the polarization catastrophe scenario has an abrupt transition from an insulating to a conducting state at 4 unit cells [12, 13]. While molecular beam epitaxy and PLD take advantage of *in-situ* RHEED monitoring to control layer-by-layer growth [95], sputtering has no comparable *in-situ* monitoring. Instead we used x-ray reflectivity for thickness calibration. At the deposition conditions used, we are able to determine the growth rate of $LaAlO_3$ to be 1.65 Å/min by fitting x-ray reflectivity data [96] as shown in Fig. 4.1. With this rate, we used deposition time as a control parameter to grow samples with $LaAlO_3$ film thicknesses corresponding to 2–6, 10, 15 and 16 unit cells.

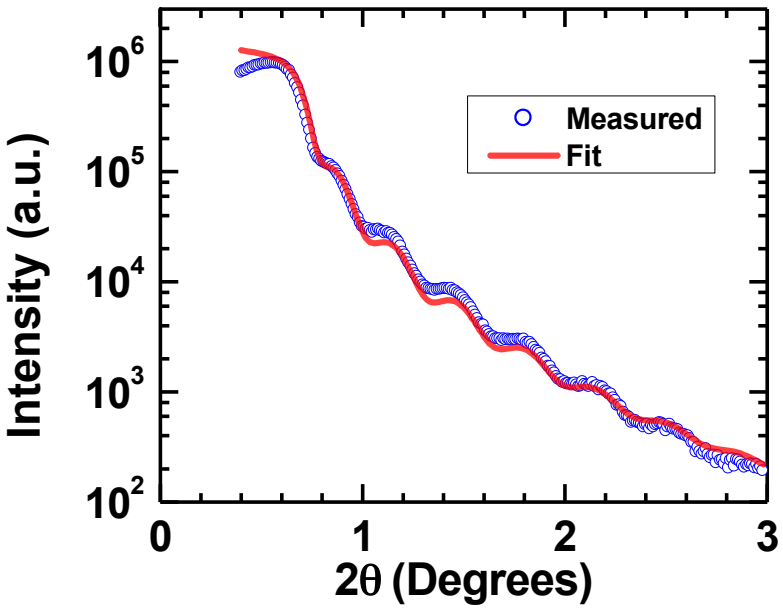

Figure 4.1: X-ray reflectivity measurement of the $LaAlO_3/SrTiO_3$ heterostructure displaying clear thickness plateaus closely matching the model. Reprinted with permission. Accepted for publication in Applied Physics Letters. Copyright AIP Publishing LLC.

4.2 Structural Analysis

High-resolution x-ray diffraction performed on a 40 nm thick $LaAlO_3$ on $SrTiO_3$ sample (Figs. 4.2 and 4.3) show an out-of-plane lattice parameter of 3.74 Å (Fig. 4.2) and in-plane lattice parameter of 3.89 Å, close to the in-plane lattice constant of bulk $SrTiO_3$ of 3.905 Å. The $LaAlO_3$ film thus displays 2.3% tensile strain when compared to the bulk $LaAlO_3$ lattice constant of 3.790 Å. This indicates that even at 40 nm the film is almost fully strained. The phi scan in Fig. 4.3 shows 4-fold symmetry of the $LaAlO_3$ film with an in-plane (101) FWHM of 0.26° indicating a very small in-plane misalignment of the film while the in-plane FWHM of the substrate is 0.01°. A reciprocal space mapping (RSM) around the Bragg peak of a $SrTiO_3$ substrate on a 10 unit cell thick $LaAlO_3$ sample (see Fig. 4.4) shows the film is fully coherent and of single phase. The ultra-thin character of the $LaAlO_3$ layer causes the elongation of the film peak. The out-of-plane lattice constant obtained from the peak position of the film is 3.72 Å, which is in good agreement with that measured from the θ–2θ scan on the thicker (40 nm) film. AFM imaging (Fig. 4.5) shows the sputtered $LaAlO_3$ film is atomically flat with an average roughness of $\sim$0.14 nm. The clear step and terrace structures observed arise from those of the underlying $SrTiO_3$ substrate.

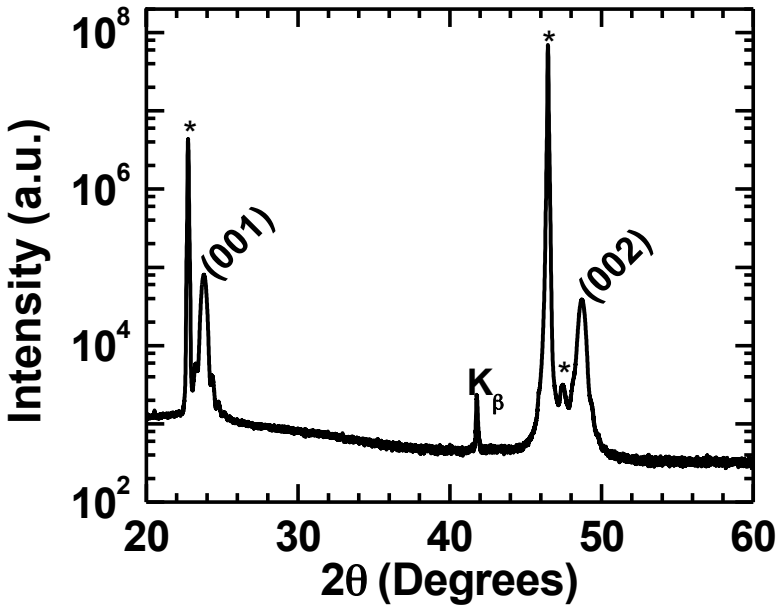

Figure 4.2: Wide range 2θ–ω scan showing single crystal $LaAlO_3$ grown a $SrTiO_3$ substrate. Reprinted with permission. Accepted for publication in Applied Physics Letters. Copyright AIP Publishing LLC.

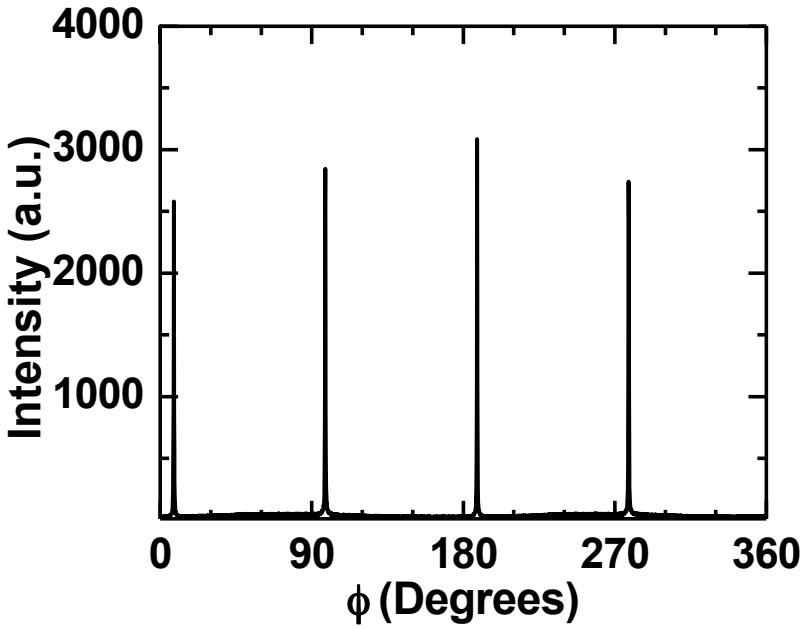

Figure 4.3: In-plane (101) ϕ scan showing 4-fold symmetry. Reprinted with permission. Accepted for publication in Applied Physics Letters. Copyright AIP Publishing LLC.

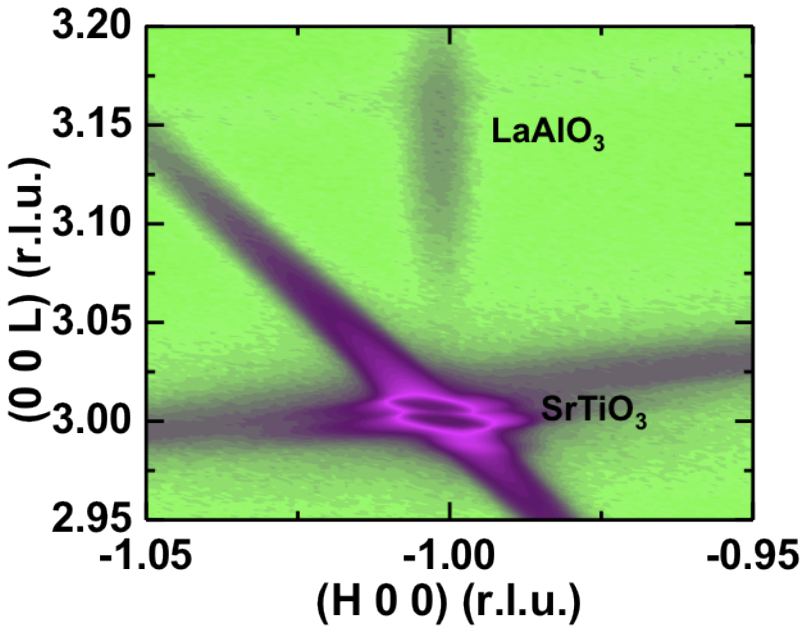

Figure 4.4: Reciprocal Space Map of a 10 unit cell sample showing the $LaAlO_3$ film to be fully coherent. Reprinted with permission. Accepted for publication in Applied Physics Letters. Copyright AIP Publishing LLC.

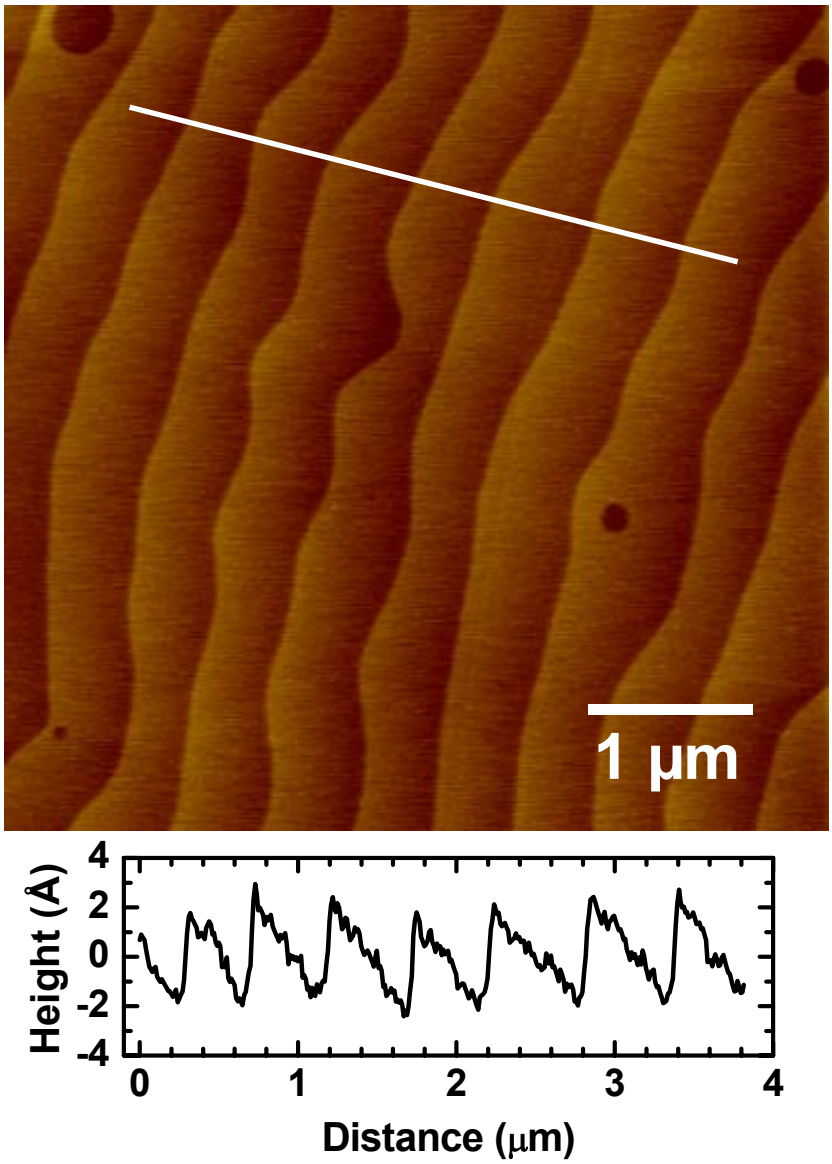

Figure 4.5: Surface topographic image of a 10 unit cell $LaAlO_3$ film showing smooth steps following the $SrTiO_3$ substrate. A plot of height versus distance along the line showing clear unit cell high steps is overlaid on the image. Reprinted with permission. Accepted for publication in Applied Physics Letters. Copyright AIP Publishing LLC.

4.3 Transport Analysis

We show the existence of a critical thickness in sputtered $LaAlO_3/SrTiO_3$ by measuring the carrier concentration (n_s) as a function of film thickness. Samples were wire bonded with Al wires in the four-point van der Pauw geometry [73] and electrical transport was measured using a Keithley 2400 Sourcemeter to source bias currents and measure potential drops, and a Keithley 2700 Data Acquisition unit. Measured Hall coefficients were found to be linear as a function of applied magnetic field. Carrier concentration measurements on samples with different $LaAlO_3$ thicknesses (shown in Fig. 4.6) display a clear transition from an insulating to a conducting state at 4 unit cells, consistent with findings on PLD-grown films [13]. This is a clear indication that these $LaAlO_3/SrTiO_3$ samples produced by sputtering exhibit a 2DEG behavior as explained by electronic reconstruction. We also observe a negligible dependence on thickness above 4 unit cells of sputtered $LaAlO_3$ not typical of PLD grown $LaAlO_3/SrTiO_3$.

Additionally, transport measurements were carried out as a function of temperature on both sputtered and PLD samples with a 10 unit cell $LaAlO_3$ film grown in similar conditions. Temperature dependence measurements were performed in two cryogenic systems. In the temperature range 300–20 K we used a closed-cycle helium gas cryostat model 261265A by APD with compressor model HC-4 by APD mounted on an electromagnet with a maximum field of $\mu_0 H = 0.7$ T at the required pole spacing. Below 20 K we used an Oxford Instruments MagLab 2000 liquid helium, sample in flowing gas cryostat with an integrated superconducting magnet with a maximum field of $\mu_0 H = 8.3$ T.

Even though the carrier density in the sputtered sample at room temperature was about six times smaller than the PLD-grown counterpart (see Table 4.1), it had a weaker dependence on temperature (Fig. 4.7). Both samples reach similar carrier concentrations at $T = 3$ K (see Table 4.2). The dependence of the Hall mobility (μ_H) on temperature

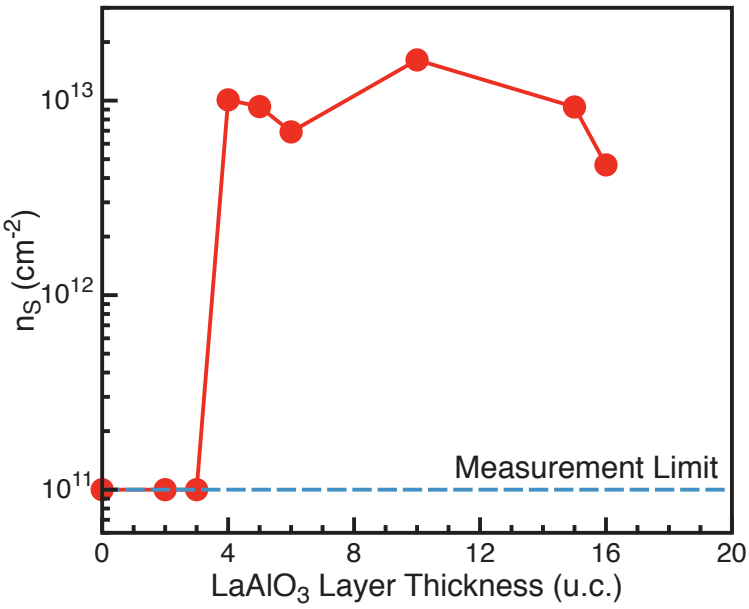

Figure 4.6: Carrier concentration dependence on $LaAlO_3$ thickness in sputtered $LaAlO_3$ on $SrTiO_3$. Reprinted with permission. Accepted for publication in Applied Physics Letters. Copyright AIP Publishing LLC.

is similar for both samples above $T = 75$ K, where they obey a power law behavior of $T^{-\alpha}$, with $\alpha = 2.3$ and 2.4 for the sputtered and PLD grown samples respectively (Fig. 4.8), consistent with reported behaviors of PLD grown $LaAlO_3/SrTiO_3$ [14, 24]. At low temperatures the mobility in the sputtered sample has a maximum at $T = 20$ K of 323 cm^2/Vs followed by a small downturn. This downturn is accompanied by a small upturn in carrier density and upturn in sheet resistance (see Fig. 4.9). On the other hand, the PLD sample displays metallic behavior in the 300–3 K range (see Fig. 4.9).

A similar transport behavior to our 10 unit cell sputtered $LaAlO_3$ is observed in oxygen reduced $SrTiO_{3-\delta}$ thin films grown at $p_{O_2} = 10^{-5}$ Torr (1.33×10^{-5} mbar) [35]. On the other hand, dependence on growth p_{O_2} during PLD of $LaAlO_3$ has been attributed create different regimes of conductivity which in turn produce different R_s behavior with temperature [28, 86]. The most similar R_s behavior to our sputtered $LaAlO_3/SrTiO_3$ is

Table 4.1: Transport Properties of Sputtered and PLD grown 10 unit cell $LaAlO_3$ on $SrTiO_3$ at Room Temperature

Property	Sputtered	PLD
R_s ($\Omega/\square$)	1.08×10^5	1.28×10^4
n_s (cm^{-2})	1.48×10^{13}	8.69×10^{13}
μ_H (cm^2/Vs)	3.92	5.62

Table 4.2: Transport Properties of Sputtered and PLD grown 10 unit cell $LaAlO_3$ on $SrTiO_3$ at $T = 3$ K

Property	Sputtered	PLD
R_s ($\Omega/\square$)	2.16×10^3	9.37×10^1
n_s (cm^{-2})	1.16×10^{13}	1.81×10^{13}
μ_H (cm^2/Vs)	250	3670

seen in samples grown at $p_{O_2} = 1 \times 10^4$ mbar in Ref. [28], where they attribute the R_s upturn to scattering from magnetic impurities. In Chapter 3 and Ref. [29] we observed a small upturn in R_s and positive magnetoresistance in low-pressure (10^{-4}–10^{-6} torr), PLD grown $LaAlO_3$ on thin-film $SrTiO_3$, which we attributed to weak localization caused by interfacial disorder. A further low temperature high-field magnetoresistance study will elucidate whether the upturn in R_s is caused by weak localization due to disorder or magnetic impurity scattering. Regardless, it is clear that oxygen deficiencies are source of these reduced magnetotransport properties. This comes to no surprise since no p_{O_2} is applied during the sputtering process and full oxidation of the $LaAlO_3$ film relies on the unmonitored oxygen released from the stoichiometric targets during the pre-sputter step.

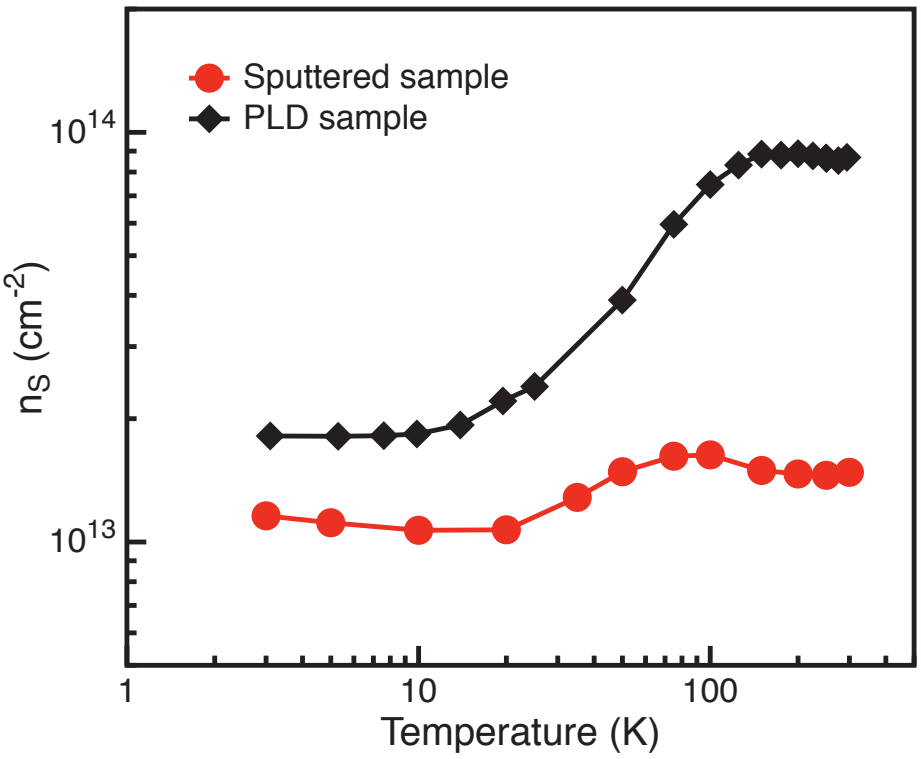

Figure 4.7: Temperature dependence of n_s of sputtered and PLD grown 10 unit cells of $LaAlO_3$ on $SrTiO_3$. Reprinted with permission. Accepted for publication in Applied Physics Letters. Copyright AIP Publishing LLC.

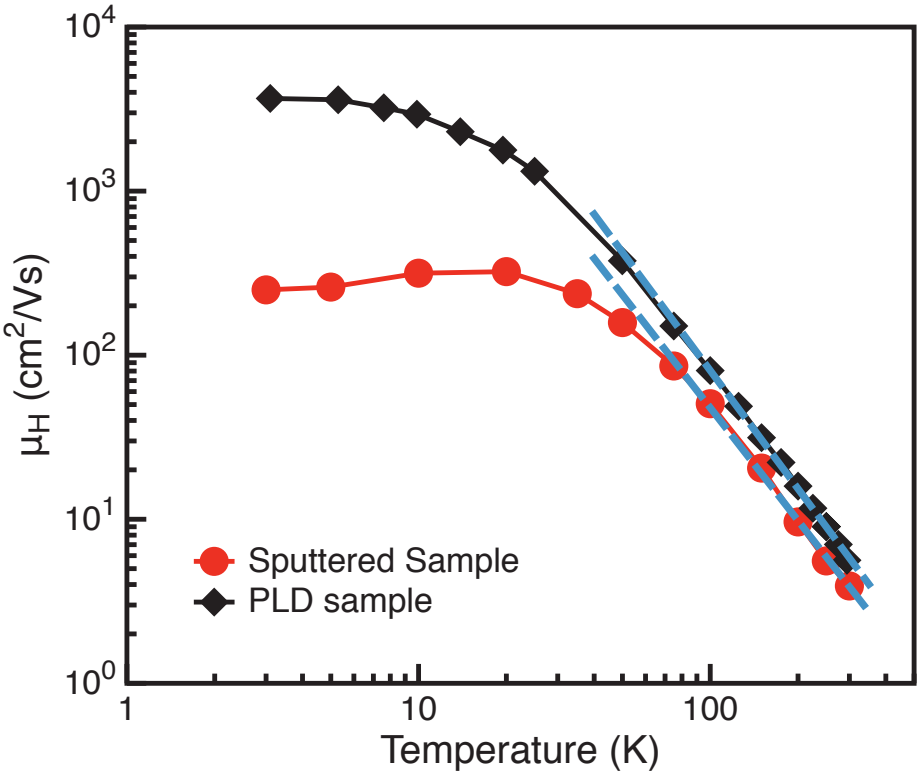

Figure 4.8: Temperature dependence of μ_H of sputtered and PLD grown 10 unit cells of $LaAlO_3$ on $SrTiO_3$. Reprinted with permission. Accepted for publication in Applied Physics Letters. Copyright AIP Publishing LLC.

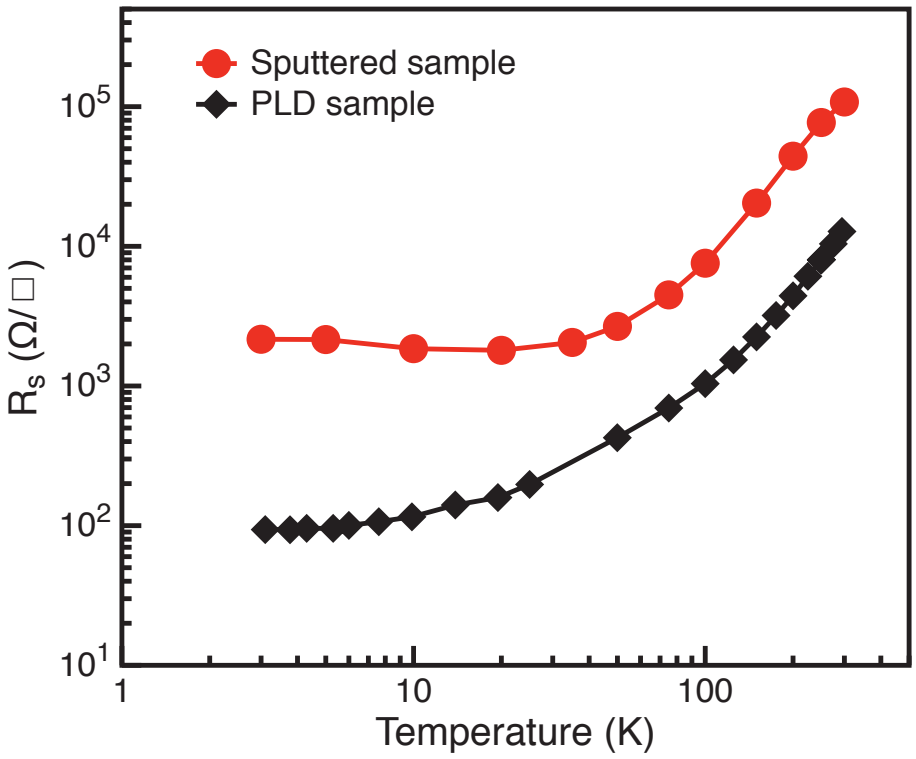

Figure 4.9: Temperature dependence of R_s of sputtered and PLD grown 10 unit cells of $LaAlO_3$ on $SrTiO_3$. Reprinted with permission. Accepted for publication in Applied Physics Letters. Copyright AIP Publishing LLC.

4.4 AFM Nano-writing Capabilities

We also demonstrate room-temperature conductive-AFM (c-AFM) switching of 2DEG nanostructures formed at $LaAlO_3/SrTiO_3$ heterointerfaces grown by 90° off-axis sputtering. The ability to write and erase nanostructures in these samples has been observed at a range of thicknesses between 3 and 3.7 unit cells. The c-AFM tip acts as a local field-effect actuator, applying a voltage at the top of the $LaAlO_3$ layers that creates a persistent conducting state of the $LaAlO_3/SrTiO_3$ 2DEG [62].

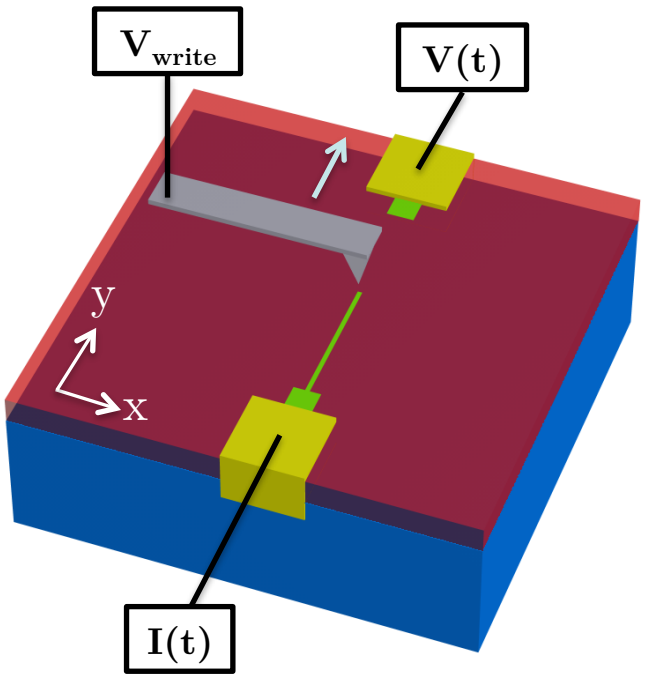

Figure 4.10: Schematic diagram of the conductive-AFM writing process of sputtered $LaAlO_3/SrTiO_3$. AFM tip is +10V biased. Reprinted with permission. Accepted for publication in Applied Physics Letters. Copyright AIP Publishing LLC.

After 90° off-axis sputtering growth, electrically conducting contacts to the interface are defined by optical lithography. Trenches 25 nm deep are created by Ar-ion milling through the $LaAlO_3$ layer, and are then filled by sputtering 4 nm of Ti and 25 nm of Au to form bilayer electrodes. Within the 30 μm × 30 μm canvas defined by the

electrical contacts, nanostructures are written and erased at the interface using c-AFM lithography at room temperature. The conductance between two electrical contacts is continuously monitored by a lock-in amplifier (Figs. 4.10 and 4.11).

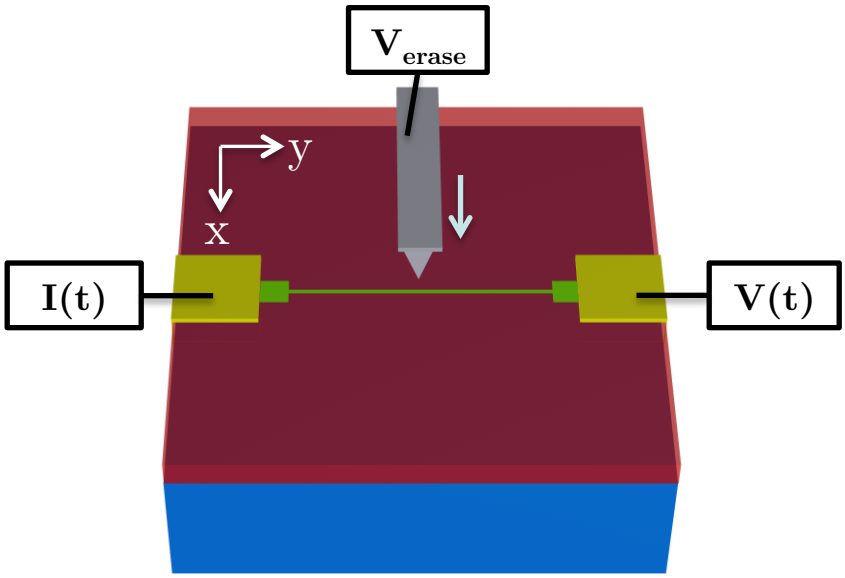

Figure 4.11: Schematic diagram of the conductive-AFM erasing process. AFM tip is -10V biased and moving perpendicularly across the nanowire. Reprinted with permission. Accepted for publication in Applied Physics Letters. Copyright AIP Publishing LLC.

The c-AFM writing process (Fig. 4.10) on a 3.4 unit cell $LaAlO_3/SrTiO_3$ sample begins by 'writing' two rectangular pads by raster scanning a V_{write}= +10 V biased AFM tip to form better contacts to the Au electrodes. Then a conductive nanowire is created by the +10 V biased AFM tip scanning from one electrode to the other at a speed of 300 nm/s (Fig. 4.10) When the tip reaches the other electrode, a pronounced and abrupt conductance jump is observed (Fig. 4.12). The observed maximum conductance change and non-exponential decay in atmosphere conditions are comparable with the 3.4 unit cell $LaAlO_3/SrTiO_3$ samples grown by PLD [62].

After writing the nanowire, the AFM tip is repositioned and biased at V_{erase}= -10 V,

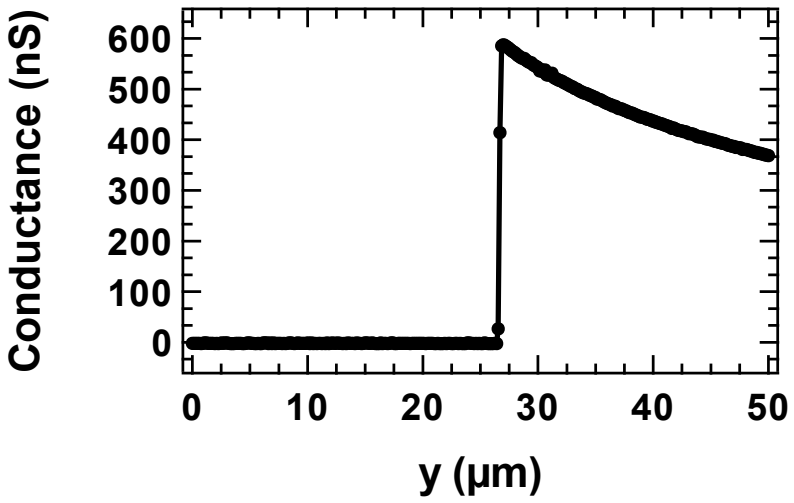

Figure 4.12: Conductance between the two electrodes during the writing process. When the tip reaches the second electrode, conductance increases abruptly. Reprinted with permission. Accepted for publication in Applied Physics Letters. Copyright AIP Publishing LLC.

and then moved perpendicularly across the nanowire at 10 nm/s speed (Fig. 4.11). The conductance decreases abruptly to zero when the tip reaches the nanowire (Fig. 4.13). The nanowire width can be quantified by fitting the conductance drop curve with the function [62]:

$$G(x) = G_0 - G_1 \tanh\left(\frac{x}{h}\right) \tag{4.1}$$

The best fit is shown as the red curve in Fig. 4.13 and we can determine a nanowire width of 9.2 nm. The ability to create conductive nanostructures is important for technological applications, but it also serves as a sensitive probe of the uniformity of the 2DEG. A single insulating patch along the nanowire is sufficient to prevent conductivity.

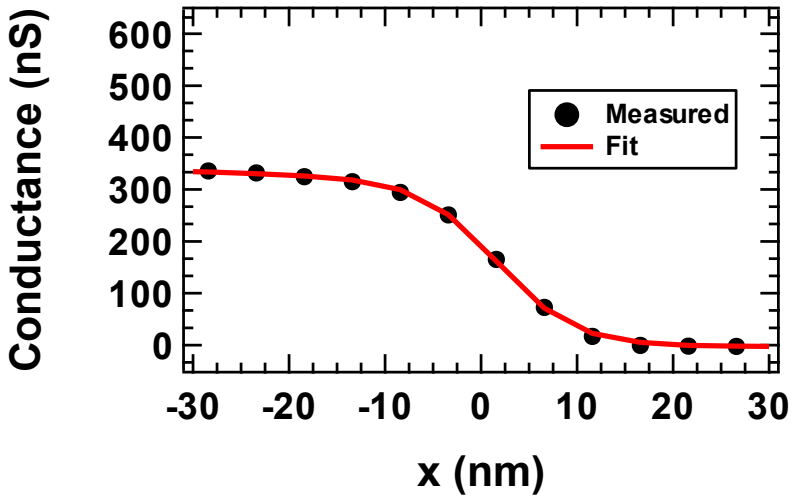

Figure 4.13: Conductance between the two electrodes during the erasing process. As the tip scans across the nanowire, conductance decreases to zero. The red curve shows the best fit indicating a nanowire thickness of 9.2 nm. Reprinted with permission. Accepted for publication in Applied Physics Letters. Copyright AIP Publishing LLC.

4.5 Concluding Remarks

Sputtering is a thin film growth technique capable of the uniform large area deposition required for scaling. In this work we demonstrated that sputtering is a viable technique to grow high quality epitaxial $LaAlO_3$ films with excellent surface quality on TiO_2-terminated $SrTiO_3$ substrates. Growth conditions were chosen to mimic those known to form a 2DEG at the interface by pulsed laser deposition. We showed that these samples have comparable electronic transport properties to heterostructures grown by PLD and demonstrated room-temperature conductive-AFM nano-writing, demonstrating the capability to make devices on these oxide films. In summary, we have created another avenue of exploration for the study of the 2DEG at the $LaAlO_3/SrTiO_3$ interface by developing a growth process using sputter deposition.

Chapter 5

Polar-Polar $LaAlO_3/SrTiO_3$ Heterointerface

The fabrication of interfacial systems in [111]-oriented perovskite oxides provides a challenge in the area of complex oxide thin films. The polar character of perovskites in (111) layers is typically greater than in the conventional [001]-oriented crystals. Larger polarity of the layers and the discontinuity faced at interfaces drives more strongly mechanisms to achieve charge neutral surfaces, for example: chemical phase separation, defect formation, atomic displacements, intermixing, reconstructions or crystallographic faceting, chemical bond (re)hybridization or chemisorption of foreign atoms [97]. Nevertheless, topologically protected electronic states are predicted by theory to exist at (111) perovskite interfaces of different materials, mainly attributed to the honeycomb lattice in this orientation [98–100]. The heterointerface between $LaAlO_3$ and $SrTiO_3$ is perhaps one of the most studied interfacial systems between two perovskite oxides and hasn't been until recently that the creation of a two-dimensional electron gas has been demonstrated in interfaces other than the (001) [101]. Herranz et al. were the first to demonstrate high-mobility electron systems at the interfaces between epitaxially grown $LaAlO_3$ on $SrTiO_3$ (110) and (111) [101].

In this chapter we look deeper at the (111) interface between $LaAlO_3$ and $SrTiO_3$ by incorporating multiple techniques to gain insight about the structural and electronic

effects at play in this exotic interface. We find that the bare surface of a $SrTiO_3$ (111) substrate is initially reconstructed and that upon epitaxial deposition of $LaAlO_3$ the two-dimensional conducting system forms with n-type carriers and that the structures is structurally coherent This project was of a complexity that required the collaboration of multiple groups. The growth of the heterostructures was led by S. Ryu in C.B. Eom's group at the Materials Science and Engineering Department at the University of Wisconsin-Madison. Surface x-ray diffraction and COherent Bragg Rod Analysis (COBRA) was performed by Hua Zhou and D.D. Fong at Argonne National Laboratory. The author (T.H.) and M. S. Rzchowski performed magnetotransport studies. TEM was performed in X.Q. Pan's group at the University of Michigan and DFT calculations were performed by E.Y. Tsymbal's group at the University of Nebraska.

5.1 Geometrical Considerations for the (111) Interface

Let us revisit the conventional unit cell of the perovskite structure ABO_3 shown in Fig. 5.1. It is constituted of a basic cubic cell with the A-sites at the edges of the cube, the O-sites at the center of the face and the B site at the center of the cubic cell. The lattice parameter is a. The cell encloses $\frac{1}{8}$ of an A-type atom per corner, $\frac{1}{2}$ of an O atom per face and the entire B atom at its center; thus, this cell contains one A type and one B type atoms and 3 O-atoms, in agreement with the chemical formula.

The equilateral triangle with edges at the points (1,0,0), (0,1,0) and (0,0,1) (seen as the yellow shaded triangle in Fig. 5.1) lies on the (111) plane of the perovskite lattice. Its side length is $\sqrt{2}a$, it has an area of $(\sqrt{3}/2)a^2$ and the distance between this plane and (0,0,0) along the [111] direction is $a/\sqrt{3}$. This triangle has an A site at each edge

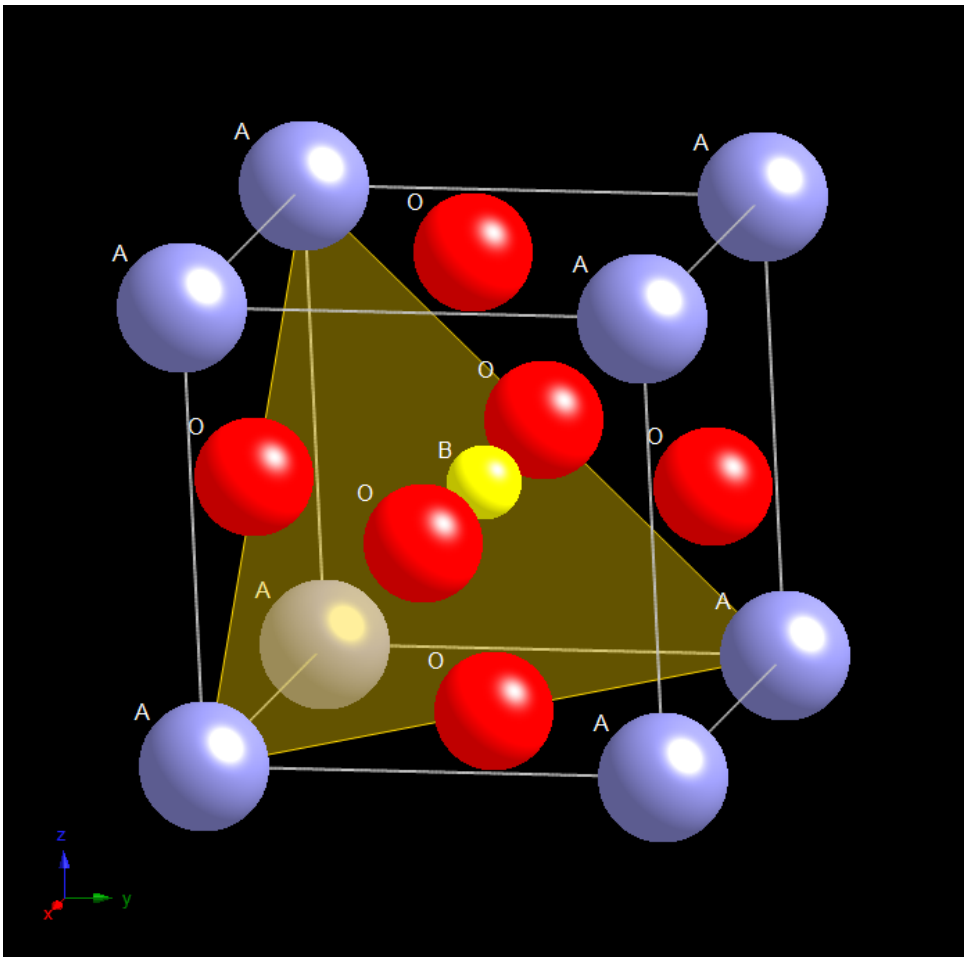

Figure 5.1: Conventional unit cell of an ABO_3 perovskite. Blue, yellow and red circles correspond to the A, B and O atoms respectively. The yellow shaded triangle shows an example of an AO_3 layer.

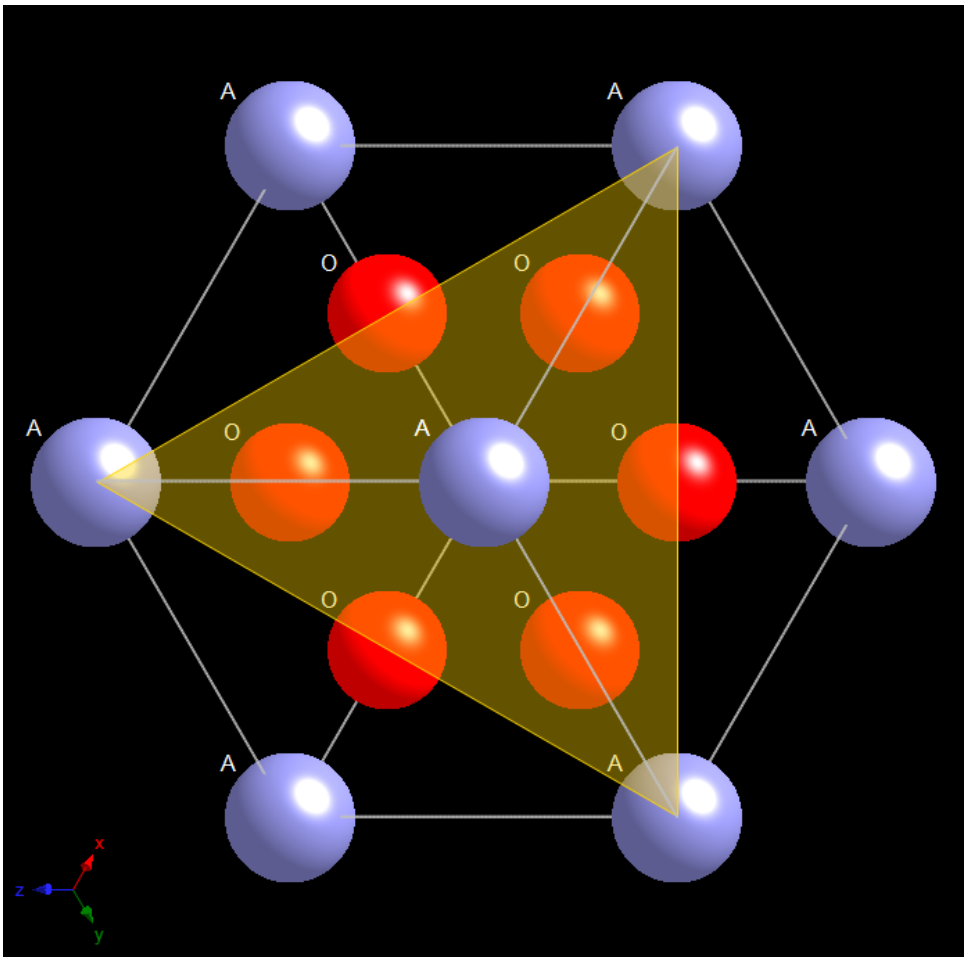

Figure 5.2: Conventional unit cell of an ABO_3 perovskite viewed from the [111] direction. Blue and red circles correspond to the A and O atoms respectively, the B atom is behind the central top A atom. The yellow shaded triangle shows an example of an AO_3 layer.

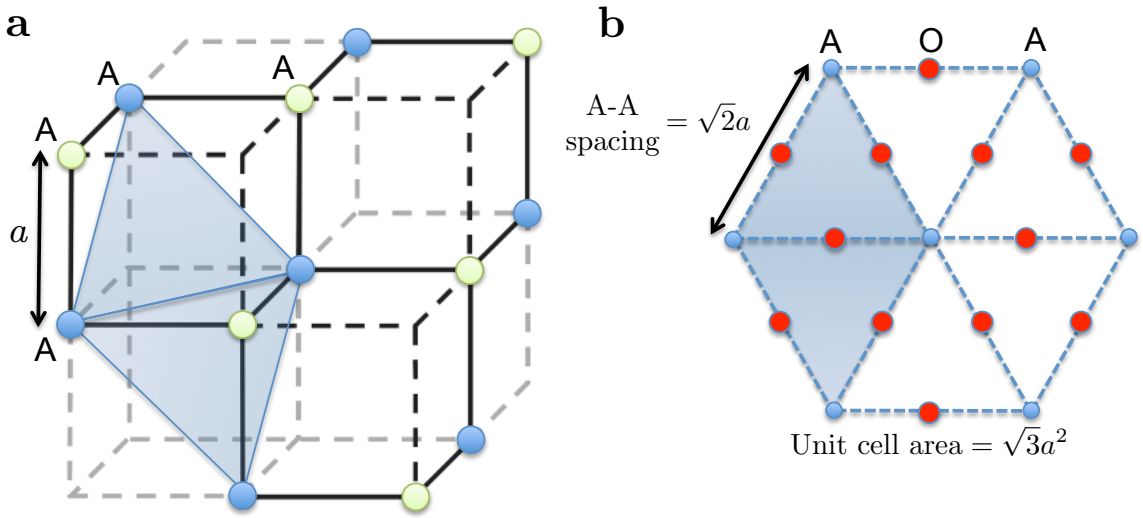

Figure 5.3: (a) Cubic lattice formed by the A-sites in an ABO_3 perovskite. Blue and green circles represent the A-sites in the first and second (111) planes respectively. (b) Hexagonal coordination of the AO_3 (111) plane and definition of a new cell, shown in shaded blue. Blue and red circles correspond to A and O atoms respectively.

and an O site at the midpoint of each of its sides; therefore the triangle cell contains $\frac{1}{6}$ A-type ions per edge and $\frac{1}{2}$ O atoms per side, which gives a total of $\frac{1}{2}$ A-type ions and $\frac{3}{2}$ O atoms per cell. The next triangle with A and O atoms on the subsequent (111) plane, for example the triangle with edges at the points (1,1,0), (1,0,1) and (0,1,1), lies at a distance of $a/\sqrt{3}$ from the (1,1,1) point. Since the distance of the diagonal across the cube, connecting the points (0,0,0) and (1,1,1) is $\sqrt{3}a$, the distance in between these two AO_3 planes is $\sqrt{3}a - a/\sqrt{3} - a/\sqrt{3} = a/\sqrt{3}$. The B cation lies at the center of the cubic cell, a distance $(\sqrt{3}/2)a$ (along the [111] direciton) from the point (0,0,0) and therefore a distance $(\sqrt{3}/2)a - a/\sqrt{3} = (\sqrt{3}/6)a$ from the AO_3 planes.

Viewed from the [111]-direction (see Fig. 5.2), the AO_3 triangles of the perovskite crystal form a hexagonal lattice on the (111) plane. We define a two-dimensional cell on this plane that includes two triangles on the (111) plane as seen in the Fig. 5.3; thus,

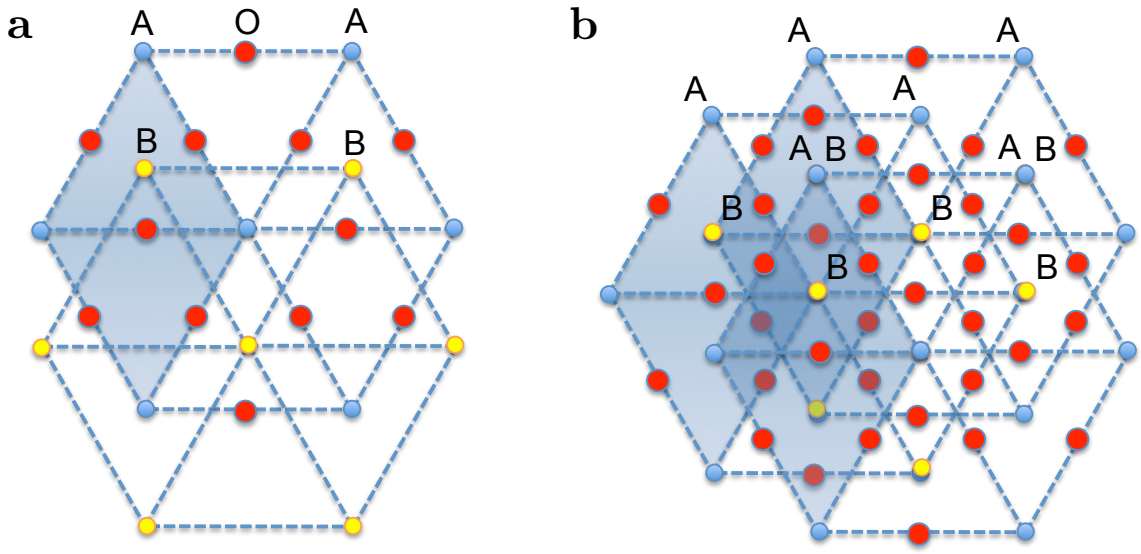

Figure 5.4: (a) One bilayer seen along the [111] direction in an ABO_3 perovskite. Blue, yellow and red circles represent the A, B and O atoms respectively. The newly defined cell consists of the blue shaded triangle of AO_3 and its corresponding B atom above it. Extra atoms are shown to illustrate the hexagonal coordination. (b) Stacking of three AO_3-B bilayers in an fcc closed packed-like *manner* to reproduce the full perovskite crystal symmetry.

each cell of AO_3 planes contains one A-type ion and three O atoms. To each double-triangle cell on the AO_3 plane corresponds a single B-type atom located a distance $(\sqrt{3}/6)a$ above the center of the top triangle. The B-sites also form a hexagonal lattice, and are stacked above the AO_3 lattice as shown in Fig. 5.4a, where only one B-layer above the AO_3 plane is shown. The full periodicity of the ABO_3 perovskite structure is thus achieved by stacking three AO_3-B bilayers in a face centered cubic (fcc) closed packed-like *manner* (see Fig. 5.4b), with periodicity of $a/\sqrt{3}$. In the case of $SrTiO_3$ with a lattice parameter $a = 3.905$ Å, the bilayer spacing is predicted to be 2.255 Å.

The elemental oxidation states in $SrTiO_3$ and $LaAlO_3$ are Sr^{2+}, Ti^{4+}, La^{3+}, Al^{3+} and O^{2-}. Therefore, the charge per cell in a SrO_3 layer is $-4e$ and its surface charge density is $\sigma = -4e/\sqrt{3}a^2$. In a similar fashion we can obtain the net charge per cell and surface

Table 5.1: Net charge per cell and surface charge densities of (111) layers in $SrTiO_3$ and $LaAlO_3$

Layer	Charge per cell (e)	σ (e/a^2)
SrO_3	-4	$-4/\sqrt{3}$
Ti	$+4$	$+4/\sqrt{3}$
LaO_3	-3	$-3/\sqrt{3}$
Al	$+3$	$+3/\sqrt{3}$

charge densities of each of the layers, shown in Table 5.1. In this way, [111]-oriented $LaAlO_3/SrTiO_3$ heterostructures provide a system in which both oxides are conformed of polar layers, in contrast with the commonly studied [001]-oriented $LaAlO_3/SrTiO_3$ polar/non-polar interface.

Furthermore, it is important to note that two consecutive B layers form a buckled honeycomb lattice as seen in Fig. 5.5. Electrons occupying open d shells in B sites of conducting transition metal oxides $LaNiO_3$ [98, 100] or $LaAuO_3$ [99] embedded on a band insulator perovskite, like $LaAlO_3$, are predicted to create topologically protected states. In the $LaAlO_3/SrTiO_3$ system, the electrons occupy the Ti $3d$ bands of the first few layers, which are then capped by band insulator $LaAlO_3$. Even though, the mechanism of conduction in the top layers of $SrTiO_3$ is polarization and dopant driven, the $LaAlO_3/SrTiO_3$ (111) interface will provide the same structural considerations as in the theoretical predictions of Refs. [98–100].

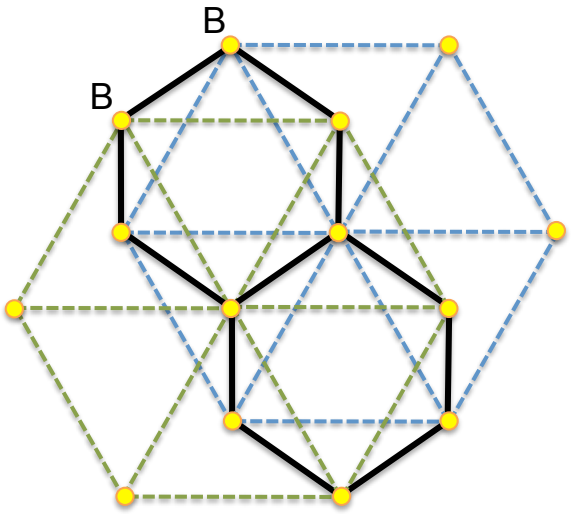

Figure 5.5: Two consecutive metallic B layers displaying the buckled honeycomb lattice. Blue and green dashed lines indicate the hexagonal lattice in two different (111) planes. Solid black lines indicate the buckled honeycomb lattice.

5.2 Methods

5.2.1 Sample Fabrication

We fabricated epitaxial $LaAlO_3/SrTiO_3$ heterostructures by growing $LaAlO_3$ on $SrTiO_3$ (111) with atomic layer controlled pulsed laser deposition (PLD). Processing methods that include chemical etching and thermal annealing of $SrTiO_3$ (111) single crystal substrates were reported to create atomically smooth surfaces with metallic Ti termination [102]. Before deposition, $SrTiO_3$ substrates were soaked in de-ionized water for 10 minutes and chemically etched with buffered HF solution for 1 minute, and then annealed at 1050°C for 3–6 hours in oxygen flow. All $LaAlO_3$ films were grown at 550°C and $p_{O_2} = 10^{-3}$ mbar with no post-growth annealing. The $LaAlO_3$ thickness and crystallinity were monitored by *in-situ* reflection high-energy electron diffraction (RHEED). Intensity oscillations of the specular spot as a function of time shown in Fig. 5.6 confirm the $LaAlO_3$ layer-by-layer growth. The RHEED pattern after 20 RHEED oscillations remains similar to that of the bare $SrTiO_3$ substrate, indicative of epitaxial coherent growth of $LaAlO_3$. Atomic force microscopy (AFM) images were taken of the treated $SrTiO_3$ substrates and the deposited $LaAlO_3$ layer (Fig. 5.7) showing equivalent clear steps and terraces. The measured step height was of 2.23 and 2.21 Å respectively, similar to the predicted spacing between bilayers along the [111]-direction of 2.255 Å.

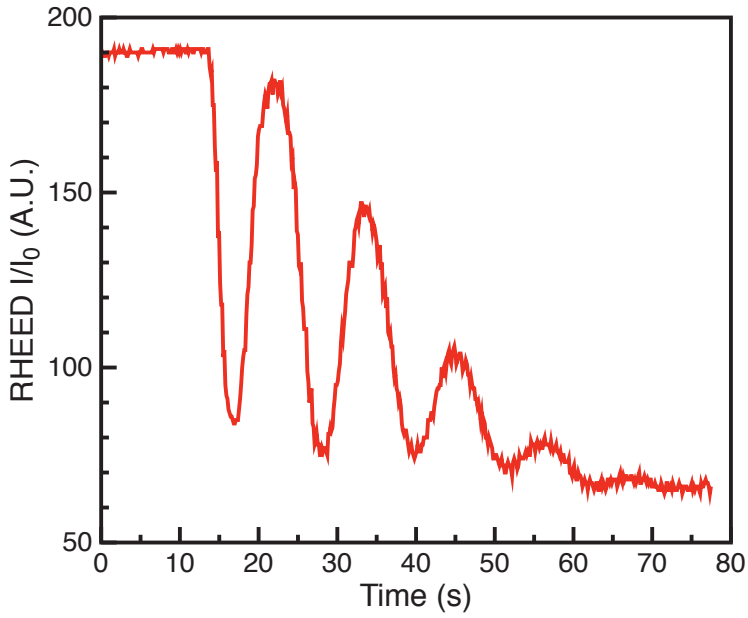

Figure 5.6: Reflection High-Energy Electron Diffraction oscillations during deposition of the $LaAlO_3$ layer.

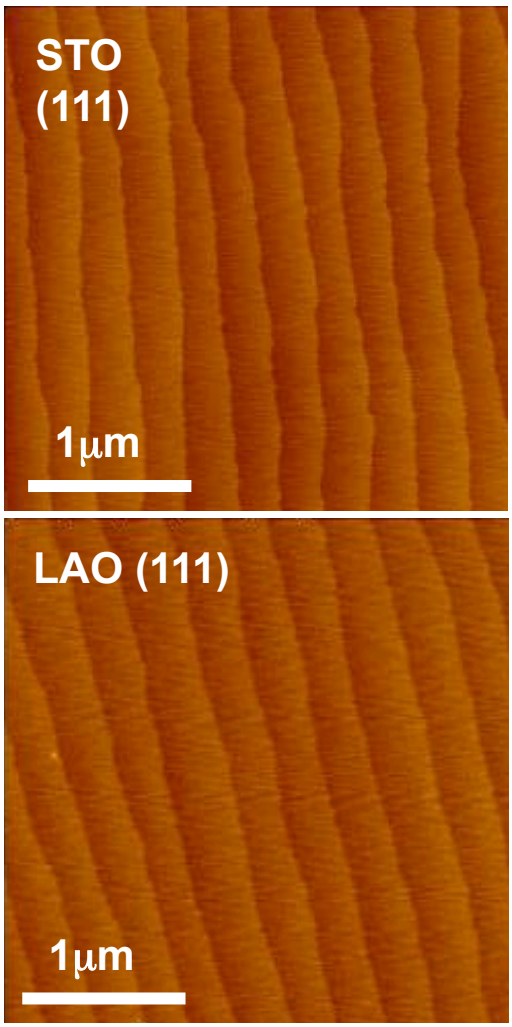

Figure 5.7: AFM images of the $SrTiO_3$ bare substrate and the deposited $LaAlO_3$ layer along the [111] direction.

5.2.2 Transport Measurements

For the majority of the samples, we directly bonded wires directly onto the samples to exclude the effect of polar adsorbates Immediately after growth, we mounted the heterostructures on ceramic chip carriers and bonded aluminum wires with a West Bond wedge ultrasonic bonder in the four corner van der Pauw configuration. Upon loading the chip carriers in the cryostats, we let the samples stabilize in the dark environment before performing magnetotransport measurements to prevent artifacts due to photo-induced carriers, a step crucial in particular for higher resistive samples. We used two different cryogenic system to measure temperature dependence of electroc properties. For the temperature range 300–20 K we used a closed-cycle helium gas cryostat model 261265A by APD with compressor model HC-4 by APD mounted on an electromagnet to with a maximum magnetic field of $\mu_0 H = 0.7$ T at the required pole spacing. Below $T = 20$ K we used an Oxford Instruments MagLab 2000 liquid helium, sample in flowing gas cryostat with an integrated superconducting magnet with a maximum field of $\mu_0 H = 8.3$ T. On select samples, we performed additional transport characterization using a custom-designed L-shaped Hall-bar pattern (shown in Fig. 5.8) that restricts the current paths and allows for precise measurement of R_{xx} and R_{xy} on two perpendicular current directions to probe for anisotropy across the sample surface.

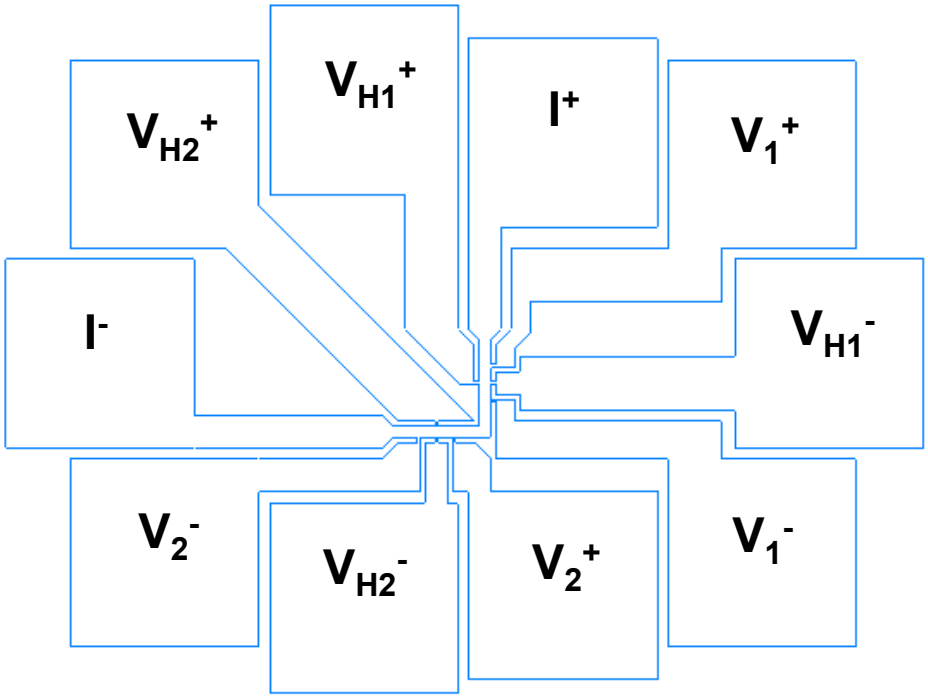

Figure 5.8: L-shaped pattern containing two perpendicular measurement arrangements for measurement of R_{xx} and R_{xy}.

5.2.3 Surface X-ray Diffraction and COBRA

The atomic structure of $LaAlO_3/SrTiO_3$ (111) heterostructures was investigated at beamline 12-ID-D of the Advanced Photon Source at Argonne National Laboratory by measuring the diffraction intensities along the substrate-defined symmetry non-equivalent crystal truncation rods (CTRs). The measurements were conducted on a six-circle Huber goniometer, using an x-ray energy of 16 KeV ($\lambda = 0.7749$ Å). The x-ray beam with a profile of 40 μm (vertical) $\times$ 500 μm (horizontal) has a flux of 1×10^{12} photons per second. The two-dimensional scattering images of CTRs at each step in the reciprocal lattice unit were recorded with a pixel array area detector (Dectris PILATUS 100 K). The L-scans along the specular CTRs were obtained by properly removing the background scattering contributions using the area detector images. Subsequently, COBRA was used to extract the three-dimensional electron density profile along the [111] direction. COBRA is an x-ray phase-retrieval method which uses the fact that the complex structure factors (CSFs) vary continuously along the CTR to determine the diffraction phases from the measured diffraction intensities. The CSFs are then Fourier transformed into real space to obtain the electron density profile of the film and substrate with sub-angstrom resolution. It is the most effective technique to determine layer resolved atomic structures on epitaxial thin films. The samples analyzed with this technique were a bare, treated $SrTiO_3$ substrate and $LaAlO_3$ films on $SrTiO_3$ (111) with thicknesses of 3 and 20 bilayers.

5.2.4 Theoretical Modeling

Density functional theory (DFT) is used to perform calculations from first-principles, as implemented within the Vienna *ab initio* simulation package (VASP) [103]. The projected augmented wave (PAW) method is used to approximate the electron-ion potential, and the local density approximation (LDA) is used to include exchange and correlation effects. $LaAlO_3/SrTiO_3$ (111) interfaces are constructed using a supercell geometry where a n-bilayer $LaAlO_3$ (n = 5, 6, 8, 9 and 16) is placed on top of a m-bilayer $SrTiO_3$ ($m = 3$), both stacked in the [111] direction, and a 1.5 nm vacuum layer separates the $LaAlO_3/SrTiO_3$ structure. We assume that the interface is LaO_3/Ti terminated as follows from our COBRA data. The constructed stoichiometric supercell contains a polar bottom surface of a $(SrO_3)^{4-}$ atomic layer and thus produces an electric field in $SrTiO_3$. To eliminate this unphysical field we remove an O atom to form a $(SrO_2)^{2-}$ atomic layer and thus a non-polar bottom surface of $SrTiO_3$. To preserve stoichiometry of the system we put this atom at the top layer of $LaAlO_3$ to create an AlO_2 atomic layer of the surface. The resulting stacking sequence of the system is:

$$AlO/LaO_3/Al/LaO_3/\ldots/Al/LaO_3/Ti/SrO_2/Ti/SrO_3/\ldots/Ti/SrO_2$$

The in-plane lattice constant of the superlattice is fixed to the calculated bulk lattice constant of $SrTiO_3$, i.e. $a = 3.905$ Å. To avoid an unphysical electric field in vacuum due to periodic boundary conditions of the supercell, a dipole layer is introduced in vacuum to cancel this field. In the calculation, we use a kinetic energy cutoff of 340 eV for the plane wave expansion of the PAWs and an equally spaced mesh of $4 \times 3 \times 1$ k points in the $[1\bar{1}0]$, $[11\bar{2}]$, and [001] directions, respectively, for Brillouin zone integration. All the ionic positions are relaxed until the atomic forces are less than 0.01 eV/Å.

5.3 Structure of the Top (111) Surface in a Bare $SrTiO_3$ Substrate

Surface x-ray diffraction and COBRA of a treated Ti-terminated $SrTiO_3$ substrate shows non-trivial CTR intensity variations (Fig. 5.9) in the mid-zones between substrate defined Bragg peaks [(003), (006) and (009)]. Such variations would not appear if the substrate is perfect and has no surface modifications (e.g. lattice distortion, surface off-stoichiometry, or charged adsorbates). The electron density profile of the $SrTiO_3$ (111) surface can only be determined with a model that designates Ti as the top most layer, (using a SrO_3 termination yields a bad fit) and is shown in Fig. 5.10. The electron density variations of the layers near the surface is indicative of modifications of the surface. The chemical composition of each atomic layer is extracted based on the integrated intensities of corresponding peaks in the density profile. We observe a significant change in stoichiometry of subsurface SrO_3 and Ti layers, accompanied by a small amount of lattice distortions, both of which alleviate the diverging surface electrostatic energy (dashed line in Fig. 5.11).

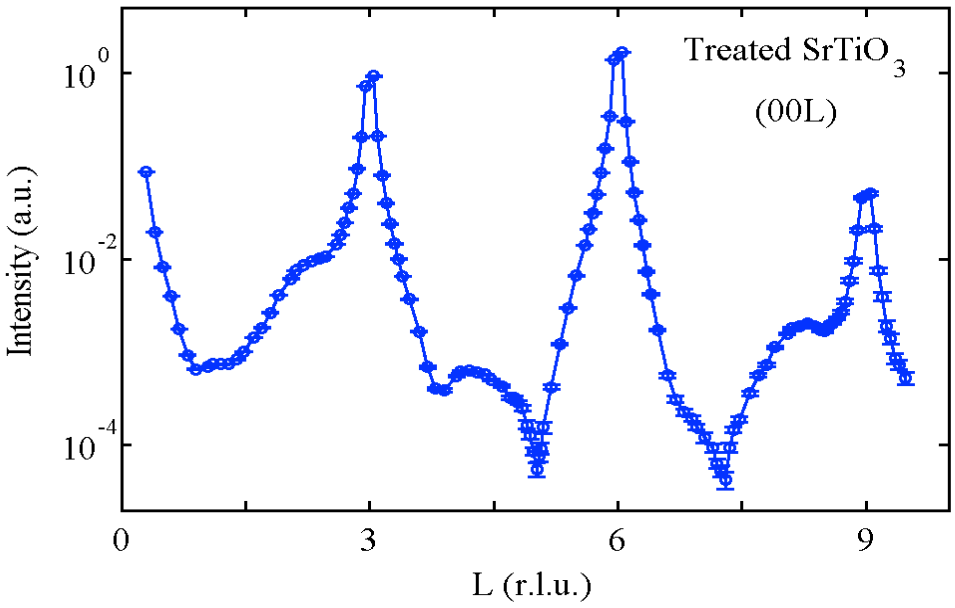

Figure 5.9: Specular CTR (00L) of a treated $SrTiO_3$ bare substrate.

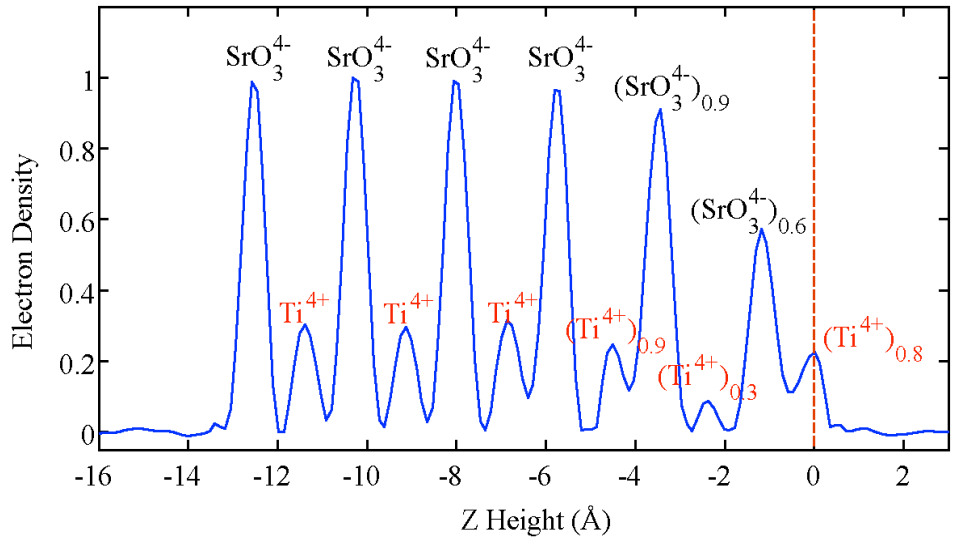

Figure 5.10: Experimentally determined electron density profile of the treated bare $SrTiO_3$ (111) surface.

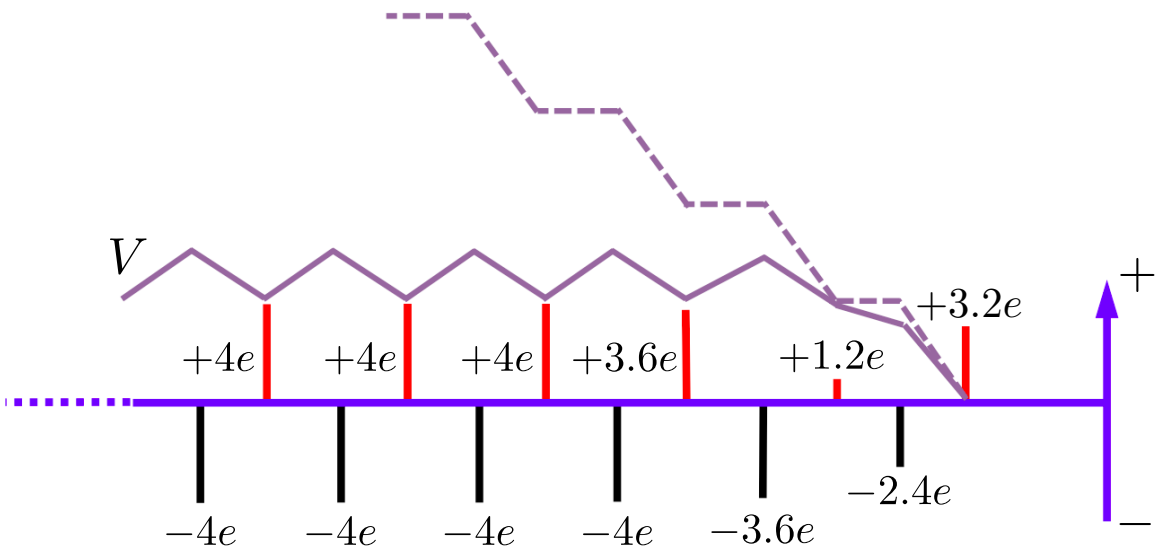

Figure 5.11: Schematic of the charge distribution and electrostatic potential, plane-by-plane near the surface of $SrTiO_3$ (111). Possible surface reconstruction (top Ti layer) and sub-surface off-stoichiometry (SrO_3 and Ti layer deficiency) alleviate a polar catastrophe, as illustrated by the dashed line, of the intrinsically polar (111) system.

5.4 Structural Analysis of the (111) $LaAlO_3/SrTiO_3$ Interface

COBRA of the high energy surface x-ray diffraction is used to determine the electron density distribution close to the surface of $LaAlO_3/SrTiO_3$ (111) heterostructures. The two-dimensional electron density maps around Ti ions of the two top most layers of $SrTiO_3$ (Fig. 5.12) shows the honeycomb coordination discussed in Section 5.1. The projection of three-dimensional electron density isosurface maps along [111] direction for $SrTiO_3$ (111) system is shown in Fig. 5.13, where one SrO_3 atomic layer together with two adjacent Ti atomic layers are overlaid. The bigger isosurface blue blob in the center of a honeycomb lattice represents an Sr atom and the smaller blue blob at the middle of the edge of a honeycomb lattice represents an O atom.

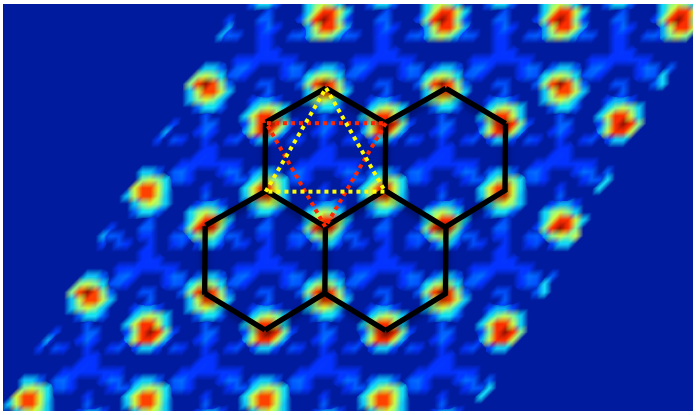

Figure 5.12: Two dimensional electron density maps at the Ti peak positions obtained by COBRA. Maps of the two Ti layers closest to the interface are overlaid, the yellow and red dotted triangles correspond to Ti layers above and below the SrO_3 plane, respectively. The black hexagons are guides to highlight the honeycomb-like coordination.

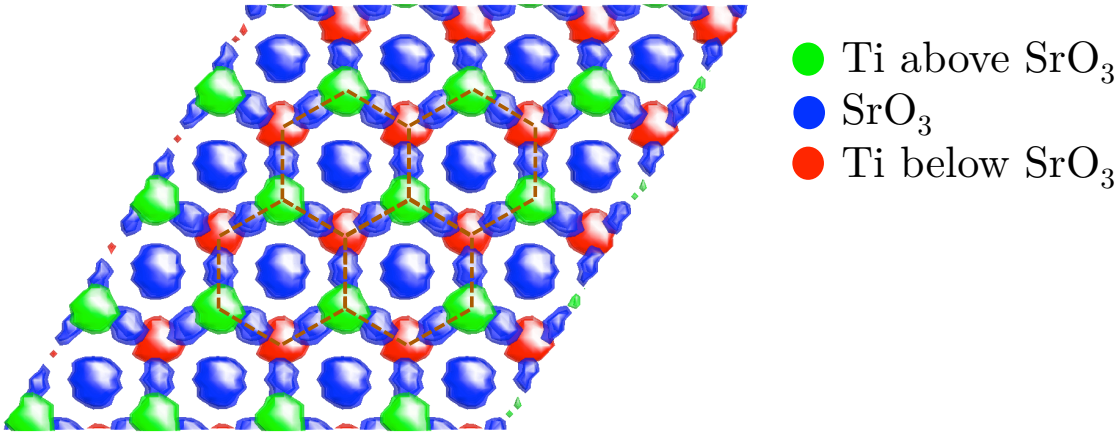

Figure 5.13: Three dimensional electron density isosurface maps of consecutive Ti-SrO_3-Ti layers.

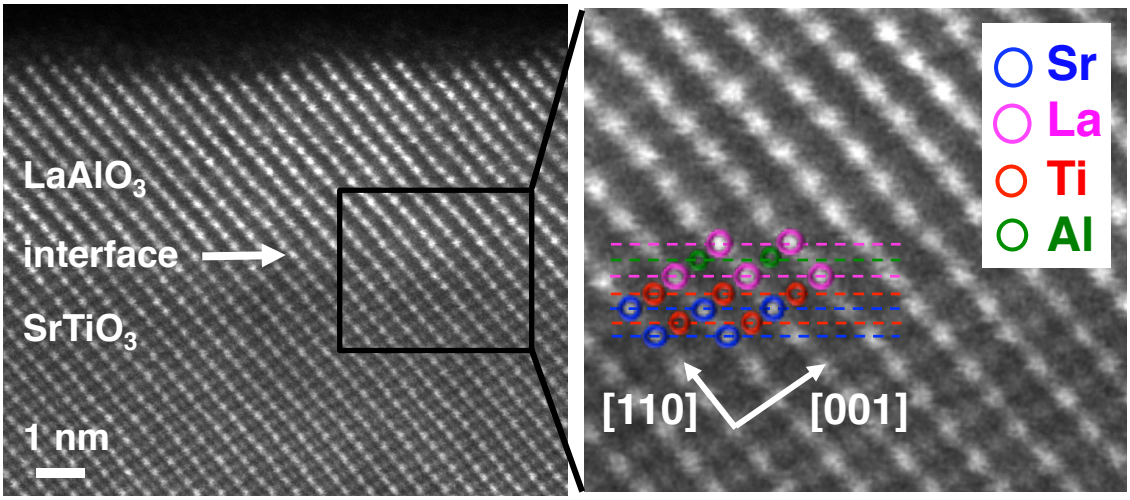

Figure 5.14: High-resolution cross-section TEM image of the coherent interface. Blue, navy, red and yellow circles are Sr, La, Ti and Al, respectively. Dashed line is the guide for each plane. The average bilayer spacing is 2.15 Å.

During PLD growth of $LaAlO_3$ films on $SrTiO_3$ (001) substrates, one complete RHEED oscillation corresponds to the deposition of an individual $LaAlO_3$ unit cell with constant surface roughness [3, 86]. However, as suggested by the step height observed in AFM, this is likely not the case depositions along the [111]-direciton.

The high-resolution cross-sectional TEM of a $LaAlO_3$ film on $SrTiO_3$ (111) for 20 RHEED oscillations (Fig. 5.14) shows 20 rows of heavy La atoms (bright spots) above the interface. This indicates that one RHEED oscillation during PLD corresponds to the deposition of a single LaO_3-Al bilayer with an average bilayer spacing of 2.15 Å.

5.5 Pre-reconstructed Interface

Let the *equivalent surface charge density* be the charge density required to produce the same internal electrostatic potential at the top and bottom of a layer of the same material In a polarization catastrophe scenario, the equivalent surface charge densities would be non-zero, increasing the potential difference between the interface and top layer with increasing $LaAlO_3$ thickness. Assuming the bare $SrTiO_3$ (111) substrate has undergone a reconstruction at its surface (as indicated by COBRA, see section 5.3), we can conceive an electrostatic scenario in which the substrate does not contribute to the internal fields at the interface (similar to the one done in Ref. [12]); such fields would have been previously alleviated. A schematic of this model is shown in Fig. 5.15, where σ_{top} and σ_{int} are the equivalent surface charge densities at the top and bottom of the $LaAl_3$ layer. The surface charge densities of each layer have already been calculated and are shown in Table 5.1. The electric field between an Al^{3+}-$(LaO_3)^{3-}$ bilayer is then:

$$E = \frac{\sigma}{\epsilon} = \frac{3}{\sqrt{3}} \frac{e}{\epsilon a^2} \tag{5.1}$$

and points towards the interface. The arrows in Fig. 5.15 show the internal electric fields in units of $(e/\sqrt{3}\epsilon a^2)$. Let m be the number of Al-LaO_3 bilayers and d be the bilayer spacing, the potential difference between the interface and the top of the film is:

$$\Delta V = -\int_c \mathbf{E} \cdot \mathbf{dl} = E \cdot \frac{1}{2} \cdot d \cdot m = \frac{1.5e}{\sqrt{3}\epsilon a^2} \cdot d \cdot m \tag{5.2}$$

An equivalent electrostatic potential is created by *equivalent* surface charge densities $-\sigma_{eq}$ at the interface and $+\sigma_{eq}$ top layer given by:

$$V_{eq} = \frac{\sigma_{eq}}{\epsilon} \cdot d \cdot m \tag{5.3}$$

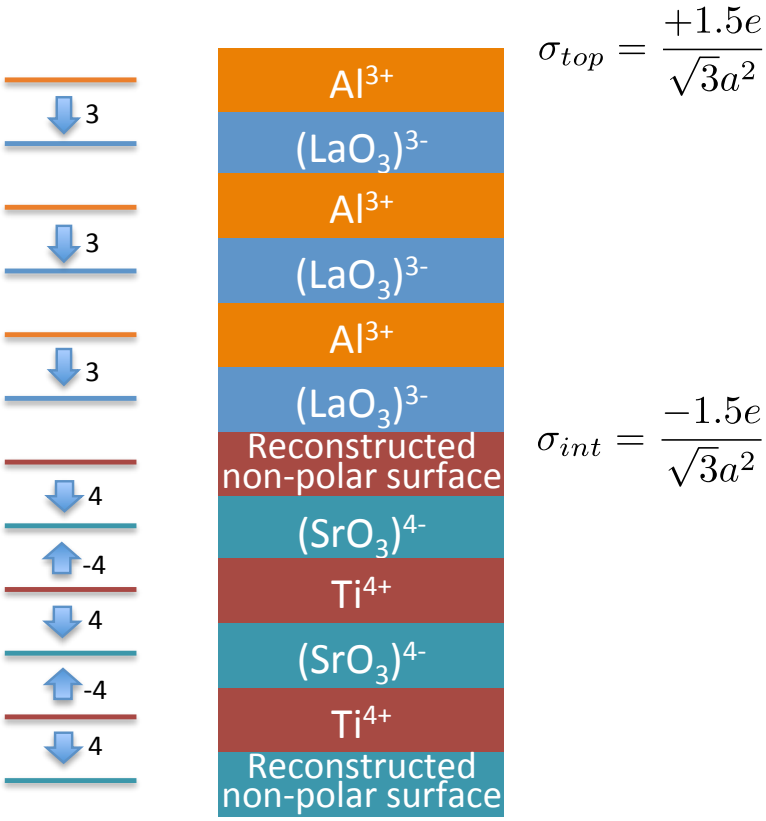

Figure 5.15: Schematic of the layers of $LaAlO_3/SrTiO_3$ (111) structure in the case when the top layer of $SrTiO_3$ is reconstructed and non-polar.

Setting both potentials (Eq. 5.2 and 5.4) equal we obtain:

$$\sigma_{eq} = \frac{1.5e}{\sqrt{3}a^2} \tag{5.4}$$

Therefore, a diverging electrostatic potential will accumulate with increasing $LaAlO_3$ layer thickness unless a positive charge is transferred to the interface from the top in order to balance σ_{int}, and creating a p-type conducting channel.

5.6 Evidence of an n-type Conducting Channel

We characterized temperature dependent magnetotransport of both [111]- and [001]-oriented heterostructures for comparison. We used both the four corner van der Pauw technique, and the L-shaped Hall-bar pattern in Fig 5.8, yielding consistent results. Contrary to the reconstruction scenario discussed in Section 5.5, we found all conducting samples to have Hall coefficients consistent with n-type carriers. Anisotropy due to uneven coverage of the $LaAlO_3$ film was not observed in the two directions and positions of the Hall bars.

Transport measurements in [111]-oriented heterostructures with varying $LaAlO_3$ thickness show a non-abrupt transition from an insulating to a conducting state, in contrast with the transition seen in [001]-oriented films (see Fig. 5.16). In our $LaAlO_3/SrTiO_3$ (001) heterostructures, the transition is abrupt in sheet resistance and sheet carrier density at a critical thickness of 4 bilayers (also reported in [13]). On the other hand, the transition is broad in the (111) structure, showing an insulating state below 6 bilayers and saturation at $R_s \sim 10^4\ \Omega/\Box$ and $n_s \sim 10^{14}\ \mathrm{cm}^{-2}$ above 15 bilayers. Such saturation of transport with increasing thickness was not observed on previously reported $LaAlO_3/SrTiO_3$ (111) [101]. Herranz et al. report quick degradation of conductivity with increasing $LaAlO_3$ layer deposited along the [111]-direction, with resistances of order $\sim 10^6\ \Omega$ for 22 bilayer samples [101]. The transport properties in our samples had low reproducibility in the $LaAlO_3$ thickness transition range, as indicated by the error bars in Fig. 5.16. A possible cause for this can be incomplete coverage found in our x-ray measurements and COBRA (see Fig. 5.17), where intensity drops of the electron density profiles near the top surface of the $LaAlO_3$ overlayer indicate variability in the coverage of the deposited film from the nominal thickness reported from the number of RHEED oscillations. The integrated electron numbers can be determined for each atomic layer

and are shown in Fig. 5.18. Tails of electron number at the top most atomic layers also point to partial coverage of the $LaAlO_3$ film. The interface widths are estimated to be 0.7 nm and 1 nm, or about 3 and 5 bilayers in the [111]-direction. Similar measurements from surface x-ray diffraction experiments on $LaAlO_3/SrTiO_3$ (001) have found similar rough interfaces with widths of a few unit cells, attributing them to cation intermixing [36, 104]. Therefore we can not rule out intermixing effects in our (111) interface. After saturation on thickness has been reached, the conducting (111) interfaces have higher carrier densities than that of similarly prepared $LaAlO_3/SrTiO_3$ (001) as shown in Fig. 5.16b.

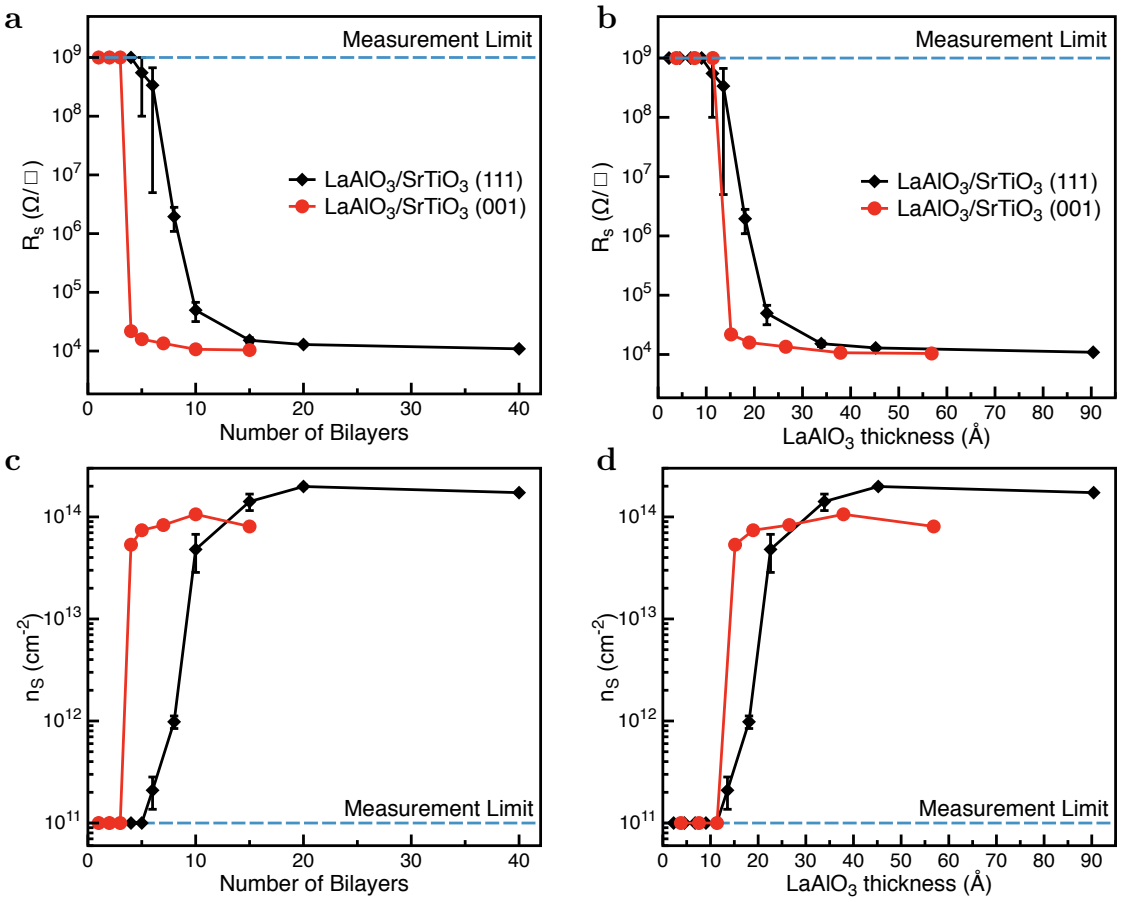

Figure 5.16: Room temperature (a) sheet resistance and (b) sheet carrier density as a function of the number of deposited $LaAlO_3$ bilayers on $SrTiO_3$ (111).

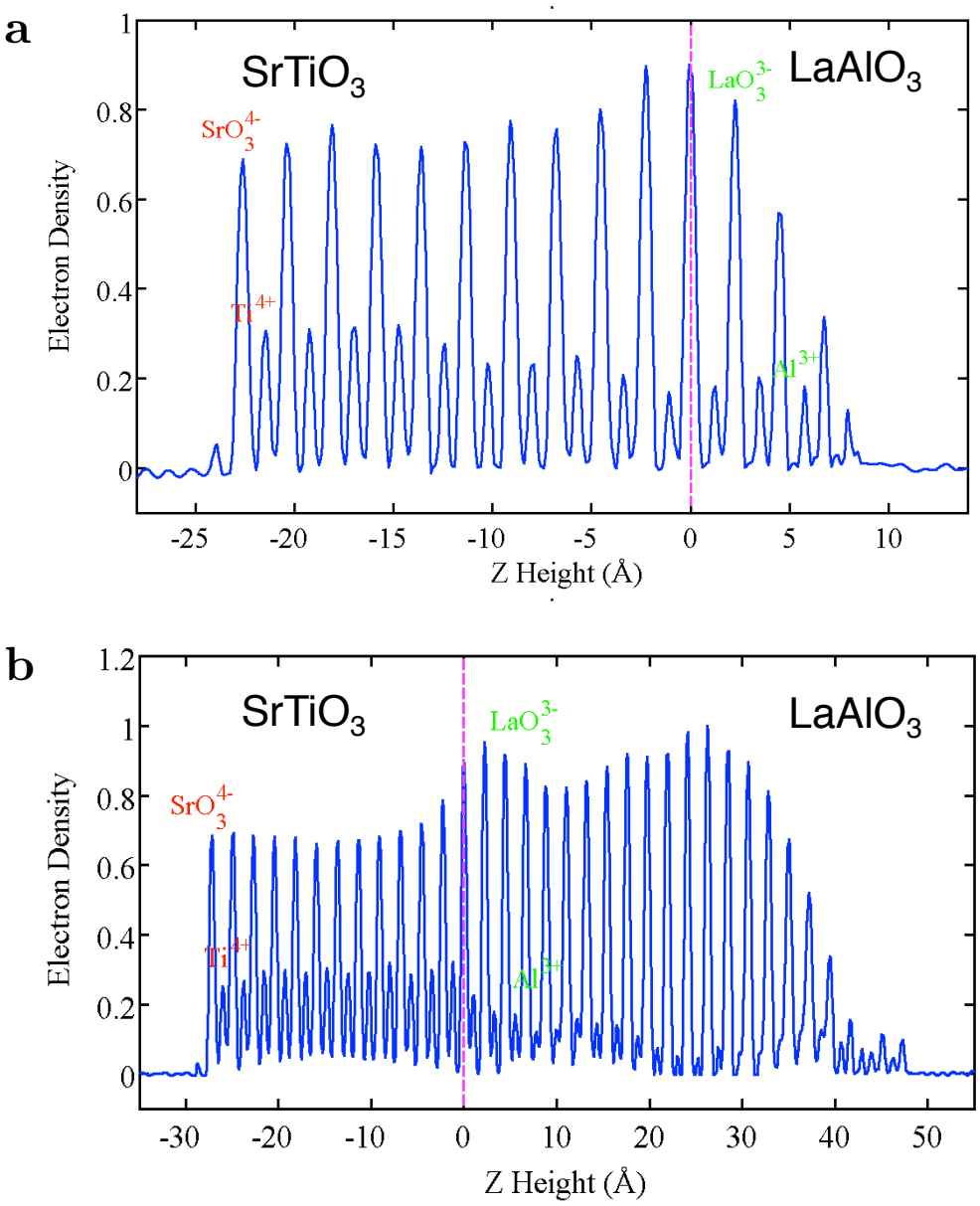

Figure 5.17: Electron density profiles of the (a) 3 and (b) 20 bilayer thick $LaAlO_3$, as a function of Z height, measured from the interface.

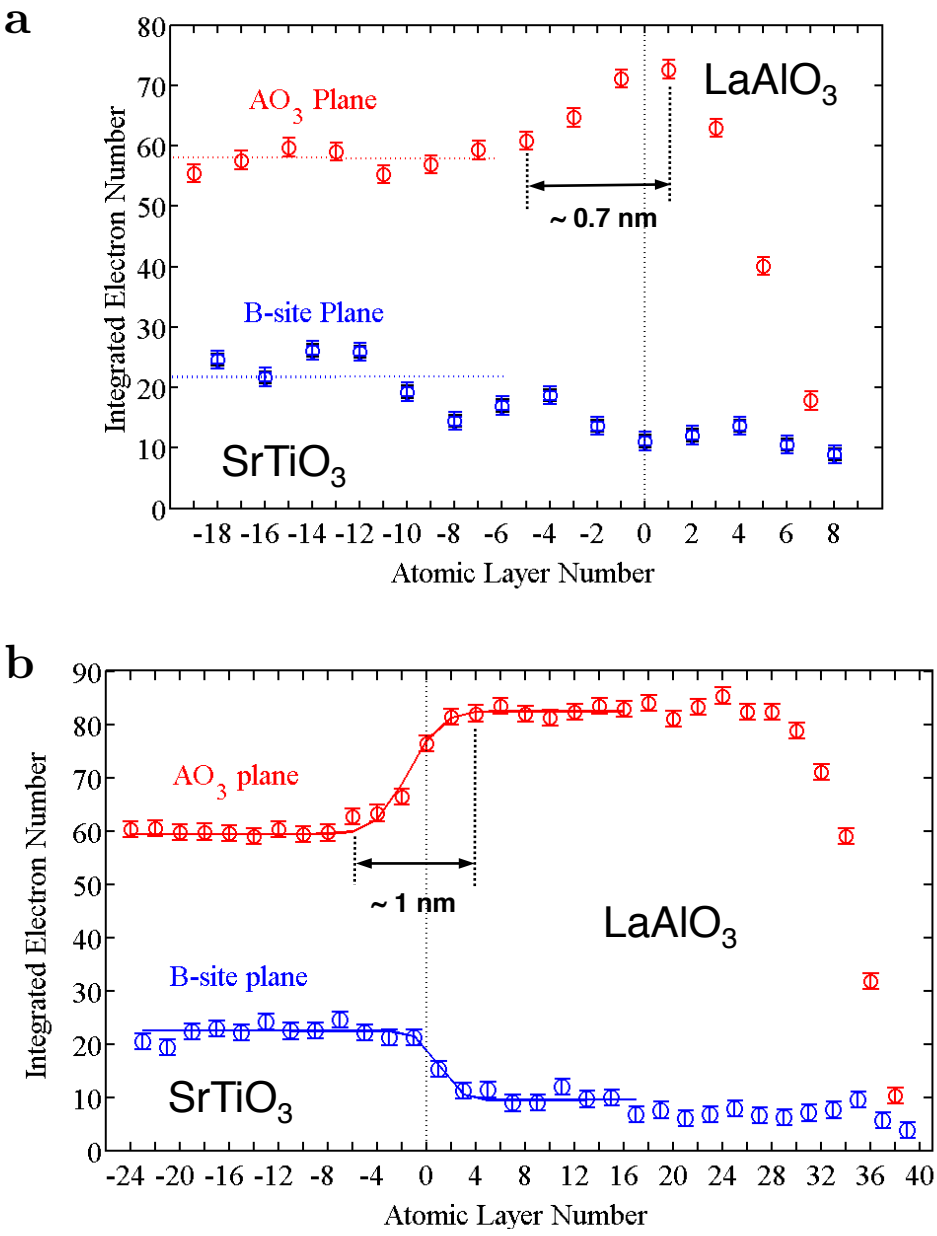

Figure 5.18: Integrated electron number profiles of the (a) 3 and (b) 20 bilayer thick $LaAlO_3$, as a function of atomic layer.

Table 5.2: Transport Properties of (001) and (111) $LaAlO_3/SrTiO_3$ Interfaces at Room Temperature

Interface	n_s (cm^{-2})	μ_H (cm^2/Vs)
(111)	1.7×10^{14}	3.2
(001)	8.8×10^{13}	5.3

Table 5.3: Transport Properties of (001) and (111) $LaAlO_3/SrTiO_3$ Interfaces at $T = 3$ K

Interface	n_s cm^{-2})	μ_H (cm^2/Vs)
(111)	1.9×10^{13}	725
(001)	1.8×10^{13}	3500

We measured the temperature dependence of transport properties of 20 bilayer $LaAlO_3$ (111) sample, a thickness well beyond the conductor transition, and is compared to a (001) sample with the same bilayer thickness (see Fig. 5.19). Values of transport properties at room temperature and $T = 3$ K are shown in Tables 5.2 and 5.3, respectively. Our (111) sample shows metallic behavior in the temperature range 3–300 K, in contrast with an upturn in resistance previously reported for $LaAlO_3/SrTiO_3$ (111) samples with comparable $LaAlO_3$ thickness [101]. The room temperature n_s of the (111) sample was almost twice as the (001) counterpart whereas μ_H was smaller in the (111) interface (see Table 5.2). The low temperature n_s saturates at an almost identical value for both types of interfaces but μ_H is a factor of ~ 5 smaller in the (111) sample. This reduced mobility can be explained in terms of increased scattering at the rough interface observed, but since there is a lack of understanding on the specific band occupation of the carriers in this (111) system, it is difficult to determine if this effect is due effective mass or relaxation times.

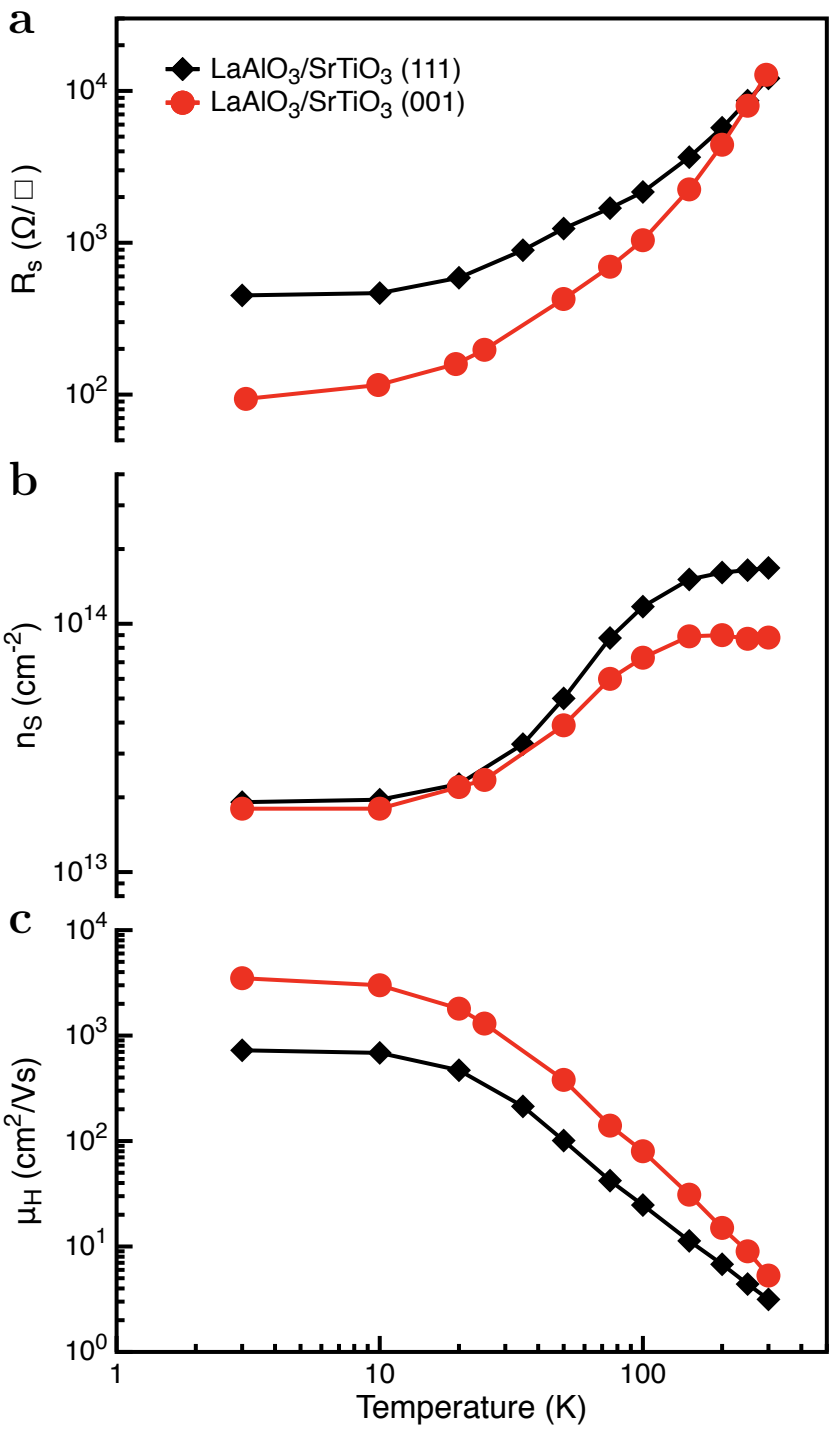

Figure 5.19: Comparison of the temperature dependence of the (a) sheet resistance, (b) sheet carrier density and (c) Hall mobility of 20 bilayer thick $LaAlO_3$ on $SrTiO_3$ (111) and (001). Black diamonds and red circles represent the (111) and (001) $LaAlO_3/SrTiO_3$ interfaces, respectively.

5.7 Polarization Driven Reconstruction

The transport measurements show that the interface hosts an n-type carriers contradicts our prediction in Section 5.5, and indicate an internal electric field in the $LaAlO_3$ layer that points away from the interface. We propose that the $LaAlO_3/SrTiO_3$ heterostructure is qualitatively different than reconstructed $SrTiO_3$, and that polar issues in both $LaAlO_3$ and $SrTiO_3$ are resolved by an electronic reconstruction well above the thickness transition into a conducting interface. We performed DFT calculations using the model in Fig. 5.20, assuming a LaO_3/Ti termination (for details see Section 5.2.4). The layer-resolved density of states in Fig. 5.21 shows the transition from insulator at 6 bilayers of $LaAlO_3$ to conductor at 8 bilayers, which is only in partial agreement with the transport measurements in Section 5.6. This is evident from the Fermi energy lying in the band gap for the 6 bilayers heterostructure (Fig. 5.21a) and in the Ti $3d$ conduction band for the 8 bilayers heterostructure (Fig. 5.21b). Even though DFT calculations of this idealized interface do not model the case of the non-abrupt transition measured, it does provide an insight of the internal fields and reconstruction that lead to an n-type interface. The red dashed line in Fig. 5.21 traces the valence band edge across the interface. In the $SrTiO_3$ layers the edge remains constant in energy, indicating constant electric potentials and no internal field. On the other hand, the slant of the trace of the band edge in the $LaAlO_3$ layer shows a change electrostatic potential, which in turn indicates an internal electric field.

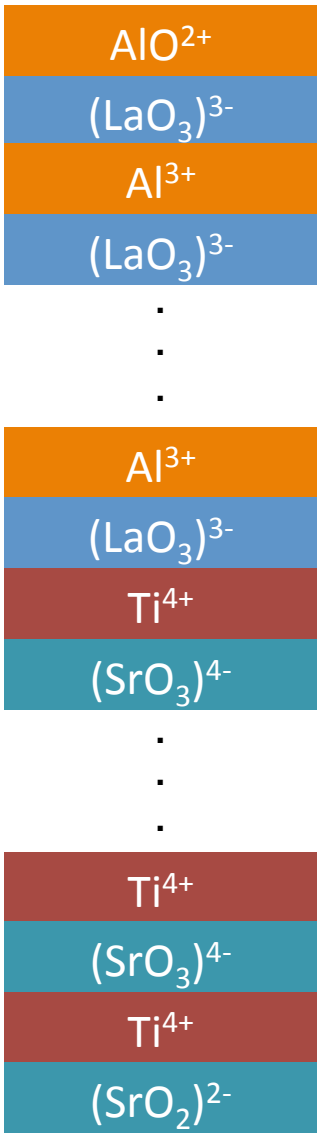

Figure 5.20: Schematic of the layers of $LaAlO_3/SrTiO_3$ (111) structure in the case of a perfect interface.

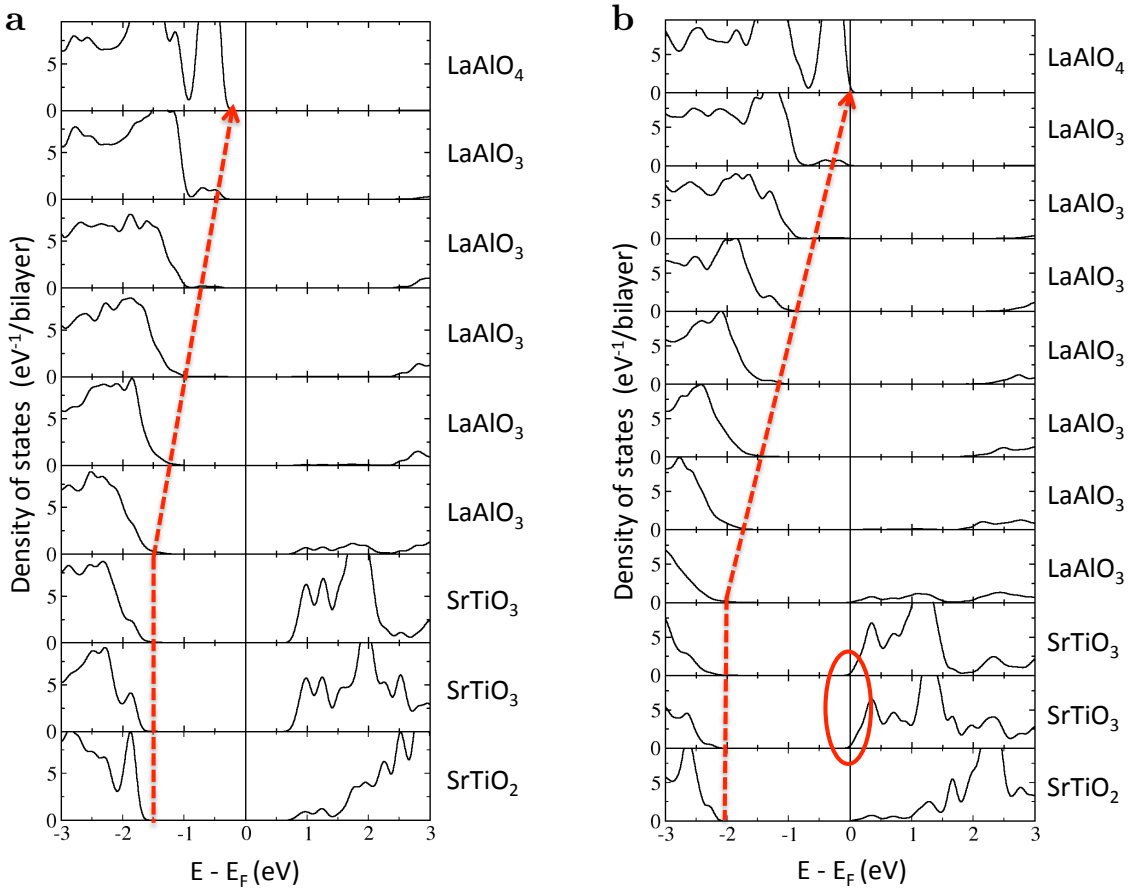

Figure 5.21: Layer resolved density of states calculations for (a) 6 and (b) 8 bilayers of $LaAlO_3$ on $SrTiO_3$ (111).

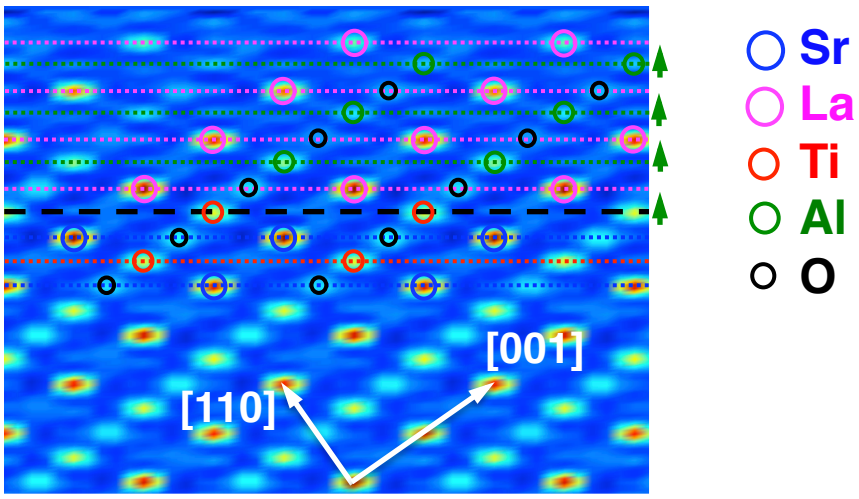

Figure 5.22: Charge density of a plane slice of a 3 bilayer $LaAlO_3/SrTiO_3$ heterostructure in the same crystallographic direction as Fig. 5.14 measured by COBRA x-ray diffraction.

An internal field in the $LaAlO_3$ layer is also observed by structural results from COBRA, where the three-dimensional atomic positions above and below the (111) interface are determined for samples with 3 and 20 bilayers of $LaAlO_3$. A slice of through the three-dimensional charge density map perpendicular to the interface for the 3 bilayer samples is shown in Fig. 5.22. The positively charged Ti layer is not centered between the negatively charged LaO_3 layers, but is rather offset away from the interface, indicating atomic rumpling due to a polar field in the $LaAlO_3$ layer [105].

We determined the B-site off-center displacements, defined as the difference between half distance between of two AO_3 layers and the distance between a B and an AO_3 layer, and the spacing between bilayers from COBRA for the 3 and 20 bilayer $LaAlO_3$ samples. These parameters were also calculated from DFT assuming the perfect interface, as discussed in Section 5.2.4 and the same $LaAlO_3$ thicknesses. Figure 5.23 summarizes the comparison between the measured and theoretically predicted parameters. The bulk values for $SrTiO_3$ (111) and $LaAlO_3$ (111) are indicated in red and brown dashed

lines, respectively, and the elastic limit of the deformation for the $LaAlO_3$ layer under triaxial strain is calculated from Poisson's ratio and shown as the pink dashed line. The measured off-center displacements of the insulating 3 bilayer thick sample are larger than the theoretical prediction from the ideal interface (see Fig. 5.23a), whereas in the 20 bilayer samples show displacement distributed around the center (see Fig. 5.23b). This is caused by reduced atomic rumpling due to internal fields in the $LaAlO_3$ layer becoming resolved by a reconstruction in the 20 bilayer sample.

Moreover, the bilayer lattice spacing of the insulating, 3 bilayer $LaAlO_3$ film is the same as to the spacing in the $SrTiO_3$ layer (see Fig. 5.23c), which is not in the elastic limit of $LaAlO_3$ nor agrees with the theoretical prediction. On the other hand, the 20 bilayer film shows (see Fig. 5.23d) a gradual decrease in the $LaAlO_3$ bilayer lattice spacing approaching the elastic limit. This expansion along the [111] direction in the insulating sample can be attributed the electrostrictive effect caused by the internal field in $LaAlO_3$, similar to the one observed in $LaAlO_3/SrTiO_3$ (001) [106]. The 20 bilayer thick sample, showing saturated transport properties above the thickness transition, has undergone an electronic reconstruction that alleviated the internal fields and displays less atomic rumpling and electrostrictive effects.

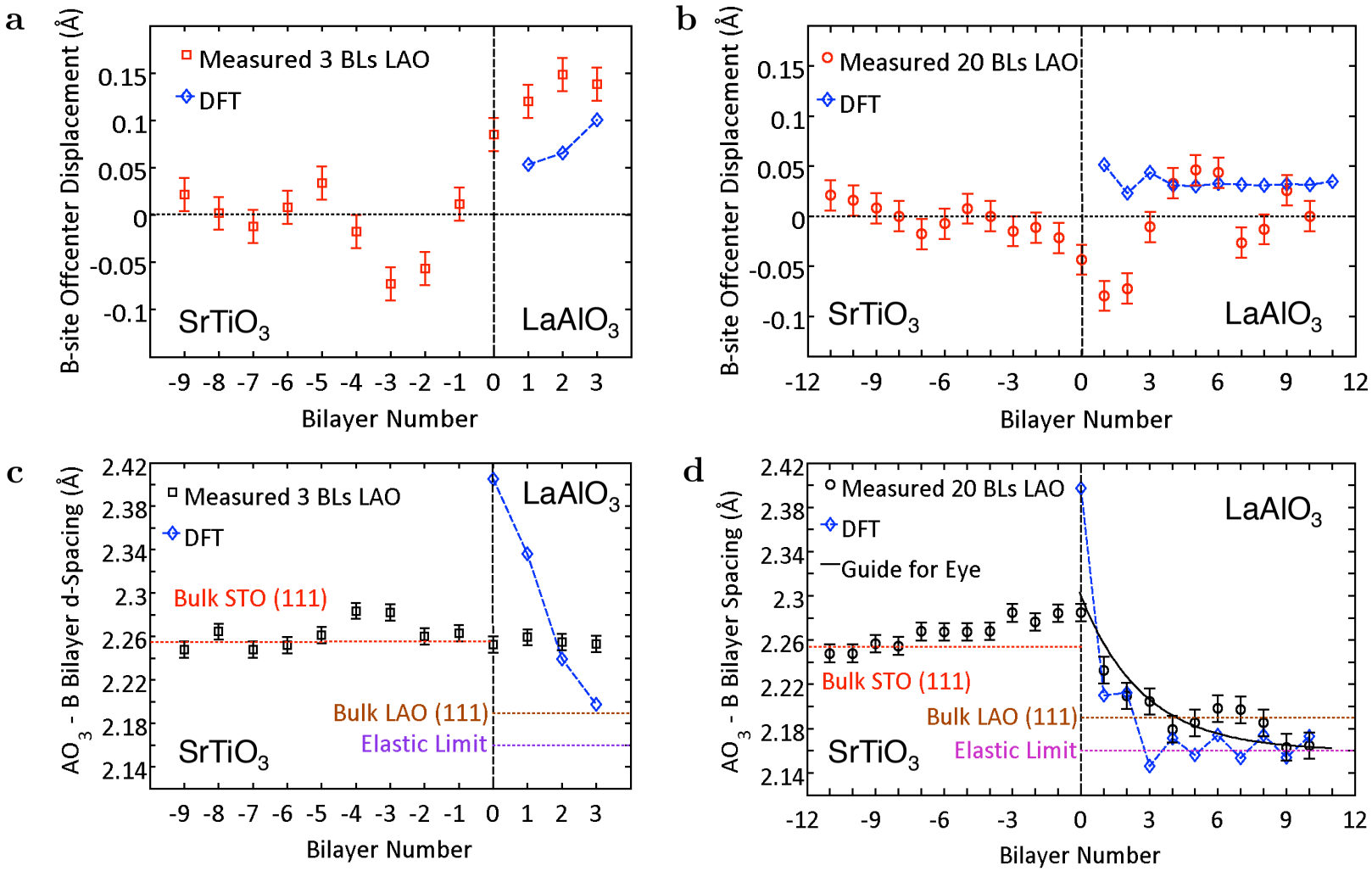

Figure 5.23: Comparison of measured and DFT calculated structural parameters of $LaAlO_3/SrTiO_3$ (111) structures. B-site off-center displacements for the (a) 3 bilayer and (b) 20 bilayer samples and bilayer spacing for the (c) 3 bilayer and (d) 20 bilayer. Blue lines represent the theoretical calculations, red and brown dashed lines represent bilayer spacing for bulk $LaAlO_3$ and $SrTiO_3$ (111), respectively. Pink dashed line represent the elastic limit of strained $LaAlO_3$ (111).

5.8 Concluding Remarks

Surface x-ray diffraction and COBRA of an etched and annealed $SrTiO_3$ (111) surface indicate a surface reconstruction and off-stoichiometry that eliminates the internal $SrTiO_3$ electric field in the [111]-direction. A polarization catastrophe scenario considering a $SrTiO_3$ (111) substrate with its internal fields resolved predicts the existence of a *p*-type conducting channel. This is contradicted by direct transport measurements of *n*-type carriers; furthermore, we observe a broad insulator-to-metal transition with increasing $LaAlO_3$ layer thickness. Incomplete or impartial film coverage or a rough, non-atomically sharp interface are possible causes for this non-abrupt thickness transition. Theoretical DFT calculations that assume a perfect LaO_3-Ti interface predict *n*-type charge carriers and internal polar fields in the $LaAlO_3$ layer. COBRA structural parameters from an insulating and a conducting heterostructure further indicate a polar field driven reconstruction. The $LaAlO_3/SrTiO_3$ (111) interface proves to be a challenging system, where atomically sharp interfaces are hard to create due to the initially reconstructed (111) surfaces of the polar substrate. We show an interplay between structural and electronic reconstructions at this interface and a polar-driven mechanism that creates an *n*-type two-dimensional electron system well above the broad transition with film thickness. Future work includes improving atomic sharpness at the interface, by preventing reconstruction at the polar substrate and studying the dimensionality and band occupation of this *n*-type conducting channel, for example high-field magnetotransport measurements would show quantum oscillations if the confinement of the electron gas is two-dimensional.

Chapter 6

Final Remarks

To summarize our findings, we identified two conduction regimes in an all thin-film $LaAlO_3/SrTiO_3$ system. The effect of oxygen partial pressure during growth directly affects the carrier density of the system. In the lower carrier density regime ($\sim 10^{13}$ cm^{-2}) we found a metallic to insulating temperature dependence and strong localization by disorder, whereas in the higher regime ($> 10^{14}$ cm^{-2}) we find metallic dependence with signs of weak localization. This is understood in the occupation of Ti $3d$ bands farther from the interface as carrier density is increased. All thin-film $LaAlO_3/SrTiO_3$ 2DEGs relieve the size constrain of the commercially available single crystal $SrTiO_3$ substrates, typically of dimensions 10×10 mm. Our work in the electronic properties of all-thin-film $LaAlO_3/SrTiO_3$ pioneers the understanding and implementations of this 2DEG to harness the richness of this oxide interface and its integration to industry standard substrates.

Furthermore, we showed the first conducting $LaAlO_3/SrTiO_3$ two-dimensional system grown by the physical vapor deposition technique: 90° off-axis sputtering. Films grown with this scalable technique have excellent crystalline quality and transport characteristics similar to those grown by the (mostly research employed) pulsed laser deposition technique. Writing of circuits on the nanoscale using the conducting-tip atomic force microscopy technique is demonstrated in sputtered $LaAlO_3$ on $SrTiO_3$, opening the doors to nanoelectronic application of this novel interfacial system.

We are among the first groups in the world to demonstrate conducting [111]-oriented $LaAlO_3/SrTiO_3$ heterostructures, a crystallographic orientation that proves to be challenging due to the large polar nature of perovskite oxides in this stacking direction. An interplay between structural and electronic reconstructions is at work to resolve the polarization divergence. This drives the $LaAlO_3/SrTiO_3$ (111) system from insulating to conducting with increasing $LaAlO_3$ thickness, displaying a broader transition than the conventional (001) system and a similar n-type conducting channel. The (111) interface between conducting and band-insulating perovskite oxides is suspected to host topologically protected electronic states due to the buckled honeycomb coordination of the metallic ions. Here we showed a conducting interfacial system between two band insulators that can serve as the starting point to investigate topological insulators at complex oxide interfaces.

Nine years after the discovery of the conducting state at the $LaAlO_3/SrTiO_3$ heterointerface, it has proven to be a rich multifunctional system with many novel electronic, magnetic and field-tunable properties. The research presented in this dissertation further expands the understanding and applicability of this system, facilitating modern technological implementations of this two-dimensional electron gas.

Appendix A

Photo-induced Mobility Enhancement of Conducting $LaAlO_3/SrTiO_3$ Interfaces

The two-dimensional electron gas (2DEG) at the $LaAlO_3/SrTiO_3$ interface provides many interesting electronic, magnetic and superconducting properties, but until recently, the electronic response to light has not been a focus of study in this system. The detection of photo-induced currents in nanoscale written devices by conducting-tip atomic force microscopy (c-AFM) methods was one of the first such studies [107]. It is important to note that in order to 'write' circuits with c-AFM, the starting system is an insulating $LaAlO_3/SrTiO_3$ interface, typically below the critical thickness of four unit cells. The result should not be surprising, since in a scanning tunneling spectroscopy and microscopy study on insulating, 2 unit cell thick $LaAlO_3/SrTiO_3$ was made conducting by inducing carriers to the interface from exposition to visible light [108]. This photo-induced conductivity was associated to promotion of carriers to in-gap trapped states [108].

Further studies focused on the macroscopic photoconductive response of highly resistive $LaAlO_3/SrTiO_3$ films exposed to UV light [109]. The characterized photoresponse to UV light followed a stretched exponential model with time of the form:

$$\frac{\Delta R(t)}{R_0} \sim \exp\left[-(t/\tau)^{\beta} \right] \tag{A.1}$$

Persistent conductivity enhancement of three orders of magnitude with exposure to UV (395 nm) and visible light was observed in highly resistive $LaAlO_3/SrTiO_3$, with recovery times on the order of days and full recovery only achieved after high temperature thermal cycling [110]. A different study found a resistance reduction of 50% on 10 nm thick $LaAlO_3$ on $SrTiO_3$ at $T = 4.2$ K when illuminating with light of energy 3.65 eV (339 nm), higher than the $SrTiO_3$ bandgap of 3.2 eV [111]. Before illumination, their structure has low mobility (3 cm^2/Vs) and report high mobility after illumination (1200 cm^2/Vs), attributed to multi-band transport of two different types of carriers. Unfortunately they do not report any transport properties at room temperature [111].

The $SrTiO_3$ bandgap is 3.2 eV (which corresponds to a wavelength of 387.5 nm) and illumination with photons of energies close to, or higher than this value will probe trapped interfacial states close to the valence or conducting bands or direct photo-induced promotion from the valence to the conducting band. Indeed, photo-luminescence experiments prove the existence of defect states created by oxygen vacancies on Ar^+-irradiated single crystal $SrTiO_3$. These trapped states occur 0.4 eV below the Ti $3d$ conduction band or 0.4 eV above O $2p$ valence band [112]. Furthermore, similar photoemission experiments have been used to show the existence of oxygen vacancies in $LaAlO_3/SrTiO_3$ and their role as the main conduction mechanism [24]. The light source used for excitation in these reports (Refs. [112] and [24]) was 325 nm and 350 nm, respectively.

While measurements of photoresistance with applied light show real-time switching, comprehensive studies of the Hall coefficient also with applied light are limited. In this appendixc we present a study to measure the response of transport properties as a

function of light exposition. We perform a wavelength response of the photoresistance using a spectrometer and then use 405 nm and 635 nm light from laser diodes to shine the sample and measure magnetotransport. At $T = 30$ K we observe clear reduced resistance after exposing the sample to light of these wavelengths; on the other hand, the Hall coefficient remains constant between samples shine with either light or in the dark. We thus attribute this to a mobility enhancement, estimated to be around 5% and 9% for the 635 nm and 405 nm, respectively. The samples used in this experiments were grown by S. Ryu in C. B. Eom's lab, the spectrometry measurements were performed by the author (T. H.) in M. Winokur's laboratory and temperature and light dependent transport was measured by the author (T. H.) in M. S. Rzchowski's laboratory.

A.1 Growth and Characterization

Layers of 10 unit cell thick $LaAlO_3$ were deposited by PLD on TiO_2 terminated $SrTiO_3$ with *in-situ* RHEED monitoring. In order to create a low resistance ($\sim 10^4$ $\Omega/\square$ at room temperature) 2DEG at the interfaces, the substrates were heated to a growth temperature of 550°C and the $LaAlO_3$ films were deposited at $p_{O_2} = 10^{-3}$ mbar, with no subsequent annealing. Intensity oscillations of the specular spot from RHEED show layer-by-layer controlled growth (see Fig. A.1) and the RHEED pattern after deposition of the $LaAlO_3$ layer is similar to the one of the bare $SrTiO_3$ substrate indicating epitaxial growth (see Fig. A.2).

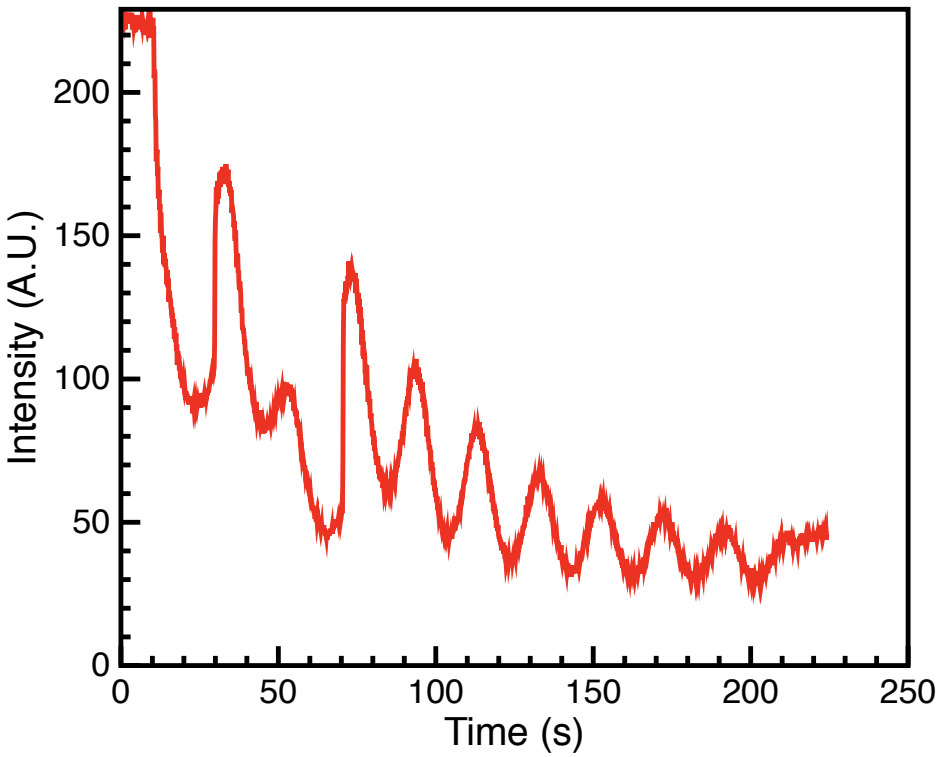

Figure A.1: Reflection High-Energy Electron Diffraction oscillations during deposition of the $LaAlO_3$ layer on $SrTiO_3$.

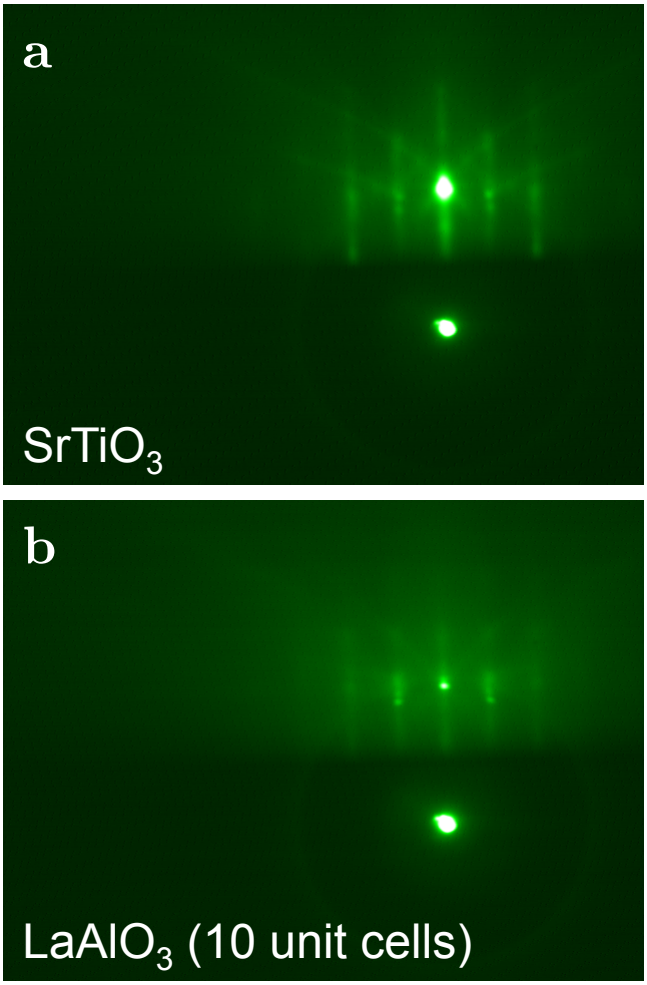

Figure A.2: Reflection High-Energy Electron Diffraction patterns of (a) the surface of the $SrTiO_3$ substrate and (b) after deposition of 10 unit cells of $LaAlO_3$.

Aluminum wires were ultrasonically bonded directly into the four corners of the samples and electronic transport was measured using the van der Pauw technique with a Keithley 2400 Sourcemeter and a Keithley 2700 Data Acquisition unit as previously described. To measure temperature dependent transport in a 'dark' environment over the temperature range 300–20 K we used a closed-cycle helium gas cryostat model 261265A by APD with compressor model HC-4 by APD mounted on a electromagnet with a maximum field of $\mu_0 H = 0.7$ T at the required spacing. The room temperature sheet resistance (R_s) was 1.2×10^4 $\Omega/\square$, which lies in the lower range for $LaAlO_3/SrTiO_3$ 2DEGs. We measured the behavior of R_s with temperature by a slow temperature ramp and by stabilizing the temperature at certain values of temperature, shown as the continuous red line and black circles in Fig. A.3 respectively. The samples showed metallic behavior down to $T = 20$ K. The room temperature sheet carrier density (n_s) was of order 1.1×10^{14} cm^{-2} and the Hall mobility (μ_H) was 4.74 cm^2/Vs. All Hall voltages were linear with applied magnetic field in the measured range (0–0.7 T) indicating single band transport. The temperature dependence of n_s and μ_H is typical to that observed in conventional $LaAlO_3/SrTiO_3$ heterostructures (see Fig. A.4). We do not observe saturation of μ_H down to $T = 20$ K, where it reaches a value of 351 cm^2/Vs, suggesting a high-mobility electron gas at lower temperatures. The carrier density shows a downturn starting at $T = 100$ K, which is commonly observed in high-mobility $LaAlO_3/SrTiO_3$ (for example see Refs. [14, 63]).

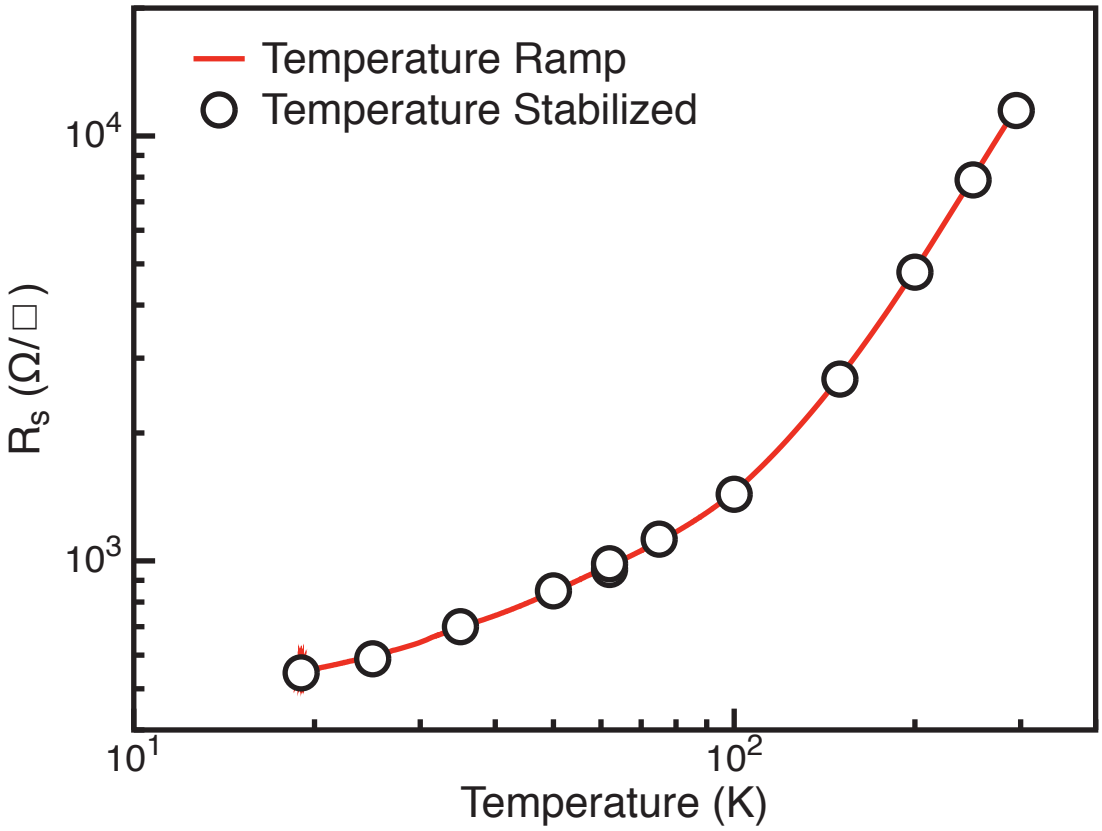

Figure A.3: Temperature dependence of R_s of a 10 unit cell $LaAlO_3/SrTiO_3$ sample.

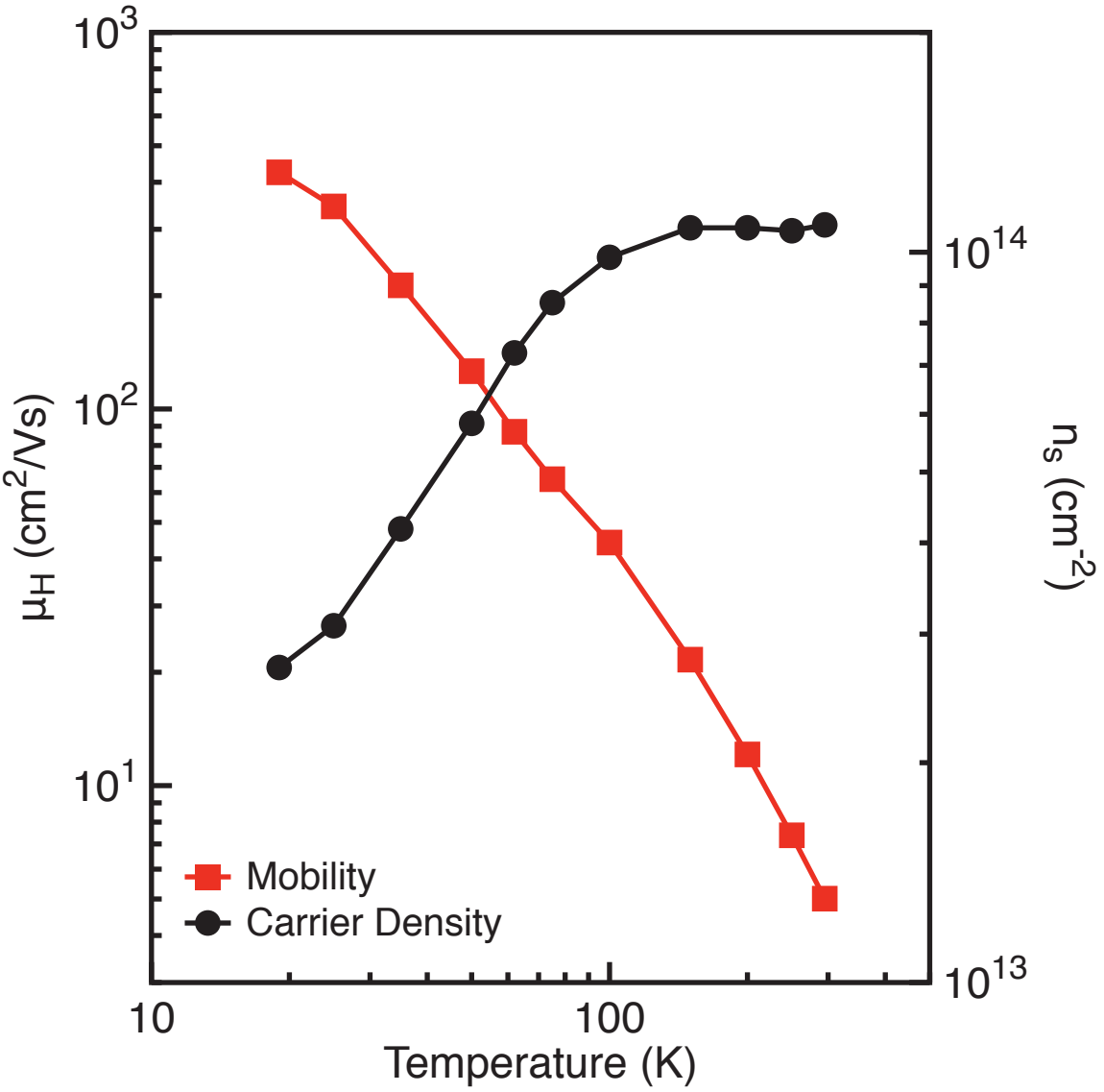

Figure A.4: Temperature dependence of n_s and μ_H of a 10 unit cell $LaAlO_3/SrTiO_3$ sample.

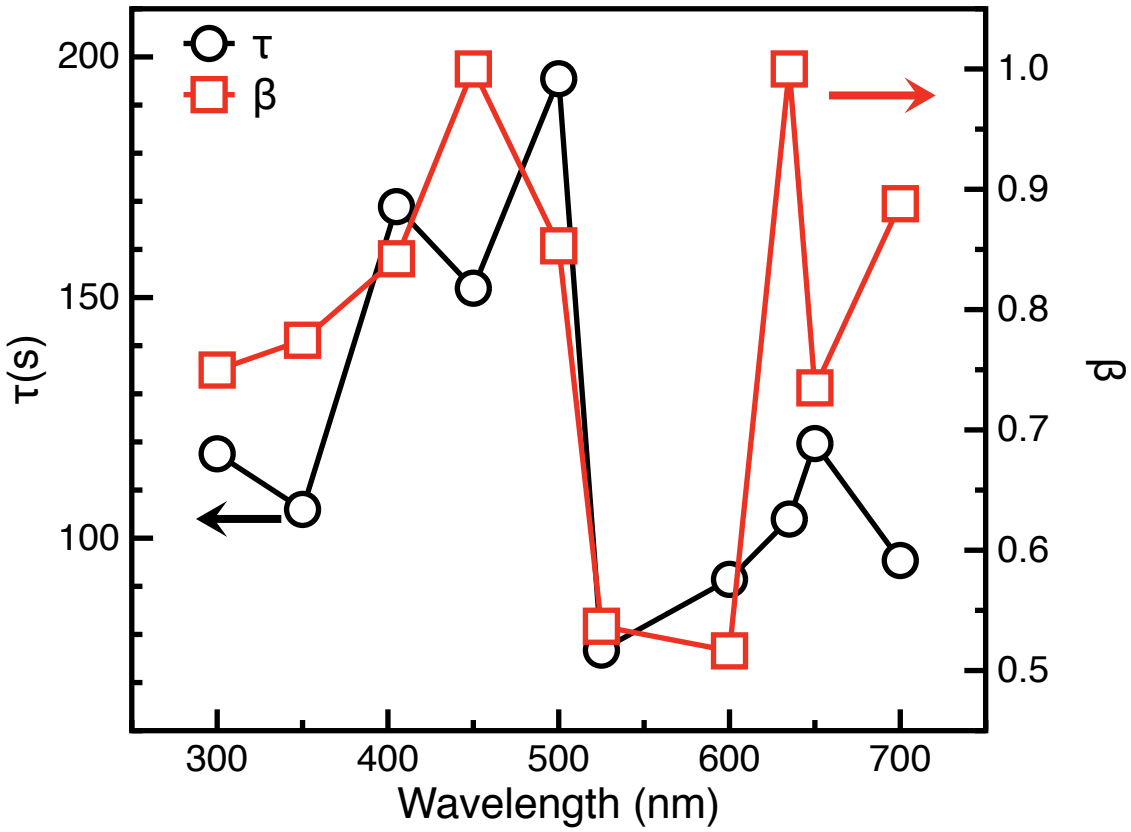

Figure A.5: Fitting parameters to stretched exponentials of the photoexposure in $LaAlO_3/SrTiO_3$.

A.2 Wavelength Response

We determiined the wavelength dependent response at room temperature by shining light from a JY HT20 Monochrometer with a 50 W Xe-Hg arc lamp source with quartz collimating optics and an incident intensity of 1–3 $\mu W/cm^2$. We monitored the resistance in a single van der Pauw configuration in real time. Light of different wavelengths was shone for 2.5 min and the sample was allowed to relax for another 2.5 min (see Fig. A.6). We fitted stretched exponentials as in Equation A.1 for the recovery periods, the time constants and exponentials obtained as a function of wavelength are shown in

Fig. A.5. From Fig. A.6 we can see a weak response in the λ =500–600 nm range, which yielded poor fits and fitting parameters. In the rest of the wavelength range, response times and exponentials are similar to reported in previos $LaAlO_3/SrTiO_3$ photoresistance experiments [109]. We select two wavelengths, 405 nm and 635 nm, that show good response in the spectrometry experiment and are both of less energy than the $SrTiO_3$ band gap to prevent direct promotion of carriers across the gap.

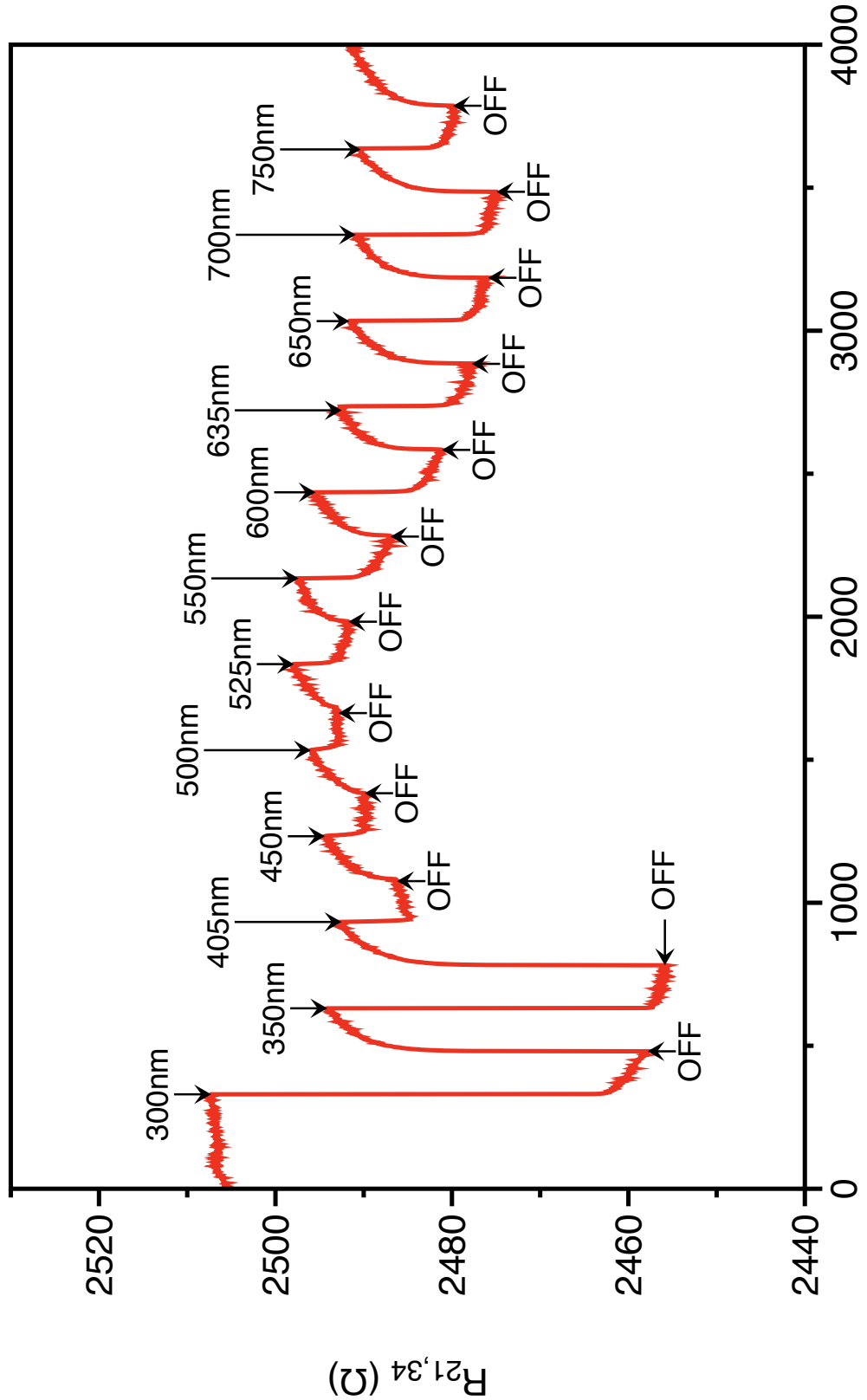

Figure A.6: Wavelength dependence of $R_{21,34}$ of $LaAlO_3/SrTiO_3$.

A.3 Mobility Enhancement from Sub-gap Photoexcitation

For temperature dependent transport with incident light we used a Cryo Industries He-flow cryostat mounted on an electromagnet with adjustable pole spacing, reaching a maximum of $\mu_0 H = 0.6$ T at the pole spacing required for this cryostat. The samples were irradiated with 405 nm and 635 nm wavelength light generated by two optical-fiber coupled laser diodes by Thorlabs (models LP405-SF10 and LPS-635-FC respectively) and collimated by a Thorlabs CFC-11X-A adjustable collimator with a focal length of 11.0 mm and anti-reflective coating for 350–700 nm light. The beam was wide enough to illuminate a majority of the sample surface (5×5 mm). The light was shone from the outside through the cryostat optical access. We tuned the excitation current to obtain an incident intensity of 2 mW/cm^2 for both laser diodes, compensating for attenuation due to the window of the cryostat.

A summary of the transport properties with light irradiation at room temperature is shown in Table A.1. The photoresistance only decreased with illumination from 405 nm light as seen Fig. A.7. The effect was associated with a +3.4% increased in carrier density and a -1% decreased in Hall mobility, which can be caused by promotion of carriers to trapped states that are then accessible to the conduction band by thermal activation. We could not obtain a reproducible effect when illuminating the sample with 635 nm, likely due to the weakness of the effect.

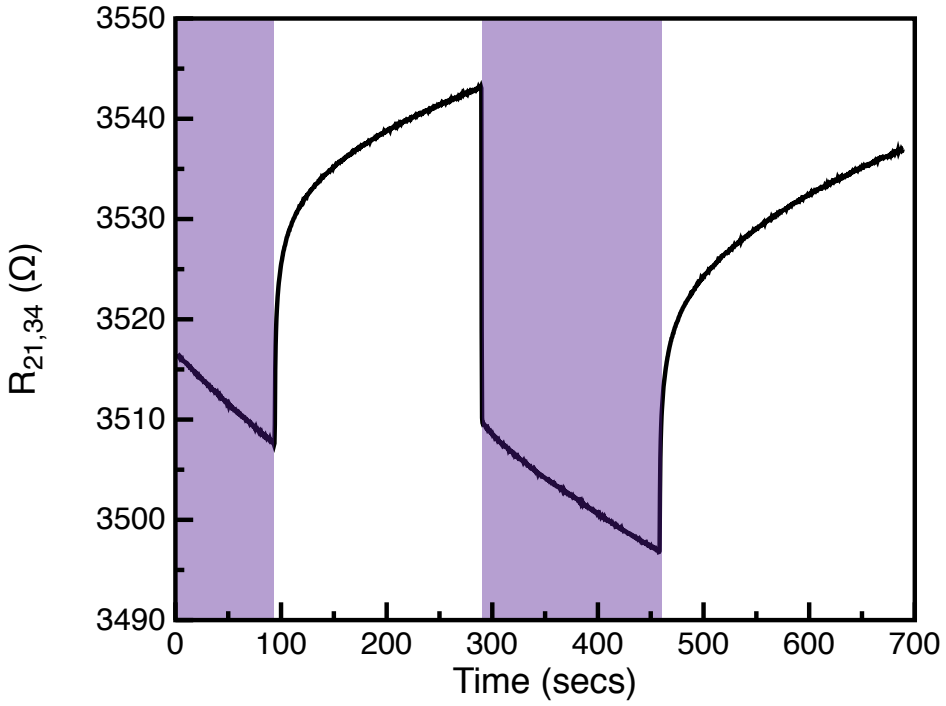

Figure A.7: Time dependent response of resistance to 405 nm light at $T = 295$ K. The shaded area indicates when sample was exposed to laser light.

Table A.1: Photo-sensitivity of Transport Properties at $T = 295$ K

Light	R_s (kΩ/□)	ΔR_s (%)	n_s (10^{13} cm^2)	Δn_s (%)	μ_H (cm^2/Vs)	$\Delta\mu_H$ (%)
none	12.00	-	10.97	-	4.74	-
635 nm	12.07	+0.6	10.97	0	4.71	+1
405 nm	11.75	−2.1	11.34	+3.4	4.69	−1

We attempted the same set of measurements at liquid He temperature (4.2 K), however, the thermal coupling between the sample and cold finger prevented the sample from reaching $T = 4.2$ K, as observed from the sample's sheet resistance. The sample, an $LaAlO_3$ film on an insulating $SrTiO_3$ substrate is mounted on a ceramic chip carrier that in turn is connected on an extended stage of the cold finger (see Fig. A.8). The cold finger was further thermally coupled by a thick Cu braid to the metallic back plate of the chip carrier, which is in direct contact with the back of the sample. Despite these efforts, a reliable coupling was not achieved, and the lowest temperature reached in the sample was 30 K, as determined by the R_s versus T curve in Fig A.3.

At $T = 30$ K the samples showed a significant decrease in resistance with light of both wavelengths. Figures A.9 and A.10 show the real-time resistance switching with applied light. The shaded area shows the time when light was being shone on the samples and the fitted parameters to stretched exponentials are shown in Table A.3. The characteristic times (τ) are in agreement with the one measured at room temperature but the exponent (β) at $T = 30$ K is lower than any seen at room temperature. The changes in resistance were of -4.6% and -8.1% for 635 nm and 405 nm light respectively. A summary of the transport properties is shown in Table A.10. The direct measurement of Hall coefficients, long after exposure, was the same for the dark, 635 nm and 405 nm light. An example of Hall voltages measured as a function of magnetic fields is shown in Fig. A.11, where the signals have been intentionally offset. This suggests the decrease in resistance observed is associated with a direct improvement of mobility of $+5.41\%$ and $+8.85\%$ for the 635 nm and 405 nm light, respectively.

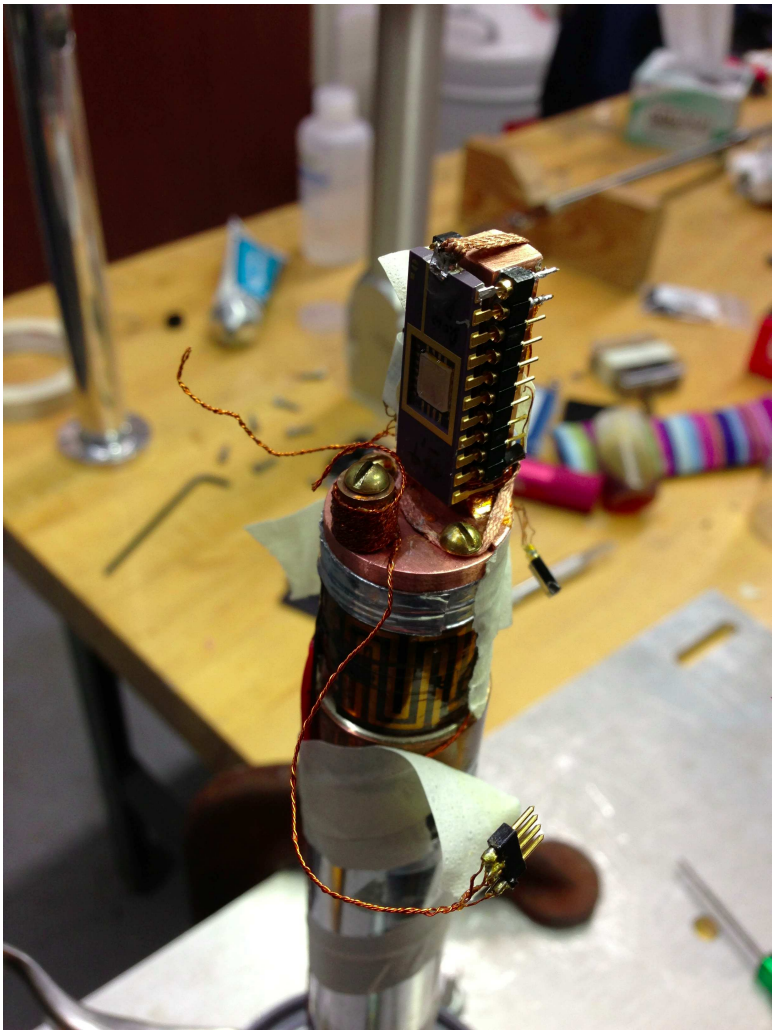

Figure A.8: Extended stage of the cold finger in the Cryo Industries He Flow crysotat, shown with a mounted chip carrier and sample.

Table A.2: Photo-sensitivity of Transport Properties at $T = 30$ K

Light	R_s ($\Omega/\square$)	ΔR_s (%)	n_s (10^{13} cm^2)	Δn_s (%)	μ_H (cm^2/Vs)	$\Delta\mu_H$ (%)
none	573	-	3.10	-	351	-
635 nm	547	-4.6	3.08	-0.6	370	$+5.41$
405 nm	526	-8.1	3.10	0	383	$+8.85$

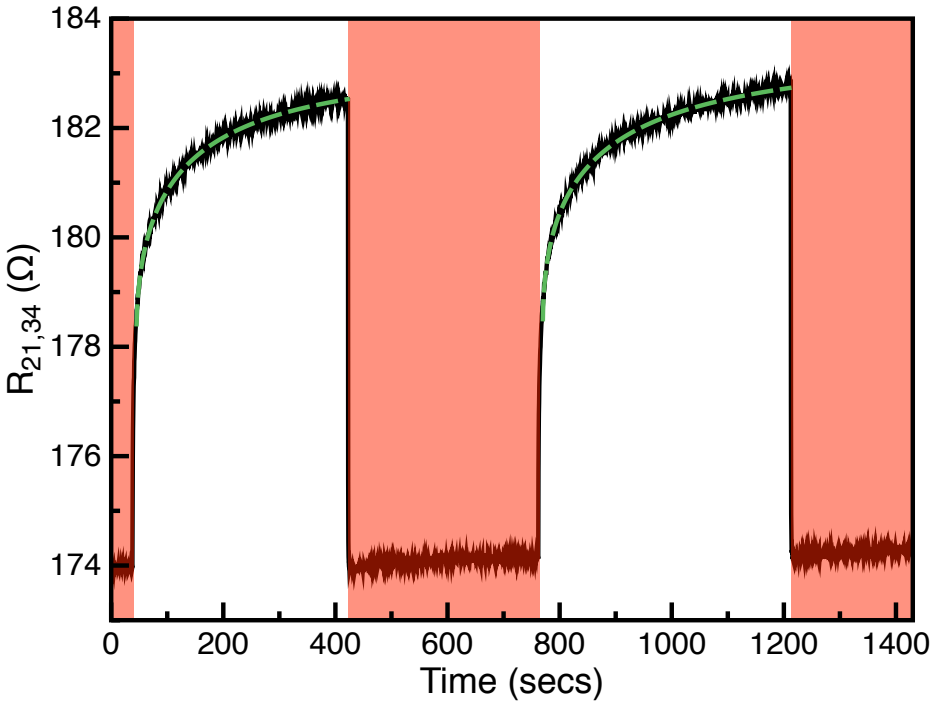

Figure A.9: Time dependent response of resistance to 635 nm light at $T = 30$ K. The shaded area indicates when sample was exposed to laser light. The green dashed lines indicate the fits to stretched exponentials.

Table A.3: Fitting parameters of a stretched exponential response for 405 nm and 635 nm light on $LaAlO_3/SrTiO_3$ at $T = 30$ K

Light	τ (s)	β
405 nm	133.5	0.458
6355 nm	102.4	0.506

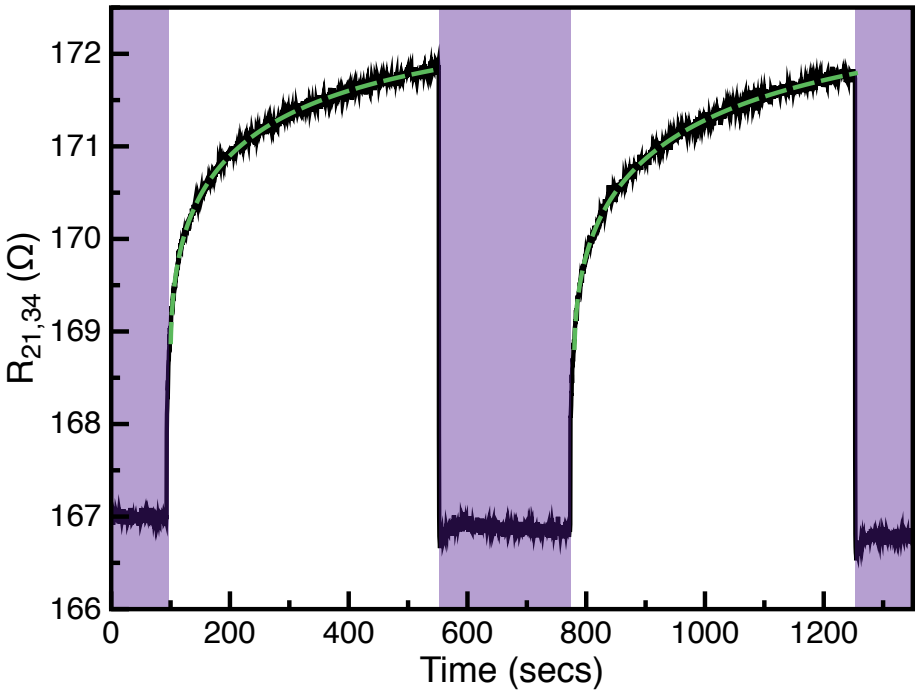

Figure A.10: Time dependent response of resistance to 405 nm light at $T = 30$ K. The shaded area indicates when sample was exposed to laser light. The green dashed lines indicate the fits to stretched exponentials.

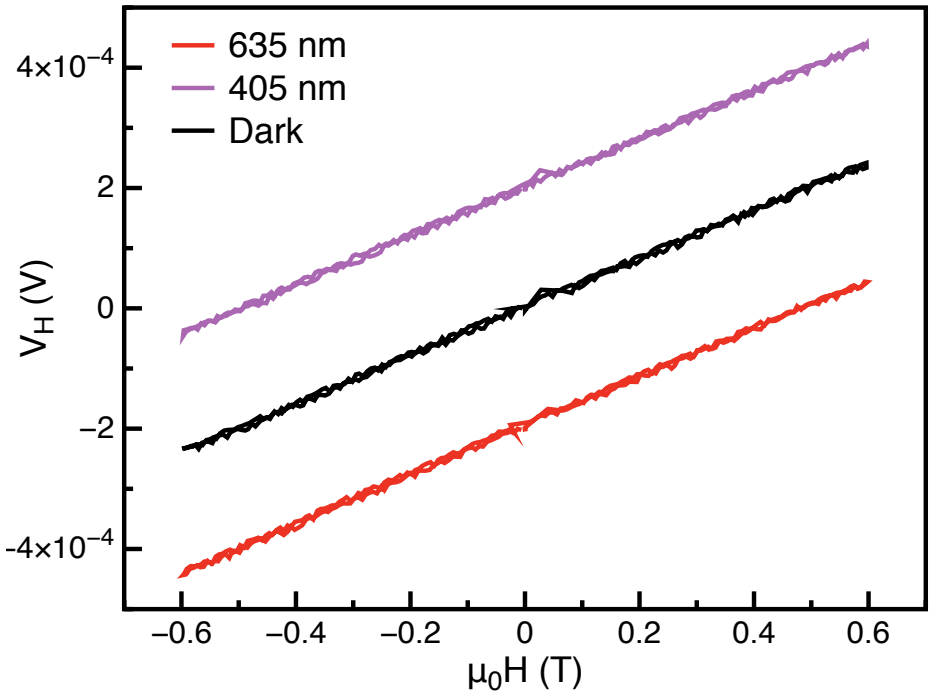

Figure A.11: Hall voltage signals as a function of applied magnetic field for $LaAlO_3/SrTiO_3$ under 635 nm and 405 nm irradiation and in a dark environment. The signals have been artificially offset.

A.4 Future Work

This preliminary result of mobility enhancement was not been previously reported for $LaAlO_3/SrTiO_3$ heterostructures, where most of the studies on the photo sensitivity of this interface found the promotion of carriers. This is in agreement with the commonly used light sources in the UV range, which have photon energies higher than the $SrTiO_3$ band gap. In order to rule out the possibility of two types of carriers, measurements at high magnetic fields need to be performed under illumination. A non-linearity of the transverse resistance with magentic field is typically indicative of multi-band transport at play, as it was found in Ref. [111]. Furthermore, the mobility enhancement effect manifests more strongly at $T = 30$ K than at room temperature; however, the Hall mobility has not saturated yet at this temperature. Mangetotransport characterization at $T = 4.2$ K will determine if the sample has a high-mobility two-dimensional electron gas ($\sim 10^4$ cm^2/Vs) and if the mobility enhancement still occurs after saturation due to phonon freeze out. Intensity or photon number dependent studies could further elucidate the absorption mechanism at play.

Bibliography

[1] Nat. Mat. **11**, 91 (2012).

[2] H. Y. Hwang, Y. Iwasa, M. Kawasaki, B. Keimer, N. Nagaosa, and Y. Tokura, Nature Materials **11**, 103 (2012).

[3] A. Ohtomo and H. Hwang, Nature **427**, 423 (2004).

[4] G. D. Mahan, *Condensed Matter in a Nutshell* (Princeton University Press, 2011) pp. 89–91.

[5] K. A. Müller and H. Burkard, Phys. Rev. B (1979).

[6] N. A. Pertsev, A. K. Tagantsev, and N. Setter, Phys. Rev. B **61**, R825 (2000).

[7] Y. S. Kim, D. J. Kim, T. H. Kim, T. W. Noh, J. S. Choi, B. H. Park, and J. G. Yoon, Appl. Phys. Lett. **91**, 042908 (2007).

[8] R. Wördenweber, E. Hollmann, R. Kutzner, and J. Schubert, J. Appl. Phys. **102**, 044119 (2007).

[9] H. W. Jang, A. Kumar, S. Denev, M. D. Biegalski, P. Maksymovych, C. W. Bark, C. T. Nelson, C. M. Folkman, S. H. Baek, N. Balke, C. M. Brooks, D. A. Tenne, D. G. Schlom, L. Q. Chen, X. Q. Pan, S. V. Kalinin, V. Gopalan, and C. B. Eom, Phys. Rev. Lett. **104**, 197601 (2010).

[10] H. Wu, R. Zhang, and Y. Zhan, Phys. Lett. A (2010).

[11] M. Egilmez, G. W. Leung, A. Hakimi, and M. G. Blamire, J. Appl. Phys. **108**, 123912 (2010).

[12] N. Nakagawa, H. Y. Hwang, and D. A. Muller, Nat. Mat. **5**, 204 (2006).

[13] S. Thiel, G. G. Hammerl, A. Schmehl, C. W. Schneider, and J. Mannhart, Science **313**, 1942 (2006).

[14] M. Huijben, G. Rijnders, D. H. A. Blank, S. Bals, S. van Aert, J. Verbeeck, G. van Tendeloo, A. Brinkman, and H. Hilgenkamp, Nat. Mater. **5**, 556 (2006).

[15] H. Frederikse, W. Thurber, and W. Hosler, Phys. Rev. **134**, A442 (1964).

[16] J. Schooley, W. Hosler, and M. Cohen, Phys. Rev. Lett. **12**, 474 (1964).

[17] O. Tufte and P. Chapman, Phys. Rev. **155**, 796 (1967).

[18] C. S. Koonce and M. L. Cohen, Phys. Rev. **163**, 380 (1967).

[19] C. Lee, J. Destry, and J. Brebner, Phys. Rev. B **11**, 2299 (1975).

[20] W. Gong, H. Yun, Y. Ning, J. Greedan, W. Datars, and V. Stager, J. Solid State Chem. **90**, 320 (1991).

[21] Y. Aiura, Y. Nishihara, Y. Haruyama, T. Komeda, S. Kodaira, Y. Sakisaka, T. Maruyama, and H. Kato, Physica B **194-196**, 1215 (1994).

[22] N. Shanthi and D. D. Sarma, Phys. Rev. B **57**, 2153 (1998).

[23] H. Frederikse and W. Hosler, Phys. Rev. **161**, 822 (1967).

[24] A. Kalabukhov, R. Gunnarsson, J. Börjesson, E. Olsson, T. Claeson, and D. Winkler, Phys. Rev. B **75**, 121404(R) (2007).

[25] W. Siemons, G. Koster, H. Yamamoto, W. A. Harrison, G. Lucovsky, T. H. Geballe, D. H. A. Blank, and M. R. Beasley, Phys. Rev. Lett. **98**, 196802 (2007).

[26] G. Herranz, M. Basletić, M. Bibes, C. Carrétéro, E. Tafra, E. Jacquet, K. Bouzehouane, C. Deranlot, A. Hamzić, J.-M. Broto, A. Barthélémy, and A. Fert, Phys. Rev. Lett. **98**, 216803 (2007).

[27] C. W. Schneider, M. Esposito, I. Marozau, K. Conder, M. Doebeli, Y. Hu, M. Mallepell, A. Wokaun, and T. Lippert, Appl. Phys. Lett. **97**, 192107 (2010).

[28] A. Brinkman, M. Huijben, M. van Zalk, J. Huijben, U. Zeitler, J. C. Maan, W. G. van der Wiel, G. Rijnders, D. H. A. Blank, and H. Hilgenkamp, Nat. Mater. **6**, 493 (2007).

[29] T. Hernandez, C. W. Bark, D. A. Felker, C. B. Eom, and M. S. Rzchowski, Phys. Rev. B **85**, 161407(R) (2012).

[30] H. Chen, A. M. Kolpak, and S. Ismail-Beigi, Adv. Mat. **22**, 2881 (2010).

[31] G. Herranz, O. Copie, A. Gentils, E. Tafra, M. Basletic, F. Fortuna, K. Bouzehouane, S. Fusil, E. Jacquet, C. Carretero, M. Bibes, A. Hamzic, and A. Barthelemy, J. Appl. Phys. **107**, 103704 (2010).

[32] J. H. Ngai, Y. Segal, F. J. Walker, and C. H. Ahn, Phys. Rev. B **83**, 045304 (2011).

[33] A. F. Santander-Syro, O. Copie, T. Kondo, F. Fortuna, S. Pailhès, R. Weht, X. G. Qiu, F. Bertran, A. Nicolaou, A. Taleb-Ibrahimi, P. Le Fèvre, G. Herranz, M. Bibes, N. Reyren, Y. Apertet, P. Lecoeur, A. Barthelemy, and M. J. Rozenberg, Nature **469**, 189 (2011).

[34] R. Di Capua, M. Radovic, G. M. De Luca, I. Maggio-Aprile, F. Miletto Granozio,

N. C. Plumb, Z. Ristic, U. Scotti di Uccio, R. Vaglio, and M. Salluzzo, Phys. Rev. B **86**, 155425 (2012).

[35] A. Ohtomo and H. Y. Hwang, J. Appl. Phys. **102**, 083704 (2007).

[36] P. Willmott, S. Pauli, R. Herger, C. Schlepütz, D. Martoccia, B. Patterson, B. Delley, R. Clarke, D. Kumah, C. Cionca, and Y. Yacoby, Phys. Rev. Lett. **99** (2007).

[37] Y. Fujishima, Y. Tokura, T. Arima, and S. Uchida, Phys. Rev. B **46**, 11167 (1992).

[38] A. Fujimori, I. Hase, M. Nakamura, H. Namatame, Y. Fujishima, Y. Tokura, M. Abbate, F. de Groot, M. Czyzyk, J. Fuggle, O. Strebel, F. Lopez, M. Domke, and G. Kaindl, Phys. Rev. B **46**, 9841 (1992).

[39] M. Takizawa, H. Wadati, K. Tanaka, M. Hashimoto, T. Yoshida, A. Fujimori, A. Chikamatsu, H. Kumigashira, M. Oshima, K. Shibuya, T. Mihara, T. Ohnishi, M. Lippmaa, M. Kawasaki, H. Koinuma, S. Okamoto, and A. Millis, Phys. Rev. Lett. **97**, 057601 (2006).

[40] A. S. Kalabukhov, Y. A. Boikov, I. T. Serenkov, V. I. Sakharov, V. N. Popok, R. Gunnarsson, J. Borjesson, N. Ljustina, E. Olsson, D. Winkler, and T. Claeson, Phys. Rev. Lett. **103**, 146101 (2009).

[41] S. A. Chambers, M. H. Engelhard, V. Shutthanandan, Z. Zhu, T. C. Droubay, L. Qiao, P. V. Sushko, T. Feng, H. D. Lee, T. Gustafsson, E. Garfunkel, A. B. Shah, J. M. Zuo, and Q. M. Ramasse, Surf. Sci. Rep. **65**, 317 (2010).

[42] S. A. Chambers, Surf. Sci. **605**, 1133 (2011).

[43] M. Sing, G. Berner, K. Goß, A. Müller, A. Ruff, A. Wetscherek, S. Thiel,

J. Mannhart, S. A. Pauli, C. W. Schneider, P. R. Willmott, M. Gorgoi, F. Schäfers, and R. Claessen, Phys. Rev. Lett. **102**, 176805 (2009).

[44] A. Dubroka, M. Rössle, K. W. Kim, V. K. Malik, L. Schultz, S. Thiel, C. W. Schneider, J. Mannhart, G. Herranz, O. Copie, M. Bibes, A. Barthélémy, and C. Bernhard, Phys. Rev. Lett. **104**, 156807 (2010).

[45] A. Savoia, D. Paparo, P. Perna, Z. Ristic, M. Salluzzo, F. M. Granozio, U. S. di Uccio, C. Richter, S. Thiel, J. Mannhart, and L. Marrucci, Phys. Rev. B **80**, 075110 (2009).

[46] R. Pentcheva and W. Pickett, Physical Review B **74**, 035112 (2006).

[47] Z. S. Popović, S. Satpathy, and R. M. Martin, Phys. Rev. Lett. **101**, 256801 (2008).

[48] F. A. Cotton, *Chemical Applications of Group Theory* (John Wiley and Sons, Inc., 1990) pp. 282–286.

[49] A. R. West, *Basic Solid State Chemistry, Second Edition* (John Wiley and Sons, Ltd, 1999) pp. 100–102.

[50] M. Salluzzo, J. C. Cezar, N. B. Brookes, V. Bisogni, G. M. D. Luca, C. Richter, S. Thiel, J. Mannhart, M. Huijben, A. Brinkman, G. Rijnders, and G. Ghiringhelli, Phys. Rev. Lett. **102**, 166804 (2009).

[51] P. Delugas, A. Filippetti, V. Fiorentini, D. I. Bilc, D. Fontaine, and P. Ghosez, Phys. Rev. Lett. **106**, 166807 (2011).

[52] N. Reyren, S. Thiel, A. Caviglia, L. Kourkoutis, G. Hammerl, C. Richter,

C. Schneider, T. Kopp, A. Rüetschi, D. Jaccard, M. Gabay, D. Muller, J.-M. Triscone, and J. Mannhart, Science **317**, 1196 (2007).

[53] A. D. Caviglia, S. Gariglio, C. Cancellieri, B. Sacépé, A. Fête, N. Reyren, M. Gabay, A. F. Morpurgo, and J.-M. Triscone, Phys. Rev. Lett. **105**, 236802 (2010).

[54] A. D. Caviglia, S. Gariglio, N. Reyren, D. Jaccard, T. Schneider, M. Gabay, S. Thiel, G. Hammerl, J. Mannhart, and J.-M. Triscone, Nature **456**, 624 (2008).

[55] C. Bell, S. Harashima, Y. Kozuka, M. Kim, B. Kim, Y. Hikita, and H. Y. Hwang, Phys. Rev. Lett. **103**, 226802 (2009).

[56] A. D. Caviglia, M. Gabay, S. Gariglio, N. Reyren, C. Cancellieri, and J.-M. Triscone, Phys. Rev. Lett. **104**, 126803 (2010).

[57] M. Ben Shalom, M. Sachs, D. Rakhmilevitch, A. Palevski, and Y. Dagan, Phys. Rev. Lett. **104**, 126802 (2010).

[58] Y. C. Liao, T. Kopp, C. Richter, A. Rosch, and J. Mannhart, Phys. Rev. B **83**, 075402 (2011).

[59] C. W. Schneider, S. Thiel, G. Hammerl, C. Richter, and J. Mannhart, Appl. Phys. Lett. **89**, 122101 (2006).

[60] Y. Xie, Y. Hikita, C. Bell, and H. Y. Hwang, Nat. Comm. **2**, 494 (2011).

[61] D. Stornaiuolo, S. Gariglio, N. J. G. Couto, A. Fe te, A. D. Caviglia, G. Seyfarth, D. Jaccard, A. F. Morpurgo, and J.-M. Triscone, Appl. Phys. Lett. **101**, 222601 (2012).

[62] C. Cen, S. Thiel, G. Hammerl, C. W. Schneider, K. E. Andersen, C. S. Hellberg, J. Mannhart, and J. Levy, Nat. Mater. **7**, 298 (2008).

[63] J. W. Park, D. F. Bogorin, C. Cen, D. A. Felker, Y. Zhang, C. T. Nelson, C. W. Bark, C. M. Folkman, X. Q. Pan, M. S. Rzchowski, J. Levy, and C. B. Eom, Nat. Comm. **1**, 94 (2010).

[64] C. W. Bark, D. A. Felker, Y. Wang, Y. Zhang, H. W. Jang, C. M. Folkman, J. W. Park, S. H. Baek, H. Zhou, D. D. Fong, X. Q. Pan, E. Y. Tsymbal, M. S. Rzchowski, and C. B. Eom, P. Natl. Acad. Sci. USA. **108**, 4720 (2011).

[65] A. E. Lee, C. E. Platt, J. F. Burch, R. W. Simon, J. P. Goral, and M. M. Al-Jassim, Appl. Phys. Lett. **57**, 2019 (1990).

[66] I. M. Dildar, D. Boltje, M. Hesselberth, Q. Xu, H. Zandbergen, S. Harkema, and J. Aarts, e-J. Surf. Sci. Nanotech. **10**, 619 (2012).

[67] J. P. Podkaminer, T. Hernandez, M. Huang, S. Ryu, C. W. Bark, S. H. Baek, J. C. Frederick, T. H. Kim, K. H. Cho, J. Levy, M. S. Rzchowski, and C. B. Eom, Appl. Phys. Lett. **103**, 071604 (2013).

[68] P. Brinks, W. Siemons, J. E. Kleibeuker, G. Koster, G. Rijnders, and M. Huijben, Appl. Phys. Lett. **98**, 242904 (2011).

[69] S. Thiel, C. W. Schneider, L. L. Fitting Kourkoutis, D. A. Muller, N. Reyren, A. D. Caviglia, S. Gariglio, J.-M. Triscone, and J. Mannhart, Phys. Rev. Lett. **102**, 046809 (2009).

[70] F. J. Wong, R. V. Chopdekar, and Y. Suzuki, Phys. Rev. B **82**, 165413 (2010).

[71] B. Jalan, S. J. Allen, G. E. Beltz, P. Moetakef, and S. Stemmer, Appl. Phys. Lett. **98**, 132102 (2011).

[72] F. He, B. O. Wells, and S. M. Shapiro, Phys. Rev. Lett. **94**, 176101 (2005).

[73] M. Lundstrom, *Fundamentals of Carrier Transport* (Cambridge University Press, 2000).

[74] B. I. Shklovskii and A. L. Efros, *Electronic Properties of Doped Semiconductors* (Springer-Verlag, Berlin, 1984) pp. 202–210.

[75] W. Jones and N. H. March, *Theoretical Solid State Physics Volume 2: Non-equilibrium and Disorder* (Dover Publications, 1985) p. 727.

[76] Measured on 7 uc of LAO grown on TiO_2 terminated (001) STO substrate by PLD, with $\mu_H = 5.6$ cm^2/V s and $n_s = 8.7 \times 10^{13}$ cm^{-2} at room temperature, and $\mu_H = 3700$ cm^2/V s and $n_s = 1.8 \times 10^{13}$ cm^{-2} at 3 K.

[77] S. Seri, E. Shimshoni, S. Paetel, J. Mannhart, and L. Klein, IEEE. T. Magn. **46**, 1630 (2010).

[78] U. Sivan, O. Entin-Wohlman, and Y. Imry, Phys. Rev. Lett. **60**, 1566 (1988).

[79] S. Maekawa and H. Fukuyama, J. Phys. Soc. Jpn. **50**, 2516 (1981).

[80] J. H. Ngai, Y. Segal, D. Su, Y. Zhu, F. J. Walker, S. Ismail-Beigi, K. L. Hur, and C. H. Ahn, Phys. Rev. B **81**, 241307(R) (2010).

[81] D. Bishop, R. C. Dynes, and D. C. Tsui, Phys. Rev. B , 126803 (1982).

[82] B. C. Chakoumakos, D. G. Schlom, M. Urbanik, and J. Luine, J. Appl. Phys. **83**, 1979 (1998).

[83] J. Mannhart and D. Schlom, Science **327**, 1607 (2010).

[84] C. Cen, S. Thiel, J. Mannhart, and J. Levy, Science **323**, 1026 (2009).

[85] N. Reyren, S. Thiel, A. Caviglia, L. Kourkoutis, G. Hammerl, C. Richter, C. Schneider, T. Kopp, A. Rüetschi, D. Jaccard, M. Gabay, D. Muller, J.-M. Triscone, and J. Mannhart, Science **317**, 1196 (2007).

[86] M. Huijben, A. Brinkman, G. Koster, G. Rijnders, H. Hilgenkamp, and D. H. A. Blank, Adv. Mater. **21**, 1665 (2009).

[87] H. Jeffrey Gardner, A. Kumar, L. Yu, P. Xiong, M. P. Warusawithana, L. Wang, O. Vafek, and D. G. Schlom, Nat. Phys. **7**, 895 (2011).

[88] M. P. Warusawithana, C. Richter, J. A. Mundy, P. Roy, J. Ludwig, S. Paetel, T. Heeg, A. A. Pawlicki, L. F. Kourkoutis, M. Zheng, M. Lee, B. Mulcahy, W. Zander, Y. Zhu, J. Schubert, J. N. Eckstein, D. A. Muller, C. S. Hellberg, J. Mannhart, and D. G. Schlom, "LaAlO3 stoichiometry found key to electron liquid formation at LaAlO3/SrTiO3 interfaces," (2013), arXiv:1303.5352 [cond-mat.mtrl-sci] .

[89] C. B. Eom, J. Z. Sun, K. Yamamoto, A. F. Marshall, K. E. Luther, T. H. Geballe, and S. S. Laderman, Appl. Phys. Lett. **55**, 595 (1989).

[90] C. B. Eom, A. F. Marshall, S. S. Laderman, R. D. Jacowitz, and T. H. Geballe, Science **249**, 1549 (1990).

[91] E. Sader, H. Schmidt, K. Hradil, and W. Wersing, Supercond. Sci. Tech. **4**, 371 (1999).

[92] K. Yamamoto, B. M. Lairson, C. B. Eom, R. H. Hammond, J. C. Bravman, and T. H. Geballe, Appl. Phys. Lett. **57**, 1936 (1990).

[93] M. Kawasaki, K. Takahashi, T. Maeda, R. Tsuchiya, M. Shinohara, O. Ishiyama, T. Yonezawa, M. Yoshimoto, and H. Koinuma, Science **266**, 1540 (1994).

[94] R. Moos, W. Menesklou, and K. H. Härdtl, Appl. Physi. A-Mater. **61**, 389 (1995).

[95] G. J. H. M. Rijnders, G. Koster, D. H. A. Blank, and H. Rogalla, Appl. Phys. Lett. **70**, 1888 (1997).

[96] M. Björck and G. Andersson, J. Appl. Crystallogr. **40**, 1174 (2007).

[97] J. Chakhalian, A. J. Millis, and J. Rondinelli, Nat. Mat. **11**, 92 (2012).

[98] K.-Y. Yang, W. Zhu, D. Xiao, S. Okamoto, Z. Wang, and Y. Ran, Phys. Rev. B **84**, 201104 (2011).

[99] D. Xiao, W. Zhu, Y. Ran, N. Nagaosa, and S. Okamoto, Nat. Comm. **2**, 596 (2011).

[100] A. Rüegg and G. Fiete, Phys. Rev. B **84**, 201103 (2011).

[101] G. Herranz, F. Sánchez, N. Dix, M. Scigaj, and J. Fontcuberta, Sci. Rep. **2** (2012).

[102] A. Biswas, P. B. Rossen, C.-H. Yang, W. Siemons, M.-H. Jung, I. K. Yang, R. Ramesh, and Y. H. Jeong, Appl. Phys. Lett. **98**, 051904 (2011).

[103] G. Kresse and F. J, Phys. Rev. B **54**, 11169 (1996).

[104] R. Yamamoto, C. Bell, Y. Hikita, H. Y. Hwang, H. Nakamura, T. Kimura, and Y. Wakabayashi, Phys. Rev. Lett. **107**, 036104 (2011).

[105] S. A. Pauli, S. J. Leake, B. Delley, M. Björck, C. W. Schneider, C. M. Schlepütz, D. Martoccia, S. Paetel, J. Mannhart, and P. R. Willmott, Phys. Rev. Lett. **106**, 036101 (2011).

[106] C. Cancellieri, D. Fontaine, S. Gariglio, N. Reyren, A. D. Caviglia, A. Fête, S. J. Leake, S. A. Pauli, P. R. Willmott, M. Stengel, P. Ghosez, and J.-M. Triscone, Phys. Rev. Lett. **107** (2011).

[107] P. Irvin, Y. Ma, D. F. Bogorin, C. Cen, C. W. Bark, C. M. Folkman, C.-B. Eom, and J. Levy, Nat. Photonics **4**, 849 (2010).

[108] Z. Ristic, R. Di Capua, F. Chiarella, G. De Luca, I. Maggio-Aprile, M. Radovic, and M. Salluzzo, Phys. Rev. B **86**, 045127 (2012).

[109] A. Rastogi and R. C. Budhani, Opt. Lett. **37**, 317 (2012).

[110] A. Tebano, E. Fabbri, D. Pergolesi, G. Balestrino, and E. Traversa, ACS Nano. **6**, 1278 (2012).

[111] V. K. Guduru, A. Granados del Aguila, S. Wenderich, M. K. Kruize, A. McCollam, P. C. M. Christianen, U. Zeitler, A. Brinkman, G. Rijnders, H. Hilgenkamp, and J. C. Maan, Appl. Phys. Lett. **102**, 051604 (2013).

[112] D. Kan, T. Terashima, R. Kanda, A. Masuno, K. Tanaka, S. Chu, H. Kan, A. Ishizumi, Y. Kanemitsu, Y. Shimakawa, and M. Takano, Nat. Mat. **4**, 816 (2005).